# Development of Advanced Curling Probe for Reactive Plasma Measurement

Doctor of Philosophy (Ph.D.) Dissertation

（博士論文）

**March, 2016**

Anil Pandey

Department of Electrical and Electronic Engineering,
Graduate School of Engineering,
Chubu University, Japan

# Table of contents

# Chapter 1

# Introduction

## 1.1 General introduction

Matter exists in four states, i.e, solid, liquid, gas and plasma. Plasma, also called as the fourth state of matter comprises of more than 99% of matter in the universe. Matter can be changed from one state to another by the application of heat energy, e.g., from solid to liquid and liquid to gas. A gas which is subjected to very high temperature can be converted into a plasma. Actually, a plasma is an ionized gas which is electrically neutral. In other words, a plasma has almost equal number of negative and positively charged particles. If $n_e$, $n_i$ and $n_n$ are the respective densities of electrons, ions and neutral species in plasma, then,

$$n_e \approx n_i \quad . \tag{1.1}$$

This nature of plasma gives a unique characteristic to plasma, viz, quasi-neutrality.

Plasmas occur in nature in the form of lightening, aurora, flames etc. Since, naturally occurring plasma cannot be controlled and used specifically for human needs, different methods are employed to produce laboratory/industrial plasma. Plasmas produced in industries are used to manufacture microelectronics that we use in our computer, tablets and smartphones, to produce different types of lighting devices like fluorescent lamps, neon lamps. Arc discharge plasma is used in industries to cut, melt and weld metals. Apart from these, plasmas are also used in space propulsion of rockets and there is a continuing research on nuclear fusion using plasmas to produce clean energy. For the production and tailoring of plasma to suit specific needs, a basic understanding of certain fundamental terms related to plasma is essential.

## 1.2 Plasma fundamentals

### 1.2.1 Degree of ionization

The amount of ionization in a gas in thermal equilibrium is predicted by Saha's equation

$$\frac{n_i}{n_n} = 2.045 \times 10^{21} \times T^{\frac{3}{2}} \times \frac{1}{n_i} \times \exp\left(-\frac{U}{kT}\right) . \qquad (1.2)$$

Where $n_i, n_n$ are the ion and neutral particle densities in $cm^{-3}$, $T$ is the electron temperature in Kelvin, $U$ is the ionization energy of the gas atom and $k$ is the Boltzmann constant.

The *degree of ionization* can be expressed as a ratio of ionized particles to the total number of charged and neutral particles in plasma. It can be expressed as

$$\alpha = \frac{n_i}{n_i + n_n} . \qquad (1.3)$$

Based upon the degree of ionization, plasma can be classified into three categories. When the degree of ionization $\alpha = 1$, the plasma is said to be ***fully ionized plasma***. Such plasma is observed in coronal discharge and during fusion process. Plasmas with degree of ionization greater than 1% are called ***strongly ionized plasmas***. Most of the plasma processing is carried out by a third category of plasma, where degree of ionization is less than 0.1%. Such plasmas are called ***weakly ionized plasma***. This thesis is concerned with weakly ionized plasmas.

### 1.2.2 Quasi-neutrality and Debye length

Quasi-neutrality of plasma arises due to the equivalent number of ions and electrons in it. However, this property can break down over a certain distance, which is called Debye length.

Let us consider a single charge q in free space. By Coulomb's law the potential $\varphi$ due to the charge over a distance $r$ is given by

$$\varphi = \frac{q}{4\pi\varepsilon_o r} . \qquad (1.4)$$

In a plasma, a charged particle attracts other oppositely charged particles around it to shield the electric field. Therefore, compared to a single charge in free space, the potential due to a charge in plasma will decrease sharply. The potential of the charge $q$ at a distance of $r$ in a plasma is given by the equation

$$\varphi = \frac{q}{4\pi\varepsilon_o r}\exp\left(-\frac{r}{\lambda_D}\right). \qquad (1.5)$$

where $\lambda_D = \sqrt{\frac{\varepsilon_o kT_e}{e^2 n_e}}$ is the Debye length, $e$ is the charge of electron, $n_e$ is the electron density, $k$ is the Boltzmann constant, and $T_e$ is the electron temperature.

It can be inferred from the above equation that, inside the Debye length($r < \lambda_D$), the potential of charge $q$ follows Coulomb`s law, however, outside the Debye length, there is an exponential decrease of potential.

### 1.2.3 Plasma frequency

A plasma consists of very light electrons and massive ions. If we displace the electrons from their mean position, an electric field is set up, which tends to bring the electrons back to their normal position. Considering a collision less environment the electrons move back and overshoot their initial position, causing an oscillation in a characteristic frequency. This frequency is called ***plasma frequency*** $\omega_p$ given as

$$\omega_p = \sqrt{\frac{ne^2}{\varepsilon_o m_e}}. \qquad (1.6)$$

where $n$ is the electron density, $e$ is the charge of electron, $\varepsilon_0$is the permittivity of free space

and $m_e$ is the mass of electron

In SI units, this equation can be written as

$$f_p = \frac{\omega_p}{2\pi} = 8.98\times10^3\sqrt{n_e\left[cm^{-3}\right]}\ \text{[Hz]}. \qquad (1.7)$$

## 1.3 Plasma diagnostics and monitoring tools

The semi-conductor industry utilizes low temperature plasmas. To control the process it is necessary to have knowledge of plasma parameters like electron temperature, electron density, plasma potential etc. Different types of plasma monitoring tools are available that enable measurement of such parameters. Out of the several techniques, probe techniques enable local and spatial measurement of plasma parameters. Some of the probe techniques are discussed below.

### 1.3.1 Langmuir probe

Langmuir probe[1)] was originally developed by Langmuir and Mott-Smith and to this day remains one of the most-widely used plasma diagnostic tool. Langmuir probe technique involves the injection of a thin metallic electrode (preferably tungsten) in a plasma and measuring the current on application of potential in it. A typical probe current-voltage (I-V) curve obtained by using Langmuir probe is as shown in Fig. 1.1. Plasma potential, electron temperature, density and electron energy distribution function (EEDF) can all be calculated through probe I-V characteristics.

Langmuir probe is easy to construct and operate but it is very difficult to interpret the I-V characteristics[2-5)] of the probe. Also, inserting a bare metal in plasma causes metal impurity

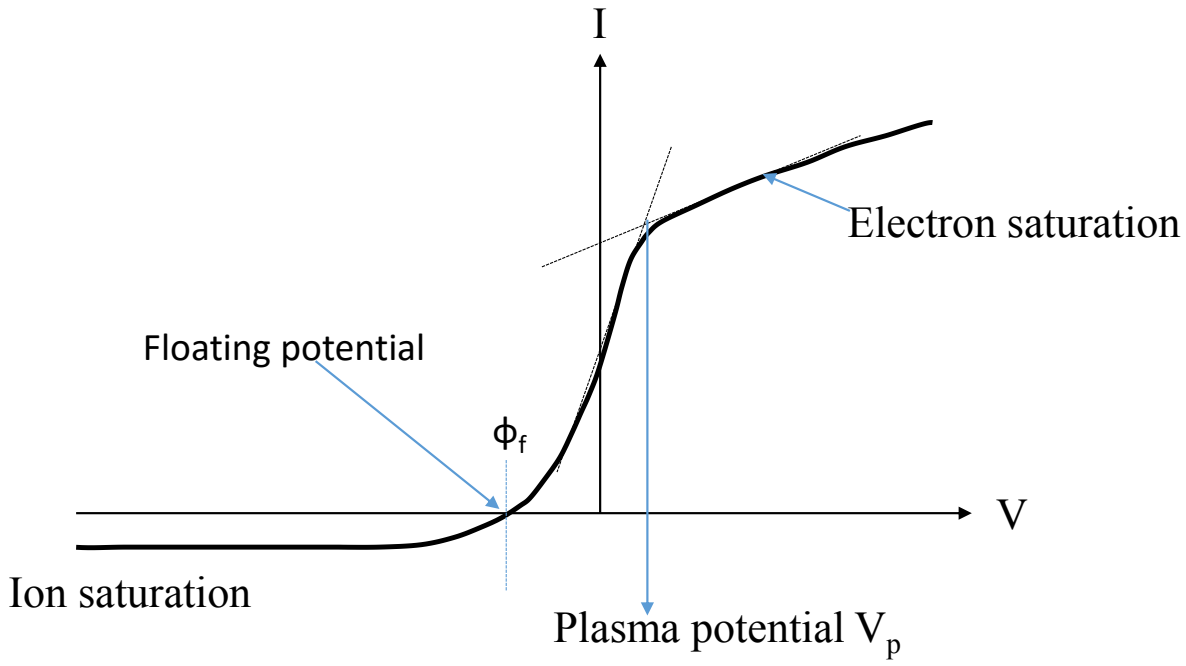


Fig. 1.1 Typical current-voltage characteristics of Langmuir probe.

contamination. A complicated circuitry is needed when probe needs to be used in Radio-Frequency (RF) plasmas to avoid RF-pickup. The most serious problem with Langmuir probe arises when the probe is used in reactive plasmas. For example, the fluorocarbon plasma used in silicon dioxide etching covers the chamber wall and probe tip with insulating polymer layer which interrupts the flow of current through the metal tip making probe measurement impossible.

### 1.3.2 Plasma oscillation probe

A plasma oscillation probe (POP)[6] has a hot filament, which injects a beam of electrons into plasma that excites the plasma waves near plasma frequency $\omega_p$. The oscillations caused by electron beam is received by a detector and observed using a spectrum analyzer. If a resonance peak is detected, this peak will be close to $\omega_p$ and electron density *c*an be calculated by using the equation

$$n_e = \frac{\omega_{pe}^2 \varepsilon_0 m_e}{e^2}$$

$$= 1.24 \times 10^{-2} \left( \frac{\omega_{pe}}{2\pi} \right)^2 \quad [m^{-3}] \qquad (1.8)$$

Fig.1.2 (a), (b), and (c) show a typical oscillation probe and the signal obtained in the spectrum analyzer respectively.

Plasma oscillation probe utilizes hot-filament as a source of electron. The life-time such filament is very short. Also, it has a narrow operable pressure range and can cause metal impurity contamination to the plasma.

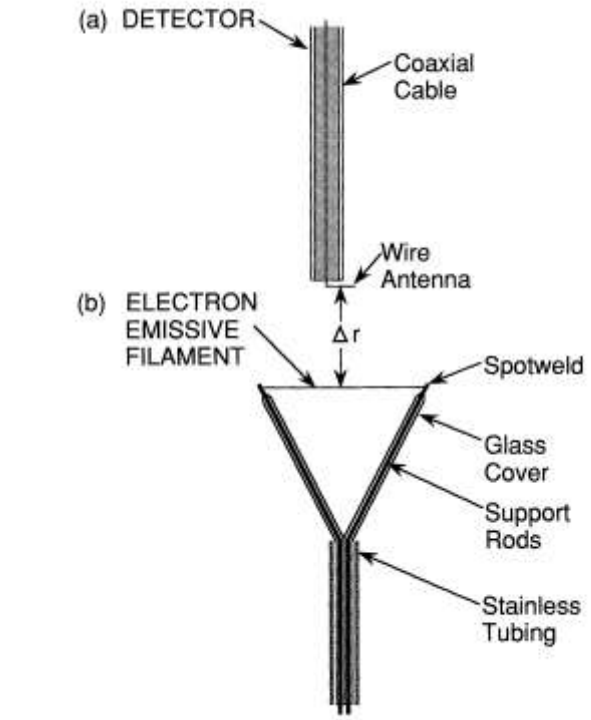


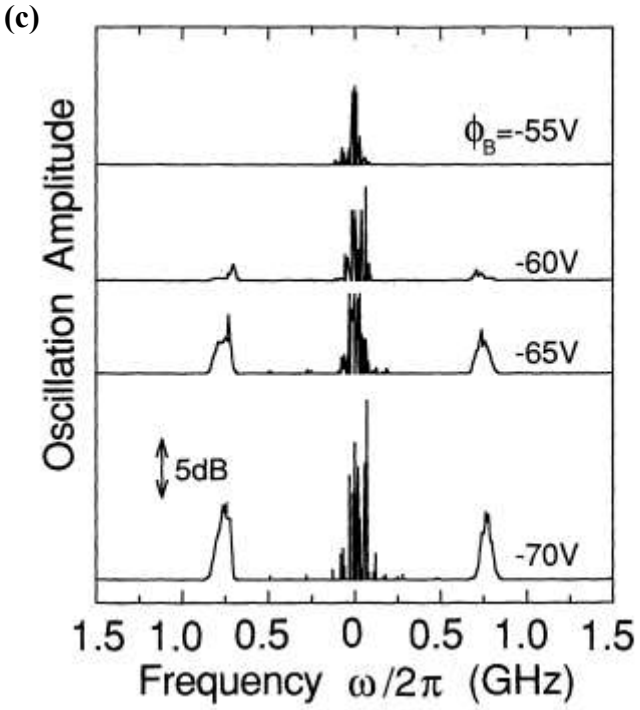


Fig. 1.2 Structures of (a) detector, (b) electron emissive filament for driving and detecting plasma, and (c) measurement sample of a plasma oscillation probe.

### 1.3.3 Plasma absorption probe

Plasma absorption probe (PAP) was designed by Kokura et al.[7] measures electron density based upon resonant absorption of surface waves (SWs) excited in a "cavity" at the probe head. The probe consists of a small antenna, enclosed in a dielectric tube which is connected to a network analyzer (NWA) by the help of a coaxial cable. The NWA feeds RF signal to the probe and frequency dependence of power absorption is obtained. Since PAP is completely covered by a dielectric medium (usually quartz) it avoids contamination of the plasma. A schematic diagram of PAP from the original design of Kokura is as shown in Fig. 1.3 (a) and power reflection spectra for different ICP powers obtained is shown in Fig. 1.3 (b).

From Fig 1.3 (b), we can see that the power absorption occurs at two frequency series and are expressed as main absorption and second absorption. These resonant absorptions shift towards higher frequencies with increasing discharge power. Electron density can be obtained from absorption frequency using the following equation

$$n_e\,(cm^{-3}) = 1.24 \times 10^{10}(1 + \varepsilon_d)(\omega_{abs}/2\pi)^2 \quad . \qquad (1.9)$$

where $\varepsilon_d$ is dielectric constant of the tube.

Even though PAP is free from metal impurity release and can be used in reactive plasmas, the probe cannot measure lower electron densities. At lower electron densities ($< 10^{10}$ $cm^{-3}$), the absorption power decreases which causes deterioration of measurement accuracy. Also, broadening of the absorption frequency at high pressure results in difficulty of measurement.

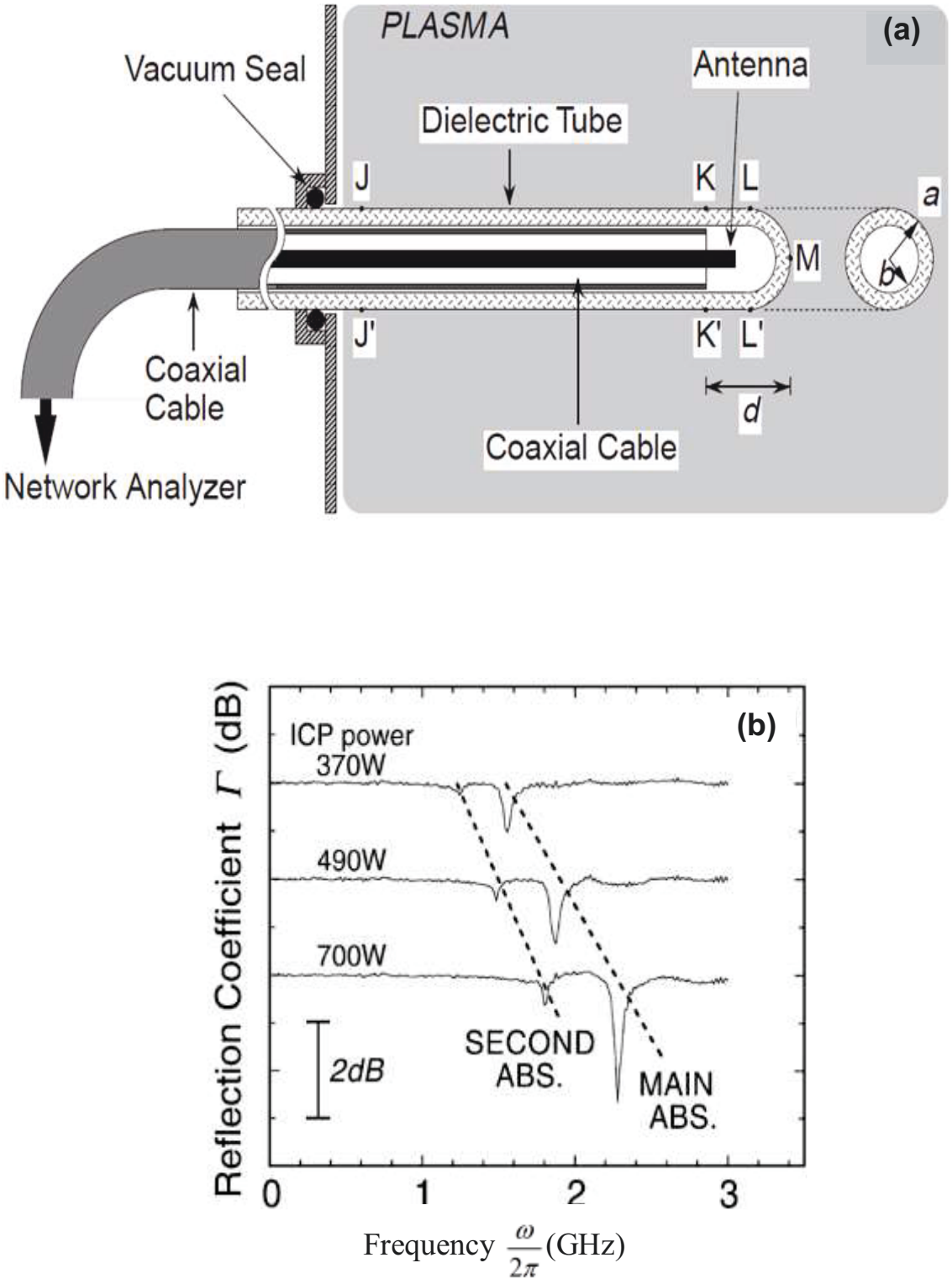


Fig. 1.3 (a) Structure of plasma absorption probe as proposed by Kokura et al. and (b) Reflection coefficient measured using the probe

### 1.3.4 Microwave resonator probe : *hairpin probe*

A hairpin probe is a type of microwave resonator probe, whose resonance depends on the relative permittivity of the medium surrounding it. Microwave resonator probe first introduced by Stenzel[8,9] is also called hairpin probe because its structure resembles to that of a hairpin. It consisted of a quarter-wavelength transmission line shorted at one end and open at the other. The original hairpin probe described by Stenzel in his paper is as shown in Fig. 1.4.

The resonator in Stenzel's design is mounted beyond the end of a 6.35-mm probe shaft through which two high-temperature coaxial cables are inserted. One of the lines is used for exciting the resonator, the other for detecting the signal coupled by the resonator. Magnetic coupling at the short-circuit end is employed so as to leave the sensitive open end free of obstructions. The resonator has a length of 8 mm, wire separation of 2 mm, silver wire diameter 0.1 mm, a vacuum resonance frequency $f_0$=7.45 GHz, and a quality factor about 150. It is mounted between the two magnetic loops (1.5-mm diameter, 4-mm separation) with a droplet of liquid ceramic cement and is thereby electrically floating in the plasmas.

The resonance of hairpin probe takes place when the antenna length coincides with $\lambda/4$ for the wavelength $\lambda$, and the resonance frequency is

$$f_r = \frac{c}{4L\sqrt{\varepsilon}}. \qquad (1.10)$$

where $c$ is the speed of light, $L$ is the length of the resonator from the bottom to the top of the U structure, and $\varepsilon$ is the relative permittivity of the medium surrounding the probe.

In case of vacuum, $\varepsilon$ is unity and the hairpin resonance frequency is simply $f_0 = c/4L$. The relative permittivity of low pressure non-magnetized plasma is

$$\varepsilon = 1 - \frac{f_p^2}{f^2}. \qquad (1.11)$$

where the plasma frequency $f_p / 2\pi = (e^2 n_e / \varepsilon_0 m_e)^{1/2}$, $e$ and $m$ are the electron charge and mass, respectively, and $n_e$ is the plasma electron density. Substituting Eq. (1.11) in Eq. (1.10), we obtain value of the resonance frequency of the hairpin as

$$f_r^2 = f_0^2 + f_p^2 \ . \qquad (1.12)$$

Expressing $f_p$ with the electron density, we can derive a simple formula relating the electron density with frequency difference of $f_r$ (GHz) and $f_0$ (GHz):

$$n_e\left(cm^{-3}\right) = \frac{f_r^{\,2} - f_0^{\,2}}{0.861} \times 10^{10} \ . \qquad (1.13)$$

The original probe designed by Stenzel was bulky and was difficult to construct. Therefore, Hebner[10] introduced a hybrid system that used a coaxial cable loop antenna to excite the resonator and a horn antenna to excite the resonator. R.B.Piejak[11] et al. redesigned the hairpin probe structure as two types: a transmission probe and a reflection probe. The reflection probe unlike a transmission probe consists of only one coaxial cable and hence has less perturbation on the plasma. Since the reflection probe is easy to construct, there has been renewed interest in microwave resonator probe.

Microwave resonator probe enables easy estimation of electron density. However, its construction is complicated and the probe is fragile. Also, the length of the antenna needs to be increased for it to be able to effectively measure a wide range of electron density. On the other hand, inserting bare metal into a plasma causes metal impurity contamination of the plasma.

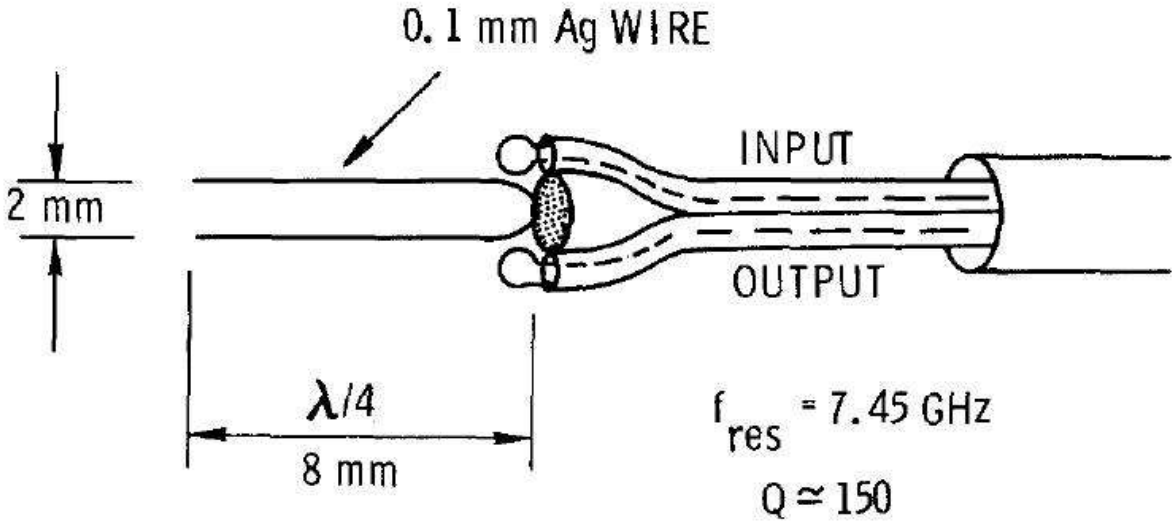


Fig. 1.4 Schematic view of microwave resonator probe developed by Stenzel.[9)]

## 1.4 Summary

In this chapter, some fundamental parameters related to basic understanding of plasma were briefly discussed. Also, some probe techniques used in diagnostics of *cold plasma* were introduced. The most commonly used plasma diagnostic tool i.e., Langmuir probe is easy to construct and operate. However difficulties in interpretation of the probe I-V characteristics pose a major difficulty. One of the other demerits of Langmuir probe being its inability to perform diagnostics in reactive plasmas.

One of the probe diagnostic tool plasma oscillation probe (POP), enables accurate measurement of electron density by observation of plasma oscillation excited by beam instability. But, POP also suffers from metal impurity contamination and relatively short-life time of the hot filament used in it. Plasma absorption probe (PAP) is metal impurity free but its measurement accuracy is severely compromised at low electron density and high pressure. Microwave resonator probe also called hairpin probe enables local measurement of electron density but this technique also suffers from metal impurity contamination and is fragile. A long antenna often creates strong perturbation in the plasma which is also not acceptable in industrial plasma processes.

Apart from the probe techniques mentioned in this chapter, new probes and techniques are continuously being developed to suit individual demands. Such new techniques are mainly inspired by the fact that, none of the existing techniques are perfect and suffer from one or another demerit.

References

1) I. Langmuir and H. M. Smith, *Phys. Rev.* 28, 727–763 (1926)

2) N. Hershkowitz, in *Plasma Diagnostics, Discharge Parameters and Chemistry,* ed. O. Auciello and D. L. Flamm (Academic press, Boston, 1989) p.113

3) F. F. Chen: in *Plasma Diagnostic Techniques*, ed. R. H. Huddlestone and S. L. Leonard (Academic Press, New York, 1965) p. 113.

4) L. Schott, in *Plasma Diagnostics*, ed. by W.L Holtgreven (North-Holland, Amsterdam, 1968), Chap. 11.

5) I. H. Hutchinson, *Principles of Plasma Diagnostics*, (CambridgeU.P., Cambridge, 2002) 2nd ed., p 60

6) T. Shirakawa and H. Sugai, *Jpn. J. Appl. Phys*. 32 (1993)

7) H. Kokura, K. Nakamura, I. P. Ghanashev, and H. Sugai, *Jpn. J. Appl. Phys*., Part 1 38 (1999)

8) R. L. Stenzel : *Rev. Sci. Instrum.* **47**, 603 (1976).

9) R. L. Stenzel, *Phys. Fluids* **19**, 865 (1976).

10) G. A. Hebner and I. C. Abraham, *J. Appl. Phys.* **90**, 10 (2001).

11) R. B. Piejak, V. A. Godyak, R. Garner, B. M. Alexandrovich, and N. Sternberg: *J. Appl. Phys.* 95 (2004) 3785.

# Chapter 2

# Curling Probe for Electron Density Measurement

## 2.1 Introduction

To overcome the short-comings of microwave resonator probe (also called hair-pin probe), a compact slot-type of microwave resonator probe, called *curling probe* (CP)[1)] was developed. A simple model of CP is as shown in Fig. 2.1.

A CP with a spiral slot length of 35 mm is shown in Fig. 2.1. An aperture of 3mm diameter is cut open at the center of the probe head and is excited by a monopole antenna joined to the co-axial cable feeding microwave power. To make the probe metal impurity free, a thin quartz cover (0.1~ 0.2 mm) is placed on top of the spiral slot. The model shown in Fig. 2.1 is just a representative model; several variants of CP with different antenna lengths are available. At present, a probe of minimum cross-section of 6 mm is also in use.

Most of our work was done using probes of 35 mm and 100 mm antenna length. Fig.2.2 shows the side-by side comparison of the two probes. It can be seen that the slot antenna length has been increased by increasing the number of spiral turns and the probe cross-section. Several parameters like gap width $g$, slot width $w$, aperture radius $a$ and probe cross-section $\phi$ can be adjusted to make the probe according to individual needs. A miniaturized probe can in principle be made by minimizing $g$, $w$ and $\phi$.

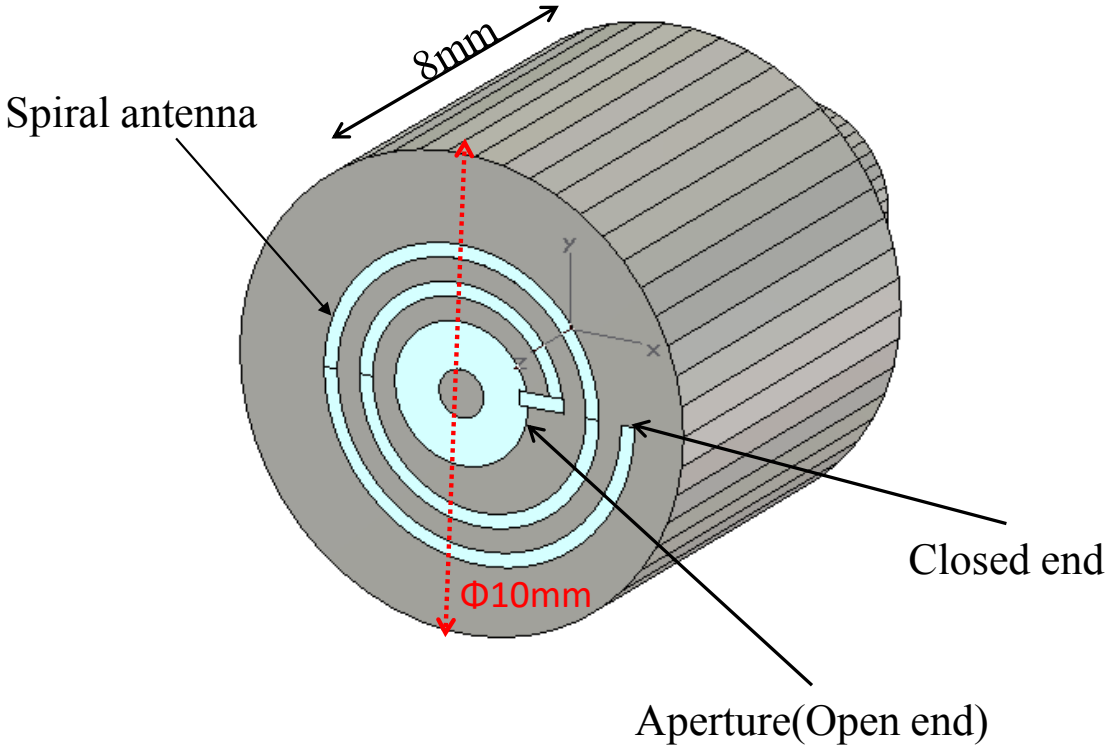


Fig. 2.1 Front-view of curling probe (antenna length 35 mm).

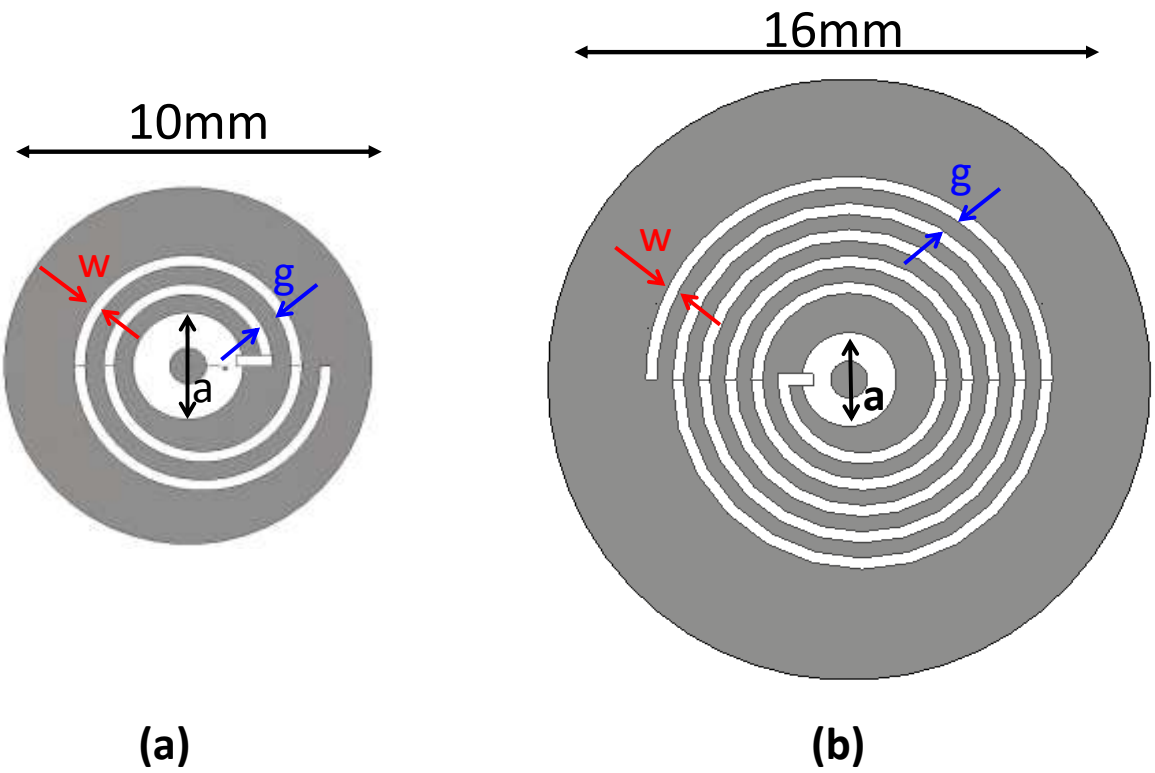


Fig. 2.2 Side by side comparison of (a) 10 mm, and (b) 16 mm probe.

## 2.2 Probe modeling using simulation

CP geometry is different compared to hair-pin probe, therefore Eq. (1.10) used to calculate resonance frequency cannot be directly applied to it. Finite difference time domain (FDTD) simulation using a commercial software Microwave Studio[2)] was performed to see the deviation of CP resonance from theoretical value obtained using Eq. (1.10)

A CP of 100 mm diameter was modeled and simulated in vacuum. Hexahedral mesh with a mesh density of 30 lines per wavelength was used. The simulation result is as shown in Fig. 2.3. The resonance frequency obtained through simulation $f_{simul}$ is approximately 8% different from the theoretically expected value of resonance frequency. Liang et.al[1)] introduced the finite size correction factor $\beta$ to account for the change in geometry. Therefore, the resonance frequency of CP, when immersed in a uniform plasma of permittivity $\varepsilon$ is

$$f_r = \beta \times \frac{c}{4L\sqrt{\varepsilon}}. \qquad (2.1)$$

Since the equation of resonance frequency for CP is different compared to microwave resonator probe, the equation used to measure electron density should also be different, i.e., the electron density in Eq. (1.13) should be corrected by some factor. Liang et al.[1)] performed FDTD simulation in a simple probe model (probe in direct contact with plasma) and used a correction factor $\gamma$ to compensate for the change in probe geometry. The equation to derive electron density for CP can be re-written as

$$n_e\left(cm^{-3}\right) = \gamma \times \frac{f_r^{\,2} - f_0^{\,2}}{0.861} \times 10^{10}. \qquad (2.2)$$

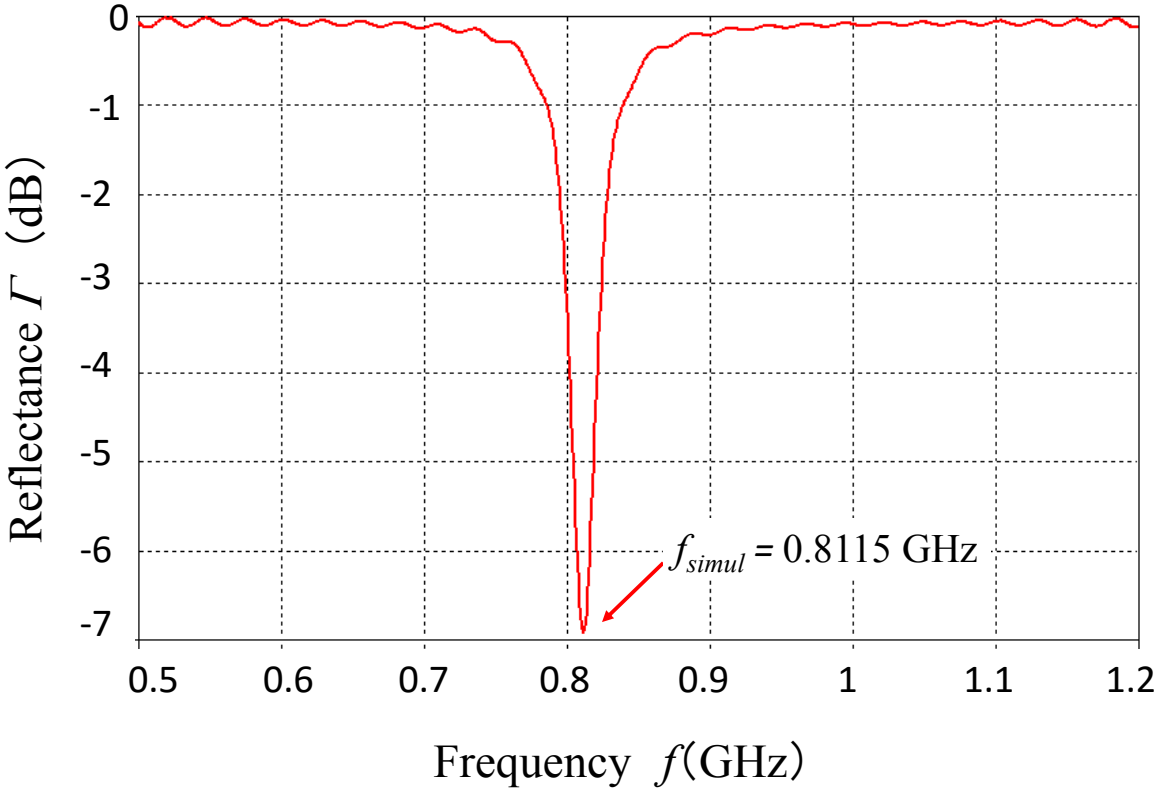


Fig. 2.3 Resonance peak for L = 100 mm probe in vacuum.

## 2.3 Computation of electron density

### 2.3.1 FDTD simulation

FDTD simulation was performed for two probes, i.e., L = 35 mm and 100 mm to find the resonance frequency dependence with electron density. Figure 2.4 (a) shows the resonance frequency shift (increase) with increasing electron density for a 35 mm probe in the simulation. Both probes were simulated in the electron density range of $10^{10}$-$10^{12}$ $cm^{-3}$, the relationship between resonance frequency shift and electron density change for both probes are shown in Fig. 2.4 (b).

By using the resonance frequency vs electron density data in Fig. 2.4 (b) as a reference, the electron density can be easily obtained from the resonance frequency measured in an experiment. However, there are several practical difficulties to this approach. FDTD simulation is very time-consuming and this approach requires performing simulation every-time a new probe is made, which is very impractical. Therefore, an analytical model to estimate the value of γ was developed.

### 2.3.2 Analytical model

A tractable formula for computation of electron density is highly desired. For simplicity let us consider a two layer model of curling probe as shown in Fig. 2.5 (a) where $\varepsilon_{IN}$ and $\varepsilon_{OUT}$ are the dielectric constants of the materials inside and outside the antenna surface, respectively. Then, the average dielectric constant of two layers can be written as

$$\varepsilon_{avg} = \frac{\varepsilon_{IN} + \varepsilon_{OUT}}{2} .$$

Now, the equation for resonance frequency can be re-written by substituting $\varepsilon_{avg}$ in the place of $\varepsilon$ in Eq. (2.1)

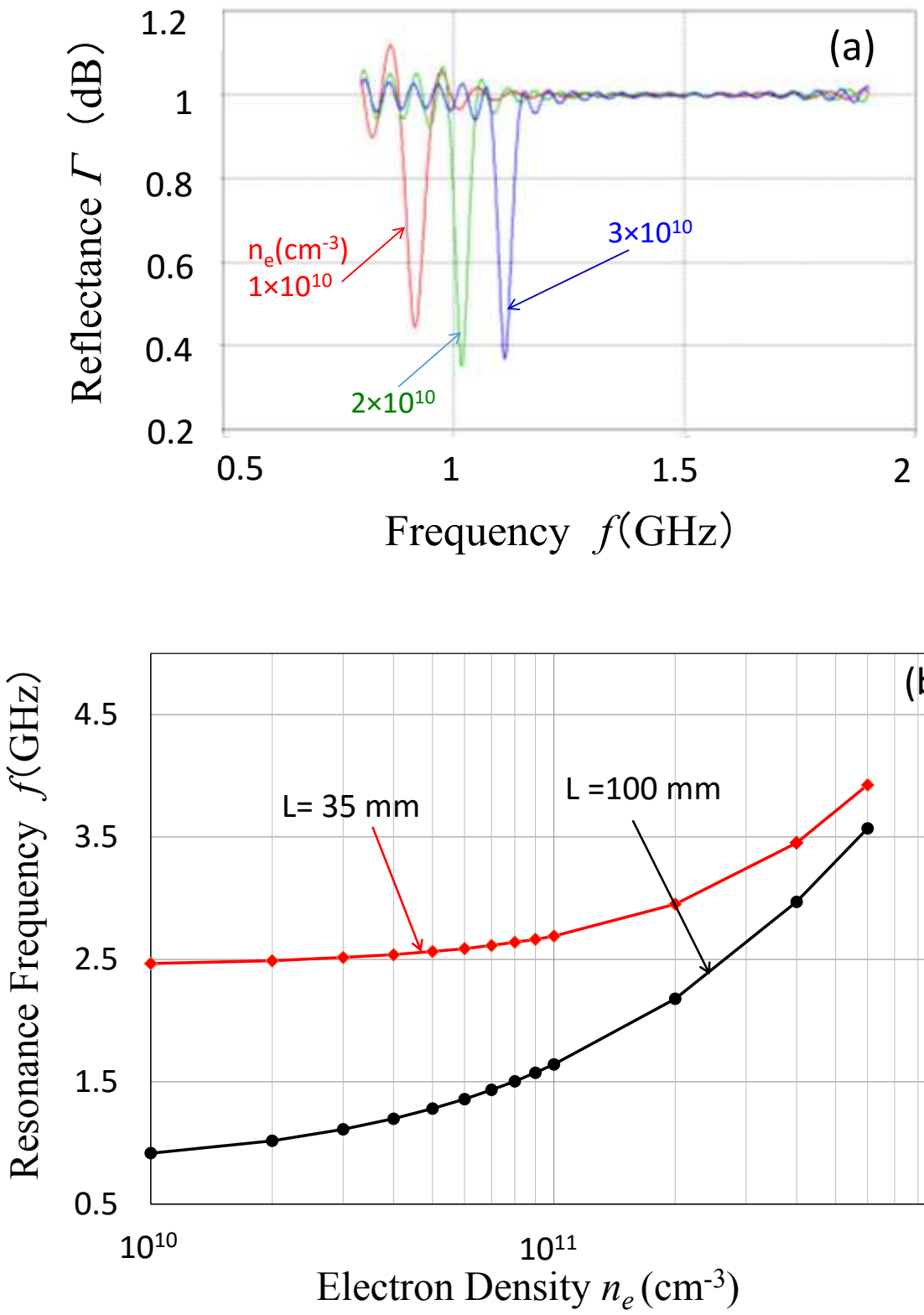


Fig. 2.4 (a) Resonance frequency shift with increasing electron density, (b) Resonance frequency vs electron density plot for 35 mm and 100 mm probe.

$$f_r = \beta \times \frac{c}{4L}\sqrt{\frac{1}{\varepsilon_{avg}}} \quad . \qquad (2.3)$$

When a medium outside the antenna is heterogeneous and non-uniform as *ε(z)* with the *z*-axis normal to the antenna plane (*z* = 0), we define the average dielectric constant $<\varepsilon_{OUT}>$, integrating ε(z) along the z-axis, as

$$<\varepsilon_{\mathrm{OUT}}>=\int_0^\infty \varepsilon(z)g(z)dz \quad . \qquad (2.4)$$

where *g*(*z*) is a weight function with $\int_0^\infty g(z)dz = 1$. By replacing $\varepsilon_{OUT}$ with $<\varepsilon_{OUT}>$, the resonance frequency can be expressed as

$$f_r = \beta \frac{c}{4L}\sqrt{\frac{2}{\varepsilon_{\mathrm{IN}} + <\varepsilon_{\mathrm{OUT}}>}} \quad . \qquad (2.5)$$

In a real-case scenario, the probe has a thin quartz cover (0.1~0.2 mm) above the antenna to avoid plasma penetration inside the probe. When the probe is inserted into plasma, the probe can be simply considered as consisting of three layers as shown in Fig. 2.5 (b).

The layer below the antenna is generally vacuum (ε = 1). Let us assume that the layer outside of the antenna has permittivity $\varepsilon_2$ and thickness *d*, and another infinitely thick layer of permittivity $\varepsilon_3$. Since the nature of weight function is unknown, FDTD simulation for CP was carried out, revealing exponential decay of the microwave field. Therefore the weight function is expressed as

$$g(z) = \frac{1}{\sigma}\exp(-\frac{z}{\sigma}). \qquad (2.6)$$

where the simulation results showed a best-fit value of σ = 0.4.

(a)

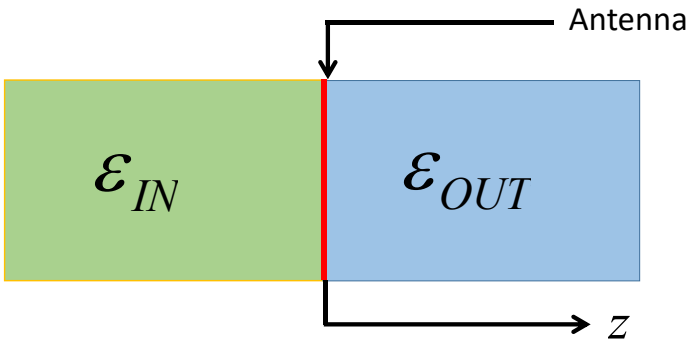


(b)

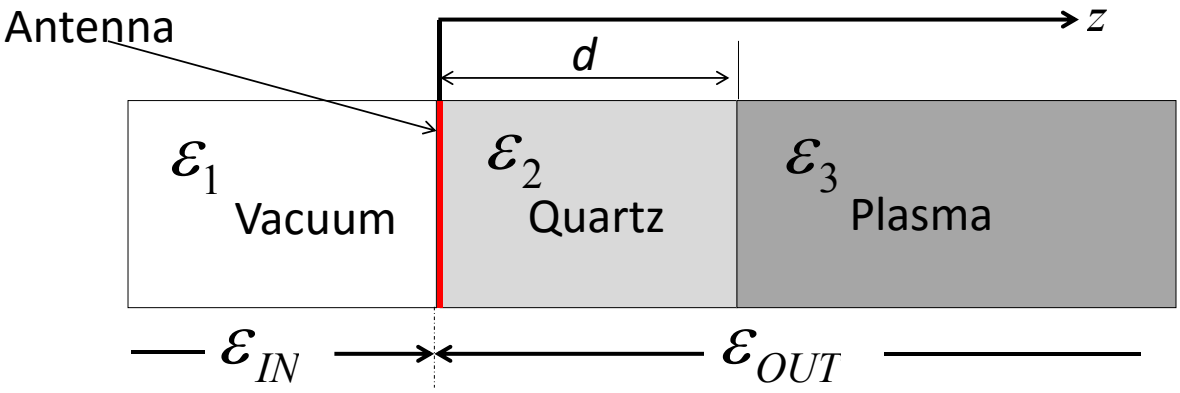


Fig. 2.5 (a) A simplified two layer model, (b) real-case three layered model

In the three layer model of Fig. 2.5 (b), the average dielectric constant of materials outside the antenna can be written as

$$< \varepsilon_{\text{OUT}} >= \int_0^{\infty} \varepsilon(z) \frac{1}{\sigma} e^{-\frac{z}{\sigma}} dz$$

$$= \int_0^{d} \varepsilon_2 \frac{1}{\sigma} e^{-\frac{z}{\sigma}} dz + \int_d^{\infty} \varepsilon_3 \frac{1}{\sigma} e^{-\frac{z}{\sigma}} dz$$

$$= \varepsilon_2 \left[ -e^{-\frac{z}{\sigma}} \right]_0^{d} + \varepsilon_3 \left[ -e^{-\frac{z}{\sigma}} \right]_d^{\infty}$$

$$= \varepsilon_2 \left[ -e^{-\frac{d}{\sigma}} + 1 \right] + \varepsilon_3 \left[ 0 + e^{-\frac{d}{\sigma}} \right]$$

$$\therefore < \varepsilon_{\text{OUT}} >= \varepsilon_2 + \left( \varepsilon_3 - \varepsilon_2 \right) e^{-\frac{d}{\sigma}} \quad . \qquad (2.7)$$

In *discharge off* condition, $\varepsilon_3 = 1$ and hence

$$\therefore < \varepsilon_{\text{OUT}} >_0 = \varepsilon_2 + \left( 1 - \varepsilon_2 \right) e^{-\frac{d}{\sigma}} . \qquad (2.8)$$

Eq. (2.5) can be written as :

$$f_0 = \beta \frac{c}{4L} \sqrt{\frac{2}{\varepsilon_{\text{IN}} + < \varepsilon_{\text{OUT}} >_0}} \quad . \qquad (2.9)$$

During *discharge on* condition, the third layer is plasma, i.e. $\varepsilon_3 = 1 - \frac{f_p{}^2}{f^2}$ .

So, the average dielectric constant outside the probe can be written for $f = f_r$ (resonance frequency) as

$$< \varepsilon_{\text{OUT}} > = \varepsilon_2 + \left(1 - \frac{f_p^{\,2}}{f_r^2} - \varepsilon_2\right) e^{-\frac{d}{\sigma}}$$

$$= \varepsilon_2 + \left(1 - \varepsilon_2\right) e^{-\frac{d}{\sigma}} - \frac{f_p^{\,2}}{f_r^2}\, e^{-\frac{d}{\sigma}} \quad . \tag{2.10}$$

Substituting Eq. (2.8) in Eq. (2.10), we get.

$$< \varepsilon_{\text{OUT}} > = < \varepsilon_{\text{OUT}} >_0 - \frac{f_p^{\,2}}{f_r^2}\, e^{-\frac{d}{\sigma}}. \tag{2.11}$$

Using the resonance frequency $f_r$ in Eq. (2.5), $f_r$ can be written in terms of $f_0$ as

$$f_r = f_0 \times \sqrt{\frac{\varepsilon_{\text{IN}} + < \varepsilon_{\text{OUT}} >_0}{2}} \times \sqrt{\frac{2}{\varepsilon_{\text{IN}} + < \varepsilon_{\text{OUT}} >}}\,.$$

Squaring both sides we get

$$f_r^{\,2}(\varepsilon_{\text{IN}} + < \varepsilon_{\text{OUT}} >) = f_0^{\,2}\ (\varepsilon_{\text{IN}} + < \varepsilon_{\text{OUT}} >_0)\ .$$

Substituting $< \varepsilon_{\text{OUT}} >$ in Eq. (2.11), we get

$$(f_r^{\,2} - f_0^{\,2})\ (\varepsilon_{\text{IN}} + < \varepsilon_{\text{OUT}} >_0) = f_p^{\,2}\, e^{-\frac{d}{\sigma}}\ .$$

Substituting the value of $f_p$ from Eq. (1.7), we get,

$$n_e\left(cm^{-3}\right) = \frac{e^{-\frac{d}{\sigma}}}{(\varepsilon_{\text{IN}} + < \varepsilon_{\text{OUT}} >_0)} \times \frac{f_r^{\,2} - f_0^{\,2}}{0.861} \times 10^{10}\ . \tag{2.12}$$

Comparing this equation with the Eq. (2.2), we find the correction factor

$$\gamma = \frac{e^{-\frac{d}{\sigma}}}{(\varepsilon_{\text{IN}} + < \varepsilon_{\text{OUT}} >_0)}\ . \tag{2.13}$$

For a quartz plate of $\varepsilon_2 = 3.72$, $d$ = 0.2 mm and $\sigma = 0.4$, we obtain the correction factor

$$\gamma = 5.1. \tag{2.14}$$

So, the equation of electron density can be re-written as

$$n_e\left(cm^{-3}\right) = 5.1 \times \frac{f_r^2 - f_0^2}{0.861} \times 10^{10}. \tag{2.15}$$

### 2.3.3 Comparison of analytical value of γ with value obtained from simulation

The correction factor $\gamma$ obtained in Eq. (2.14) through analysis was compared with the value of $\gamma$ obtained through simulation. In simulation, the value of $\gamma$ was calculated from Eq. (2.2) using the resonance frequencies ($f_0, f_r$) simulated for given electron density $n_e$. The value of for L = 35 mm and 100 mm is plotted in Fig. 2.6.

On comparison of the analytical model with simulation, the value of gamma in analytical model was found to be about 17% smaller than simulation for 100 mm probe. Similarly, for 35 mm probe, gamma was 35% smaller in low electron density regime but was in agreement in high density region ($\sim 10^{12}$ cm$^{-3}$). In conclusion, it was found that simulation is essential for high-accuracy measurements.

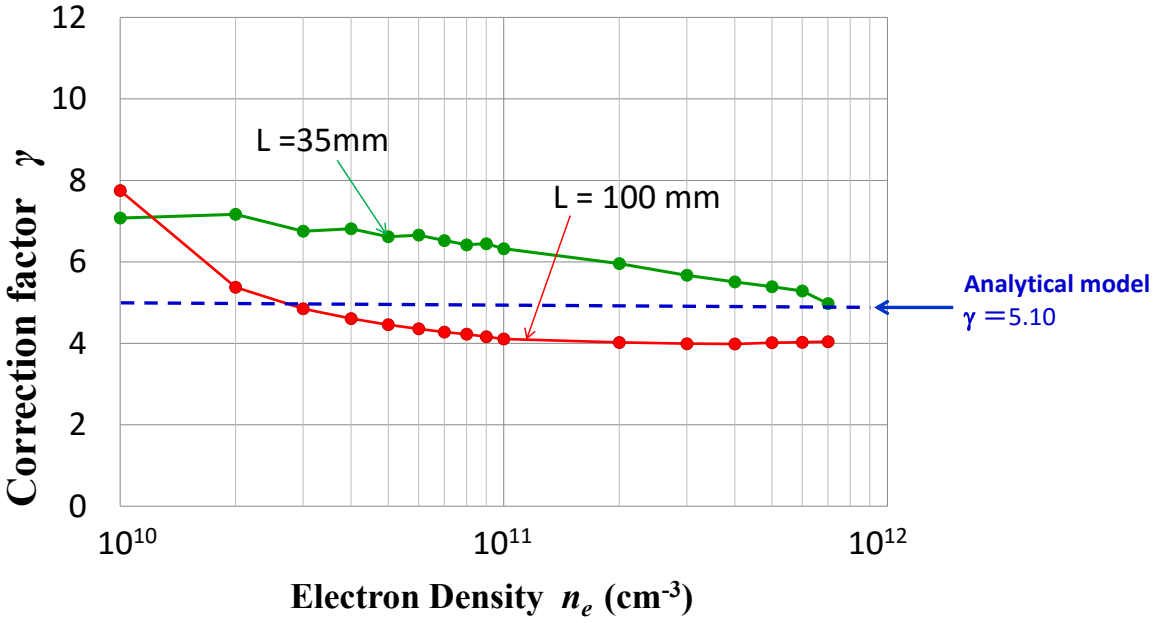


Fig. 2.6 Comparison of γ in analytical model and simulation.

## 2.4 CP correction for sheath influence

### 2.4.1 Using FDTD simulation

The equal number of positive ions and electrons in a plasma gives a unique property called *quasi-neutrality* which was briefly discussed in Chapter 1 of this thesis. The electrons in a plasma are more mobile due to their smaller mass. If a substrate (electrically grounded) is inserted into a plasma, then it will be bombarded by both electrons and ions. Since the flux of electrons is greater the substrate will get charged negatively with respect to the plasma. This causes positive ions in plasma to be attracted and electrons to be repelled from the substrate, finally leading to the formation of a region with net positive charge. This region is called *sheath*. Sheath is formed on the chamber wall surrounding the plasma and also around a probe inserted into the plasma. The thickness of the sheath is some order times the Debye length where Debye length is defined as

$$\lambda_D = \sqrt{\frac{\varepsilon_o k T_e}{e^2 n_e}} \,. \qquad (2.16)$$

From Eq. (2.16) it can be seen that Debye length depends on both electron density and temperature. Chen[3)] mentions that the sheath is about 5 times the Debye length. CP measurements performed are also influenced by sheath effects.

To measure the extent of sheath influence, FDTD simulation of a probe of antenna length 35 mm with a cross-section of 10 mm was performed. At first, a simple model as shown in Fig. 2.7 (a) without considering sheath was simulated. In the second stage, a simulation model as shown in Fig. 2.7 (b) was used. For simplicity the sheath was considered to be a vacuum layer of thickness $5\lambda_D$. CP simulation was carried out at a constant electron temperature

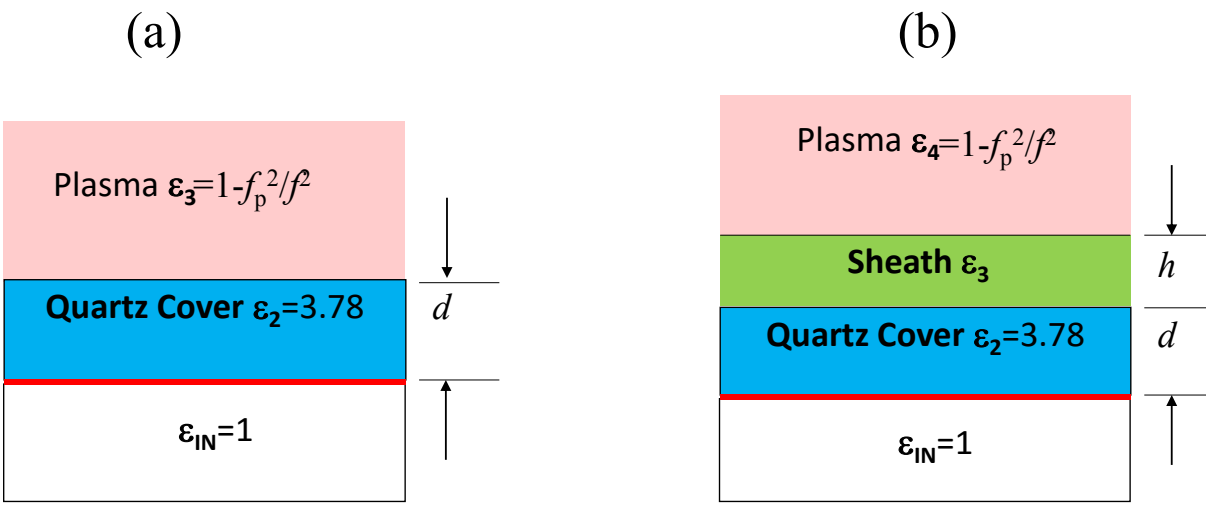


Fig. 2.7 (a) Simulation model without sheath, (b) simulation model with sheath.

$T_e$ = 1 eV, the thickness of quartz cover was considered as 0.2 mm. The thickness of vacuum layer representing the sheath in Fig. 2.7 (b) was made to depend on electron density and temperature. For the simulation, a constant electron temperature of was considered. Both models were simulated by varying the electron density from $10^9$-$10^{12}$ $cm^{-3}$ and the results were compared.

Fig. 2.8 (a) shows the FDTD simulation results of the two models, i.e., with and without sheath. It can be seen that the sheath effect is almost negligible in the electron density region below $10^{11}$ $cm^{-3}$. However, in the region > $10^{11}cm^{-3}$, deviation was observed between the results of with and without sheath.

### 2.4.1 Using analytical model

Apart from FDTD simulation, analytical model treatment of sheath problem using a four layers model was considered. For the analytical treatment, comparison of two conditions i.e. without sheath and with sheath was performed.

Eq. (2.10) gives the average dielectric constant outside probe antenna $<\varepsilon_{out}>$ for a three layer model. But in case of an additional layer of sheath with a thickness $h$ the average dielectric constant outside the probe head can be written as

$$<\varepsilon_{out}>=\varepsilon_2+(\varepsilon_3-\varepsilon_2)\exp\left(-\frac{d}{\sigma}\right)+(\varepsilon_4-\varepsilon_3)\exp\left(-\frac{d+h}{\sigma}\right) \quad .$$

where $\varepsilon_2$= 3.78, $\varepsilon_3$= 1, and $\varepsilon_4$ is plasma dielectric constant which is determined by $f_p$ (plasma frequency) and $f$ (probe resonance frequency).

$$\therefore \; <\varepsilon_{out}> = \; \varepsilon_2 - 2.78\exp\left(-\frac{d}{\sigma}\right) - \frac{f_p^{\,2}}{f^2}\exp\left(-\frac{d+h}{\sigma}\right). \qquad (2.17)$$

The changed value of $<\varepsilon_{out}>$ was used to calculate relationship between electron density and resonance frequency. Fig. 2.8 (b) shows the comparison of analytical results while considering sheath and without sheath. Just like in the simulation, the sheath influence was found to be negligible for electron densities < $10^{11}$ $cm^{-3}$. On further calculation it was found that on an average there is sheath influence in electron density measurement was ~ 5%. Such a small effect can therefore be neglected.

### 2.4.2 Summary

Effect of sheath on CP measurement was studied, by considering a vacuum layer of thickness $5\lambda_D$ and electron temperature of 1 eV. The resonance frequency didn't show any significant shift/change as a result of sheath consideration. However, for proper estimation of sheath influence FDTD simulation with different values of electron temperature is necessary. Also, the simulation result for one probe cannot be used for other probes with different geometry. The simulation considers sheath to be $5\lambda_D$, however, there are limitations to this approach. In very low density plasma, or in magnetized plasma with gyro radii larger than Debye length the sheath can be much thicker.

For sheath correction in an experimental data, beforehand knowledge of electron temperature is necessary. At present, CP can measure only electron density therefore such correction is not possible. More work needs to be done in developing the analytical CP model to compensate for the sheath effects.

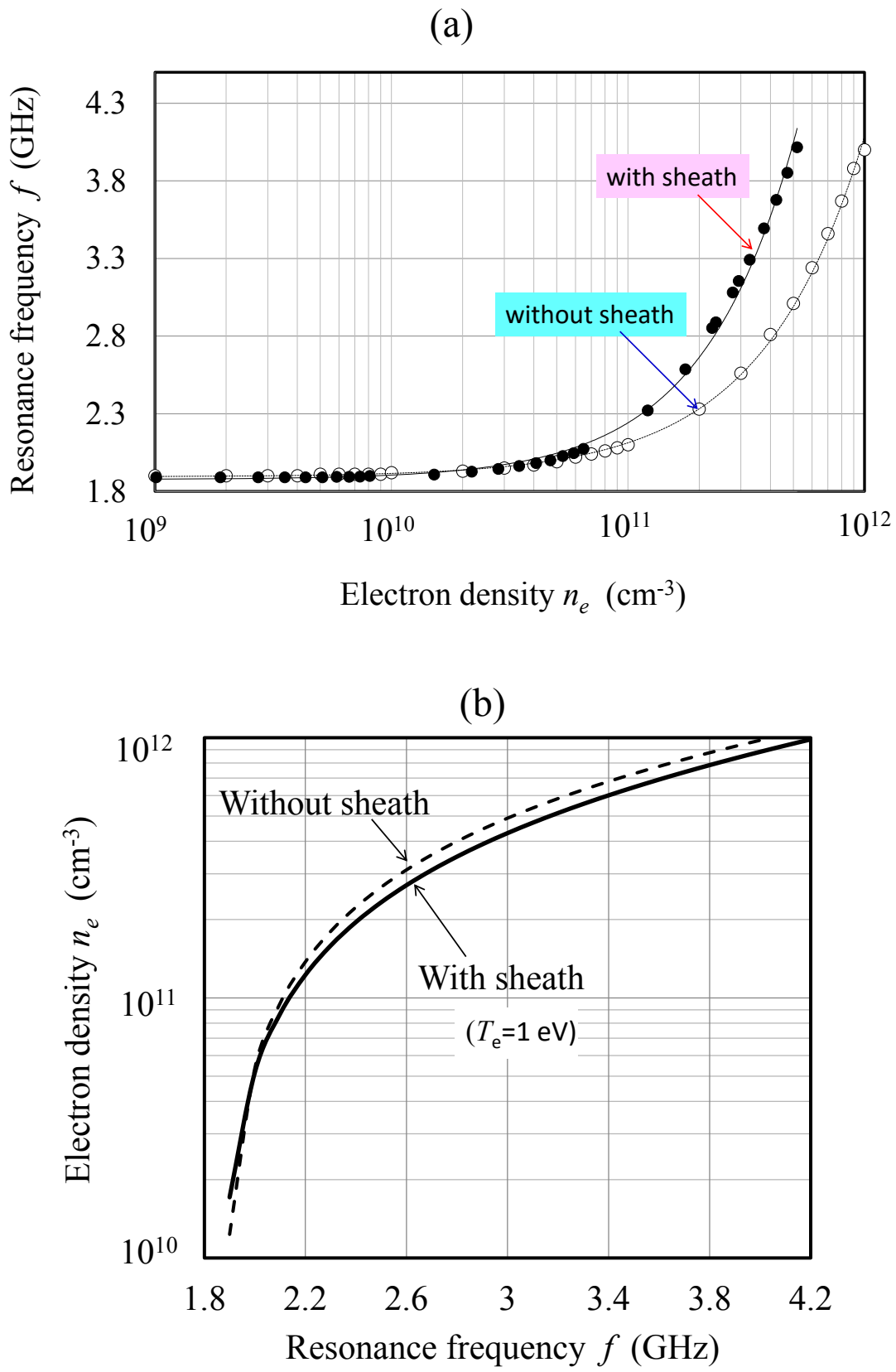


Fig. 2.8 Resonance frequency dependence on electron density with and without sheath in (a) FDTD simulation, and (b) Analytical model

## 2.5 Electron density measurement in inductively coupled plasma (ICP) device

### 2.5.1 Introduction

While performing experiments, CP is inserted into the discharge chamber through a port in the chamber wall. The CP is connected with a network analyzer (NWA) operated in *reflectance mode*, by a co-axial cable. The microwave signal from the NWA excites the spiral slot antenna, on which resonance occurs. At resonance frequency, there is a loss of power, which is seen as a dip in reflectance in reflection spectrum.

$$\text{Reflectance}\left(\Gamma\right) = \log\left(\frac{\textit{Reflected Power}}{\textit{Incident Power}}\right) \qquad (2.18)$$

CP measures electron density based upon resonance frequency shift from *discharge off* to *discharge on* condition. So, during an experiment CP resonance before *discharge on* should be taken. After obtaining the resonance frequency at any particular discharge condition, Eq. (2.15) is used to obtain the electron density.

CP has been developed so that measurements could be performed in any kind of reactive gas discharge. For this purpose two types of probes were developed as shown in Fig. 2.9.

The probe on the left-hand side of Fig. 2.9 is alumina coated such that it is corrosion resistant when used in reactive plasmas. The yttria-coated probe on the right hand-side has a ceramic co-axial cable due to which it can operate up to ~ 600$^{o}$C.

### 2.5.2 ICP discharge apparatus and measurement procedure

The experimental setup is as shown in Fig. 2.10(a). The discharge chamber is 50 cm in diameter and about 15 cm in height. CP was inserted from the side port of the chamber and connected with a NWA. The probe is moveable and hence can be used for spatial measurements.

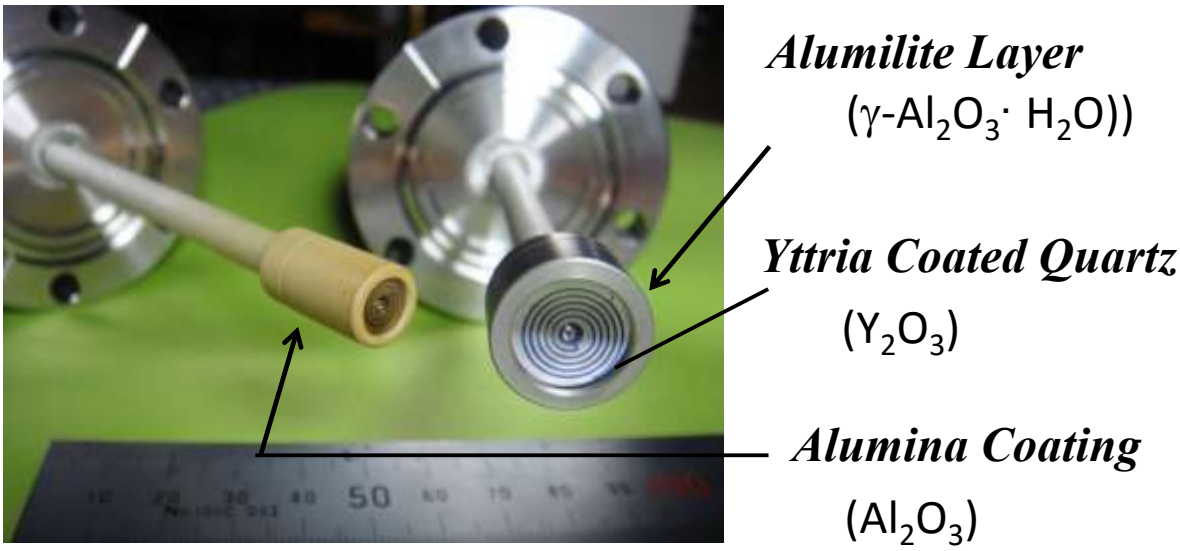


Fig. 2.9 Curling probe variants for use in reactive plasmas.

(a)

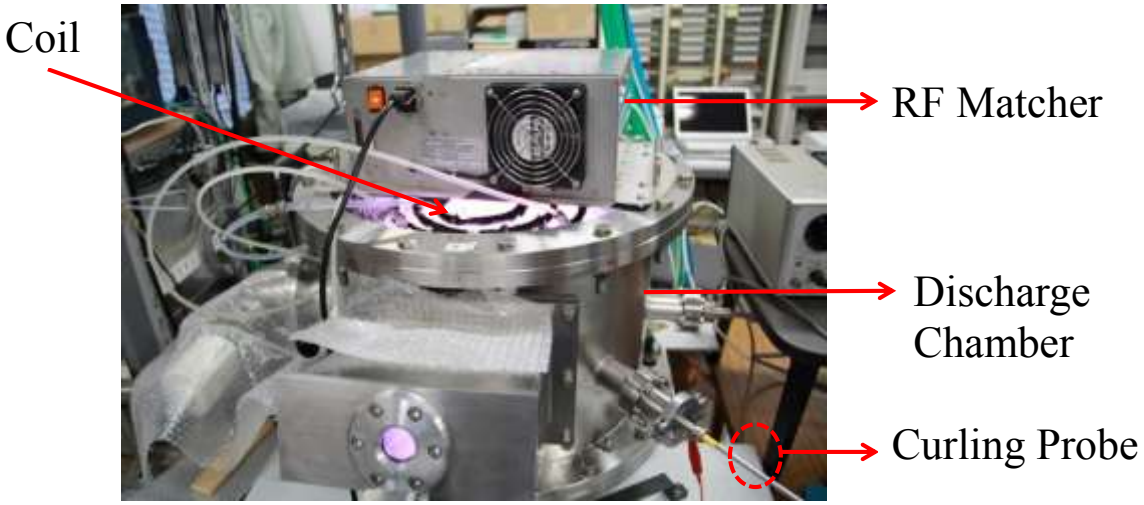


(b)

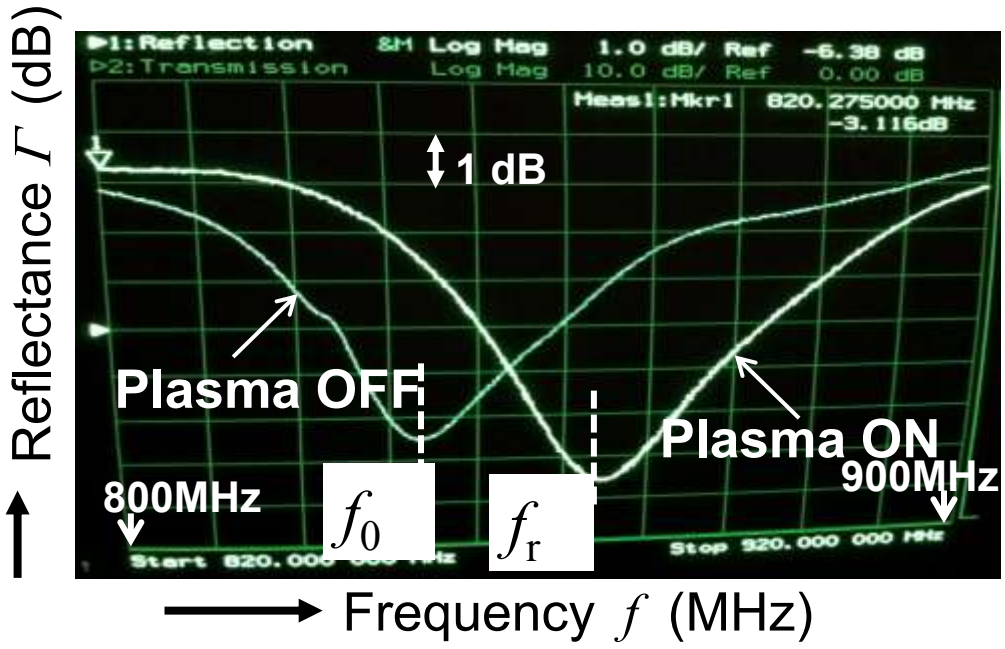


Fig. 2.10 (a) ICP device, (b) Reflectance spectra obtained in Ar 9 Pa discharge.

RF discharge frequency of 13.56 MHz was used and discharge was typically produced in argon in a pressure range of 1-1000 Pa.

A typical reflectance signal obtained in a steady state plasma is shown in Fig. 2.10 (b). In the figure, $f_0$ and $f_r$ are the resonance frequencies in *plasma off* and *plasma on.* In this particular condition, the values were found to be 854 MHz and 874 MHz respectively. Using the value of $f_0$ and $f_r$ in Eq. (2.15), the electron density was calculated to be $1.76 \times 10^9$ cm$^{-3}$. The same approach can be used to measure electron density in any other discharge condition.

### 2.5.3 Power dependence on electron density

Liang et al. observed two kinds of resonances using CP, named as high frequency (HF) and low frequency (LF) resonance. HF resonance occurs at the antenna plane and low frequency (LF) resonance on the slot hole.[1)] LF resonance appears at high electron densities where surface waves are excited by the monopole antenna. So, the electron densities computed using LF resonance agree well with the electron densities computed with surface wave resonance $f_{SWR}$ given as[4,5)]

$$n_e = \frac{1+\varepsilon_d}{0.806} f_{SWR}^2 \times 10^{10} \ (cm^{-3}). \qquad (2.19)$$

where $\varepsilon_d$ is the dielectric constant of material surrounding the probe.

Fig. 2.11 shows the resonance spectra obtained at different discharge power. At low discharge power, only one type of resonance frequency viz., HF resonance was observed but as the discharge power was increased both LF resonance and HF resonance were observed. Fig. 2.12 (a) shows the HF and LF resonance frequencies obtained in an experiment. To measure the electron densities, the equation obtained by the best-fitting the curve in Fig. 2.8 was used.

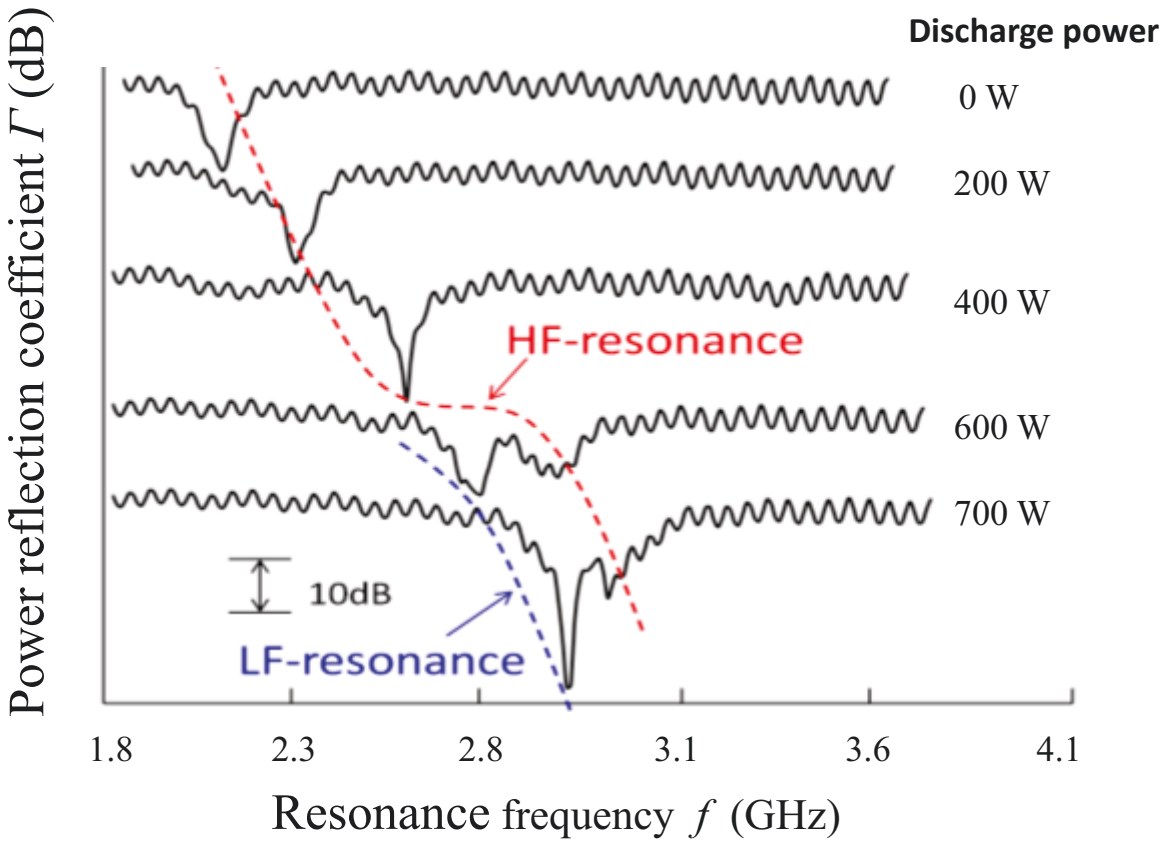


Fig. 2.11 High frequency and low frequency resonances observed during experiment.

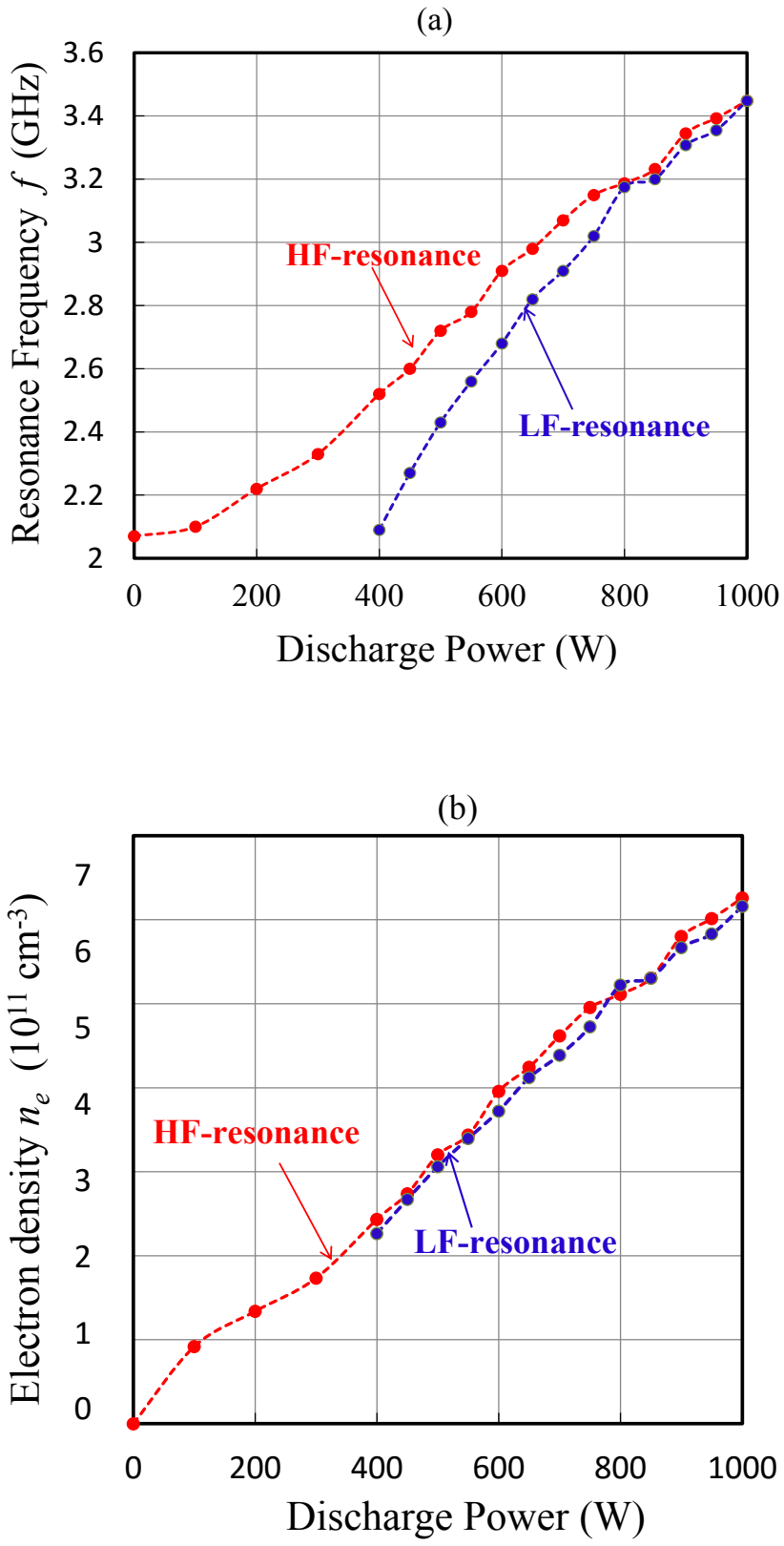


Fig. 2.12 (a) Measured HF and LF resonances, and (b) electron densities measured with HF and LF resonance.

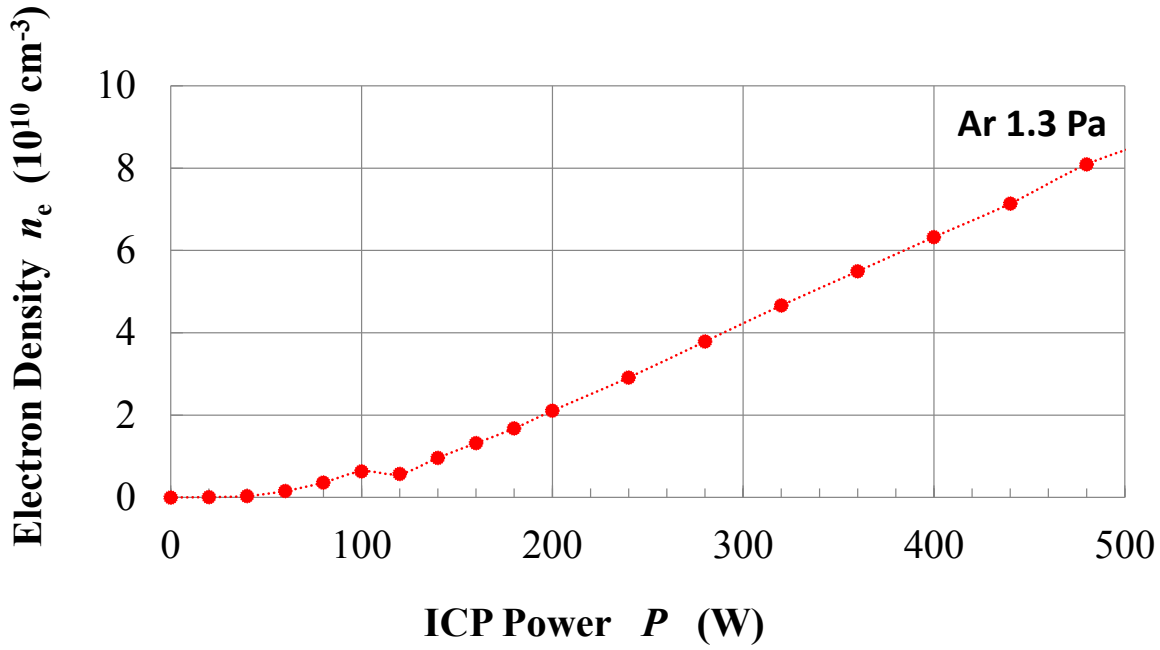


Fig. 2.13 Electron density dependence on discharge power.

Figure 2.12 (a) shows the resonance frequency dependence on discharge power. The electron densities measured using the resonance frequencies obtained from Fig. 2.12 (a) is as shown in Fig. 2.12 (b). It can be seen that both HF resonance and LF resonance yield almost same value of electron density. In other words, electron density can be calculated using any one of the resonance frequencies, either HF or LF.

Similar results were obtained for CP of 100 mm antenna length. Fig. 2.13 shows the electron density measured by varying discharge power (up to 500W) in Ar discharge at 1.3 Pa.

### 2.5.4 Effect of RF-bias on the substrate

In an ICP device the bottom electrode can be powered by a separate RF source (400 kHz, < 500 W) to control ion bombardment energy. A study of electron density variation under RF bias on substrate was performed. The experimental setup is as shown in Fig. 2.14. A planar coil, supplied with inductive power at 13.56 MHz, generates the plasma through a quartz window.

A wafer ($\phi$ 300 mm) was clamped electrostatically to a chuck which is cooled by helium gas. A floating probe was used to measure the plasma potential oscillation and the high-voltage probe was used to measure the wafer voltage.

The ion bombardment energy was controlled by applying RF bias voltage of 400 kHz in argon discharge at 1.3 Pa. CP positioned at the center of the chamber was used to measure the electron density variation for varying RF bias (< 500 W) for discharge power of 150 W.

Fig. 2.15 (a) shows the effect of RF bias on electron density. The electron density was found to decrease with increasing RF-bias power. It is mainly because of power loss resulting from ion bombardment of the wafer. This result is consistent with findings by other researchers[6].

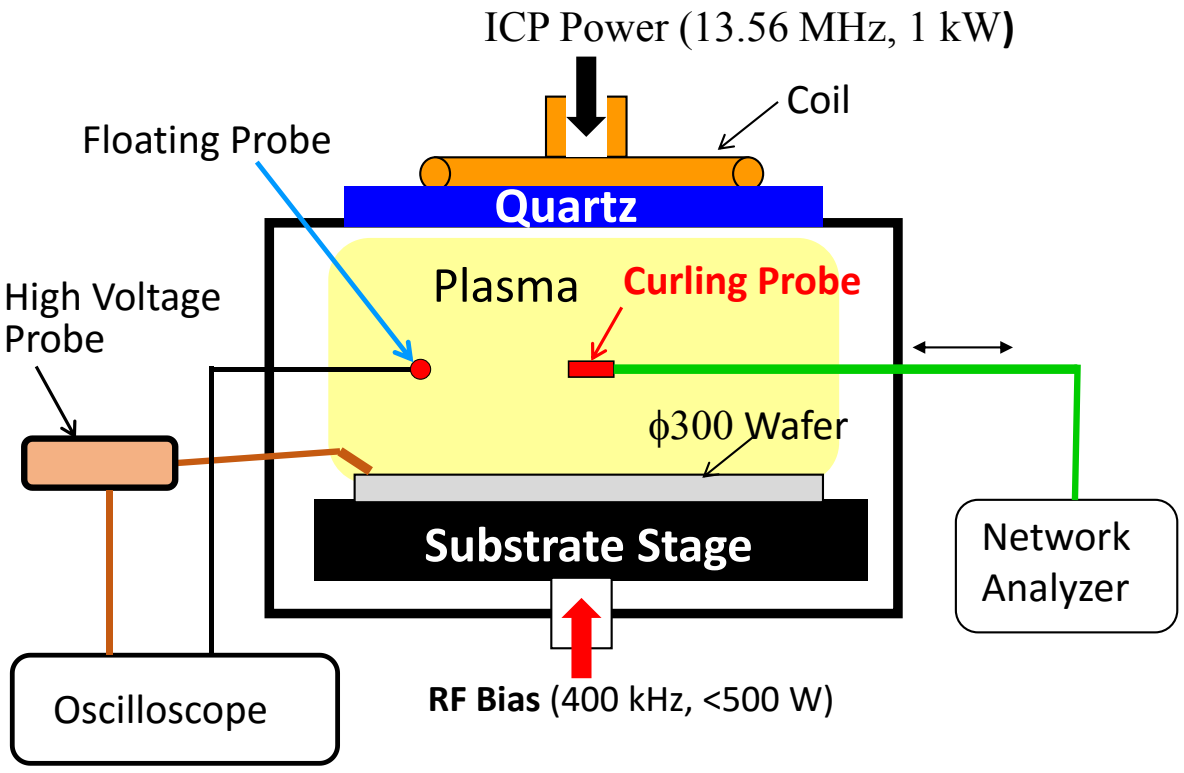


Fig. 2.14 Cross-section view of experimental setup to observe effect of RF-bias.

Similar results i.e. decrease in electron density was obtained at discharge power of 300 W. The plasma potential oscillation at RF-bias of 400 kHz was found to be as small as ~6 $V_{pp,}$ but the wafer voltage was found to be several times 100 $V_{pp.}$

DC wafer voltage $V_{DC}$ was also measured at different ICP discharge power by changing the RF-bias power. $V_{DC}$ was found to decrease more and more negatively due to applied RF-bias. Larger $V_{DC}$ was found to be induced by RF-bias at smaller ICP power as shown in Fig. 2.15 (b). The plasma potential oscillation caused by RF-bias power was also investigated using floating probe and oscilloscope. The relationship showing wafer voltage and floating potential for applied RF-bias power is shown in Table 2.1.

| **RF-bias Power** | **Wafer Voltage** | | **Plasma Potential** | |
|---|---|---|---|---|
| | 400 kHz component | DC component | DC component | 400 kHz component |
| 0 W | 0 | 0 | 0 | ~+8 V |
| 40 W | 200 $V_{pp}$ | ~+4 V | 6 $V_{pp}$ | ~+4 V |
| 80 W | 420 $V_{pp}$ | ~+8 V | 7 $V_{pp}$ | ~+8 V |
| 120 W | 560 $V_{pp}$ | -7V | 8 $V_{pp}$ | ~+8V |

Table 2.1 Wafer Voltage and floating potential dependence on RF-bias power

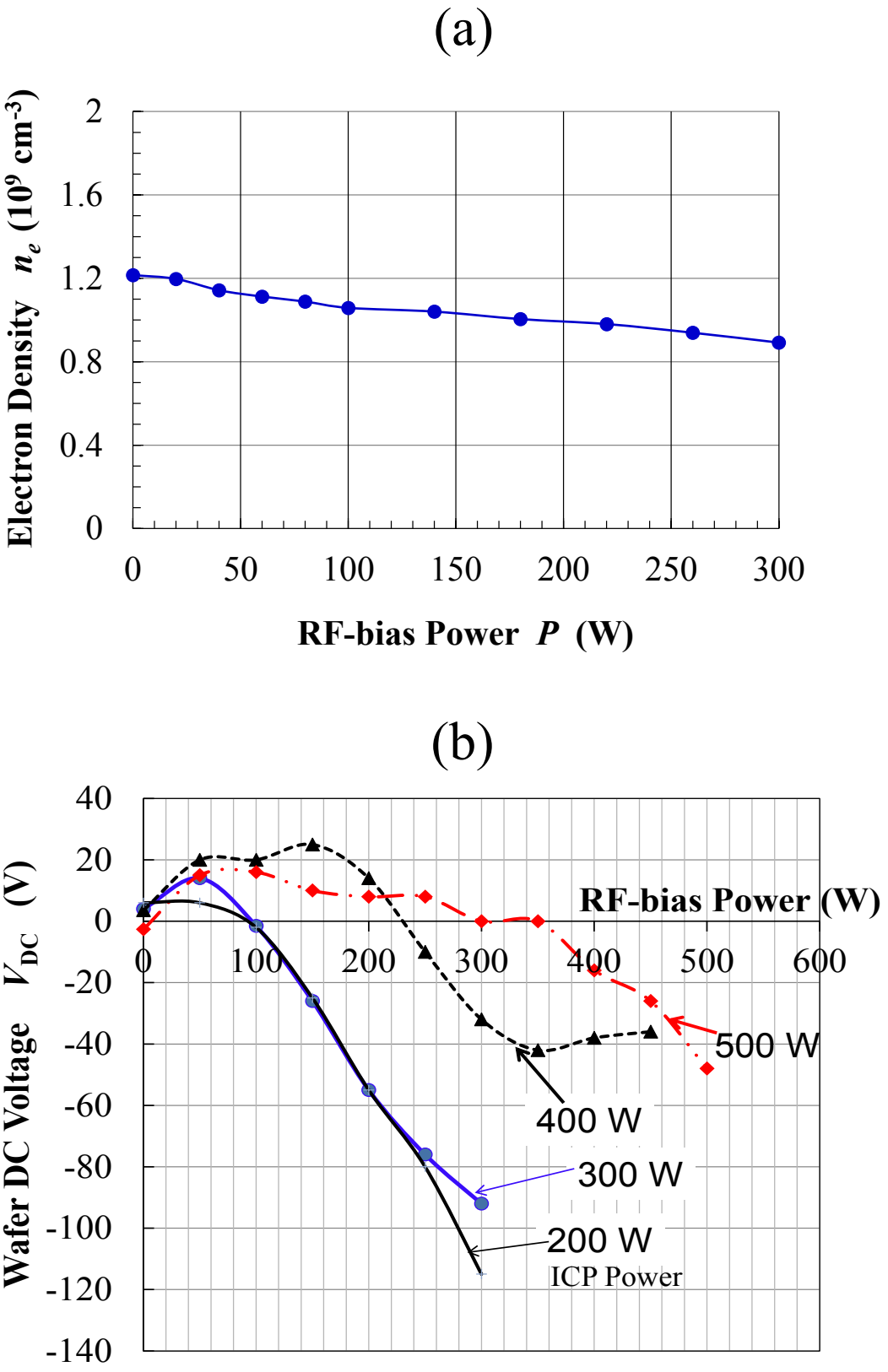


Fig. 2.15 Electron density dependence on RF-bias power, (b) wafer DC voltage dependence on RF-bias power

## 2.6 Summary

In this chapter, curling probe (CP) a modified form of microwave resonator probe was introduced. Due to the change in geometry of CP, the formula to calculate the electron density was changed using analytical approach. The correction factor $\gamma$ was also calculated through FDTD simulation and a comparison with analytical model was made. The new formula (with correction factor was $\gamma$ ) then used to measure electron density in an ICP device. The dependence of electron density on RF-bias power, wafer bias voltage and plasma potential oscillation was investigated. Electron density was found to increase with increasing discharge power when no RF-bias was applied. However, electron density decreased with increasing RF-bias power. The plasma potential oscillation caused by RF-bias was found to very small, but the wafer voltage was found to increase by several orders of magnitude.

Reference


1) I. Liang, K. Nakamura, and H. Sugai: *Appl. Phys. Express* **4** (2011) 066101.

2) https://www.cst.com/products/CSTMWS

3 F. F. Chen: in *Plasma Diagnostic Techniques*, ed. R. H. Huddlestone and S. L. Leonard (Academic Press, New York, 1965) p. 5.

4) H. Kokura, K. Nakamura, I. P. Ghanashev, and H. Sugai, *Jpn. J. Appl. Phys*., Part 1 38 (1999)

5) M. A. Lieberman and A. J. Lichtenberg, *Principles of Plasma Discharges and Materials Processing* (Wiley, New York, 2005) 2nd ed., p. 529.

6) H.C. Lee, M.H. Lee, and C.W. Chung : *Appl. Phys. Lett* **96**, 071501 (2010).

# Chapter 3

# Development of Opto-Curling Probe

## 3.1 Introduction

A brief discussion of probe diagnostic techniques was made in Chapter 1. Probe techniques are invasive diagnostic tools, i.e. probes are directly inserted into the plasma which causes perturbation in the immediate vicinity of the probe. Therefore some remote diagnostic techniques have been developed, one of them is *optical spectroscopy*[1)]. Optical diagnostics are powerful tools for non-invasive measurement of the properties of chemically complex discharges[2)]. Optical spectroscopy involves measurement of light emitted from the plasma as a function of wavelength, time and position. Optical spectroscopy can be classified as *active spectroscopy* and *passive spectroscopy*.

Passive spectroscopy involves observation of emissions from the plasma, e.g. Doppler shift, Stark broadening, Zeeman effect. Whereas, in active spectroscopy the atoms in plasma are excited to observe adsorption or emissions. Charge exchange recombination spectroscopy, beam emission spectroscopy (BES), laser induced fluorescence (LIF), absorption spectroscopy are some examples of active spectroscopy.

A conventional *curling probe* (CP) can only measure electron density which leaves out important information on radical species in the plasma. Therefore, the existing CP was modified to make a new type of probe called *opto-curling probe*, such that both electron and radical species can be monitored at the same time.

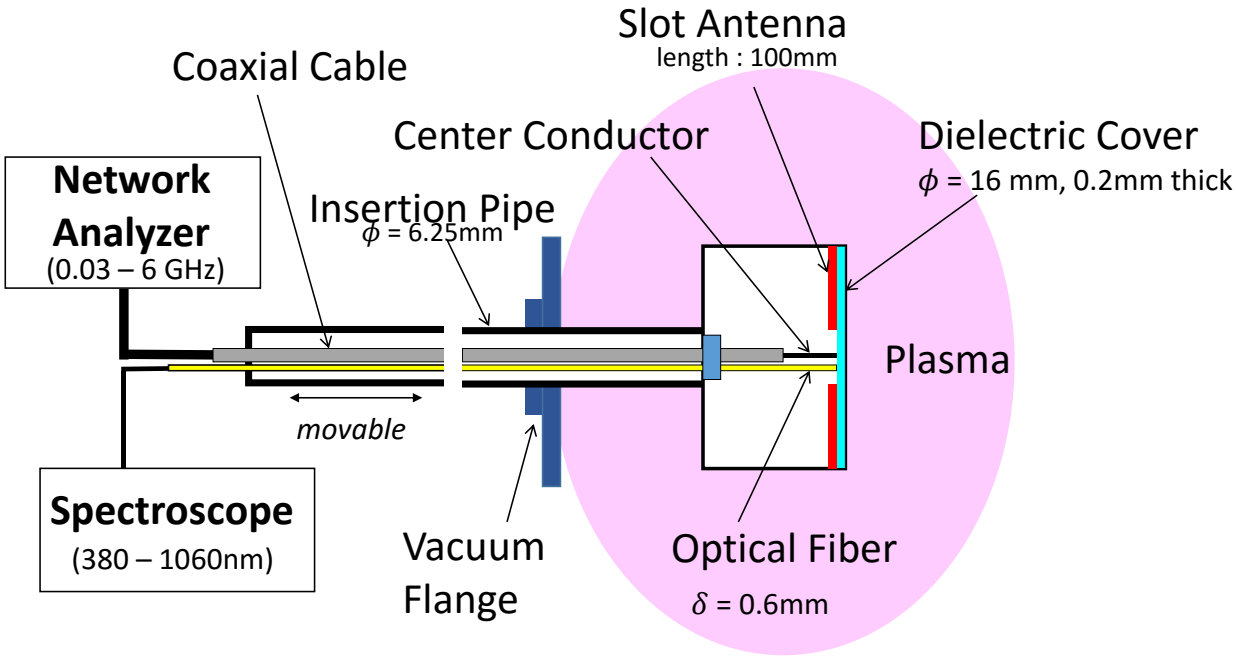


Fig. 3.1 Schematic of opto-curling probe.

## 3.2 Construction and design of opto-curling probe

*Opto-curling* probe (Opto-CP) consists of a *conventional CP*[3)] mounted with an optical fiber. To construct an Opto-CP, a conventional CP with spiral antenna length of 100 mm and a probe head diameter of 16 mm with a 3 mm diameter coupling aperture was taken. An optical fiber was installed parallel to the coaxial cable along an insertion pipe via a vacuum flange, positioning the fiber end within the antenna central hole, i.e. coupling aperture. The antenna is covered with a thin dielectric material, usually quartz plate of thickness 0.2 mm.

The co-axial cable exciting the antenna was connected to a network analyzer (NWA) and the optical fiber was connected to a spectroscope. The optical emission signal is guided by the optical fiber to a spectrometer. A detailed schematic of Opto-CP is shown in Fig. 3.1.

In the probe design shown in Fig. 3.1, the optical fiber is of diameter $\delta$ = 0.6 mm which collects the light emitted from the plasma within a cone angle of 25°.

### 3.2.1 Sensitivity of optical fiber

A simple experiment was performed to measure the detection sensitivity of the optical fiber. A small light source, i.e., a ball lamp of 5 mm diameter was moved in *z*-direction along a straight optical fiber. The optical intensity $I_d$ was measured as a function of the separation distance between the optical fiber and the ball lamp over a range of $z$ = 5 – 100 mm. The data points plotted in log-log scale lie on a straight line, indicating a relation $I_d \propto \frac{1}{z^2}$ . The experimental set-up and the result is shown in Fig. 3.2. The results obtained in Fig. 3.2 is reasonable because the optical fiber detects luminous flux emitted from a point source, in this case a ball lamp, within a solid angle specified by the optical fiber cross-section area as $\frac{\pi(\delta/2)^2}{z^2}$. As a result, the optical fiber detects 100 times more photons emitted from $z$ = 5 mm than those from

$z$ = 50 mm. To sum up, the optical fiber predominantly picks up photons very near the fiber tip (within a few millimeters).

## 3.3 Determination of radical density

Optical emission spectroscopy (OES) along with actinometry technique is generally used to obtain radical densities in the plasma. When an electron collides with an atom *A,* the atom can jump to a higher energy state (excited state). If an atom A from ground state $E_g$ is excited to state $E_x$. A photon is released when the atom de-excites and returns to a lower energy state $E_l$. The energy of the emitted photon is given by

$$\Delta E = E_x - E_l \qquad (3.1)$$

The photon energy in terms of wavelength can be written as $\Delta E = \frac{hc}{\lambda}$ , where $h$ and $c$ are Planck's constant and speed of light.

Let us consider that a species X of the ground state density $n_X$ is excited by electron of the density $n_e$ and decays due to spontaneous emission in plasma. Assuming corona equilibrium, the optical emission intensity $I_X$ of the species X is given by[1)]

$$I_X = u k_X n_X n_e \qquad (3.2)$$

where $u$ is a proportional constant, and the excitation rate coefficient $k_X$ is expressed as

$$k_X = \int_0^\infty \sigma_X(\varepsilon)\sqrt{\frac{2\varepsilon}{m_e}}F(\varepsilon)d\varepsilon \qquad (3.3)$$

for the electron-impact excitation cross-section $\sigma_X$, the electron energy $\varepsilon$, and the electron energy distribution function $F(\varepsilon)$. Following Eq. (3.3), the optical emission intensity is proportional to the radical density, the electron density, and the excitation rate coefficient. These complex dependences can be simplified introducing actinometry technique[4,5)].

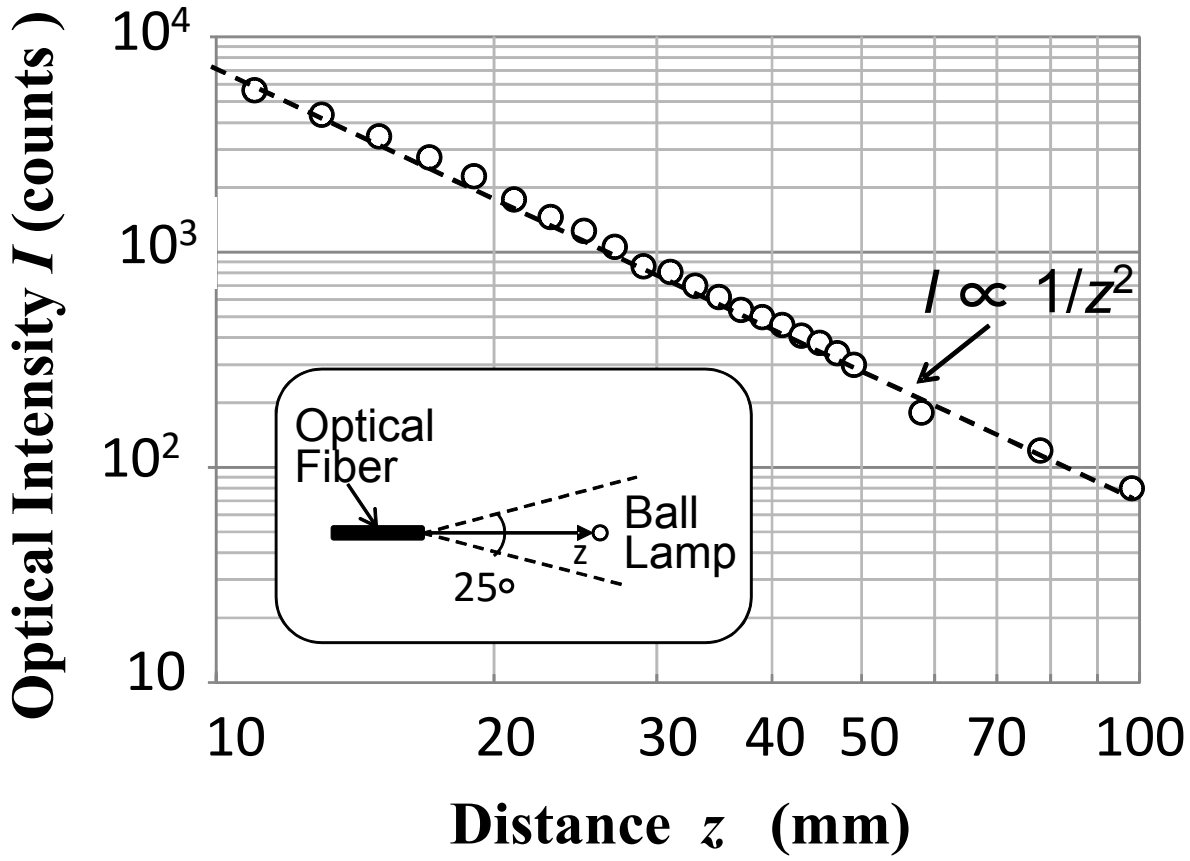


Fig. 3.2 Measurement of optical fiber sensitivity.

In actinometry technique, a trace of rare gas (usually argon) is added into plasma, and the argon emission intensity $I_A = u' k_A n_A n_e$ expressed in the same manner as Eq. (3.3) is measured along with the radical emission intensity $I_X$. Taking the ratio of $I_X$ to $I_A$, one can eliminate the electron density $n_e$, finding the radical density as

$$n_X = (\frac{u' k_A}{u k_X}) n_A (\frac{I_X}{I_A}) . \qquad (3.4)$$

The absolute radical density can be obtained if the ratio of $u' k_A$ to $u k_X$ is known. However, there have been many arguments on the measurement accuracy of absolute density, concerning the different excitation cross-sections ($\sigma_A$, $\sigma_X$) integrated over a non-Maxwellian electron energy distribution function. As long as the relative radical density is concerned, the actinometry is a simple and convenient calibration method, assuming negligible perturbation accompanied with rare gas mixing.

We can use Opto-CP as an alternative calibration technique. Opto-CP gives both the local electron density and the local intensity of optical emission at the same location (~ a few mm from the probe surface). Therefore, dividing the OES intensity $I_X$ in Eq. (3.2), by the electron density $n_e$, we can obtain the radical density $n_X$ as

$$n_X = \frac{1}{u k_X} (\frac{I_X}{n_e}) . \qquad (3.5)$$

The technique of using OCP is superior because addition of rare-gas is not required. Also, OCP can be moved easily to obtain spatial distribution of radical density.

## 3.4 Application of opto-curling probe

Opto-CP was used to monitor CVD and cleaning process carried out in a 500-mm-diam microwave plasma device where the discharge frequency is 2.45 GHz with the incident power < 2.5 kW. A 300-mm-diameter quartz plate with 161 hollows of 8 mm in diameter and 8 mm in depth was used in the discharge device. The details of the device and its merits have already been discussed elsewhere[6]. $CH_4$ for carbon layer deposition and $O_2$ for cleaning of carbonized wall, at the discharge pressure of ~10 Pa were used.

An Opto-CP of 16 mm in diameter was inserted from a bottom port with the probe head positioned at 150 mm from the multi-hollow quartz plate as shown in Fig. 3.3. When the discharge gas is methane ($CH_4$), carbon thin film is deposited everywhere including Opto-CP head, the thickness of which is maximum around the top plate (multi-hollow plate). In the experiments, the maximum thickness of the amorphous carbon layer was less than 200 nm. Such thin films don't effect the performance of Opto-CP. Also, the absorption coefficient of C:H layer[7] is in the visible range (~2 eV) is ~$10^4$ $cm^{-1}$ which gives only 20% reduction in the optical emission intensity for a 200 nm thick carbon layer.

However, during a long-time CVD process, plasma wall interactions give rise to recycling, re-deposition, particle formation, and eventually flaking of carbon layer. These unfavorable phenomena lead to degradation of carbon film quality and a lack of repeatability in volume production. To avoid such troubles and keep the high repeatability of process, *in situ* plasma cleaning of the chamber wall is frequently carried out to reset the wall condition to the initial state.

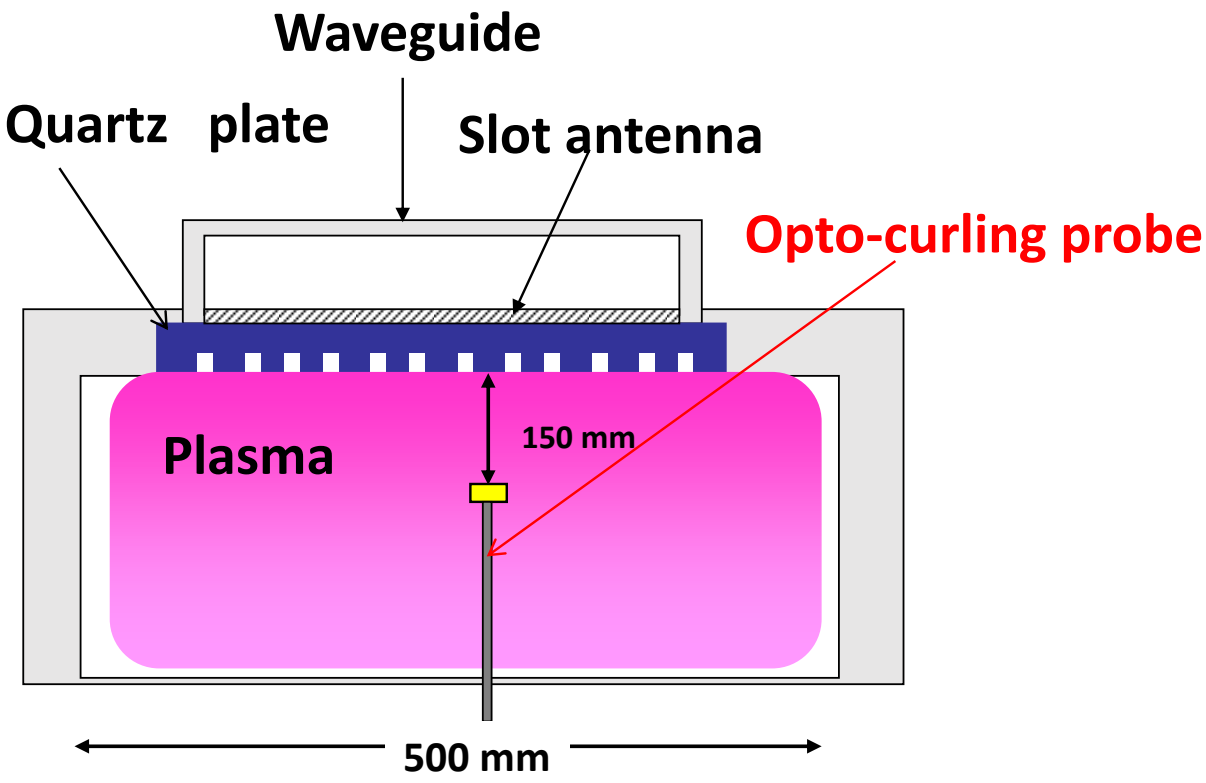


Fig. 3.3 Discharge apparatus for plasma CVD and cleaning.

The experiments were divided into two stages. In the first stage a 10 min methane discharge at room temperature was carried out to deposit carbon layer on the inner chamber wall, whose hydrogen content is usually 30–50 % as designated hydrogenated amorphous carbon (a-C:H) film[7]. In the second stage, oxygen gas was introduced at 10 Pa in the same chamber and the 700 W cleaning discharge was turned on to remove the deposited carbon layer. Abundant oxygen atoms generated by electron-impact dissociation of $O_2$ molecule react with a-C:H layer, yielding $H_2O$ and CO molecules desorbed from the carbonized wall. As shown in Fig. 3.4, the OES measurement during the cleaning discharge shows several emission lines from H atom ($H_\alpha$: 656.28 nm, $H_\beta$: 519.80 nm, $H_\gamma$: 434.05 nm), and electronically excited CO* (519.80 nm) in addition to excited O*(777.19 nm), which are representative species detected in OES[1]. Relatively large emissions at 526.5 nm, 569.3 nm and 597.3 nm were unidentified which survived with almost same intensities after the long $O_2$ plasma cleaning.

After the startup of cleaning discharge, the color of discharge changed from grayish white (typical water vapor discharge) to transparent blue (typical pure $O_2$ discharge), suggesting a time variation of species desorbed from the wall. The emission intensities of $H_\alpha$, $H_\beta$ and CO* are observed to considerably decrease in time as shown in Fig. 3.5 (a) although the O* emission remains almost constant. After ~45 min, both emission intensities diminished to noise levels. Using the Opto-CP, the electron density was measured at the same time as shown in Fig. 3.5 (b). Here the electron density was derived from Eq. (2.15) using the measured resonance frequencies $f_0$ and $f_r$.

It should be noted in Fig. 3.5 (b) that the electron density is very low in the early phase of cleaning discharge. This is probably because a lot of power is consumed to decompose huge

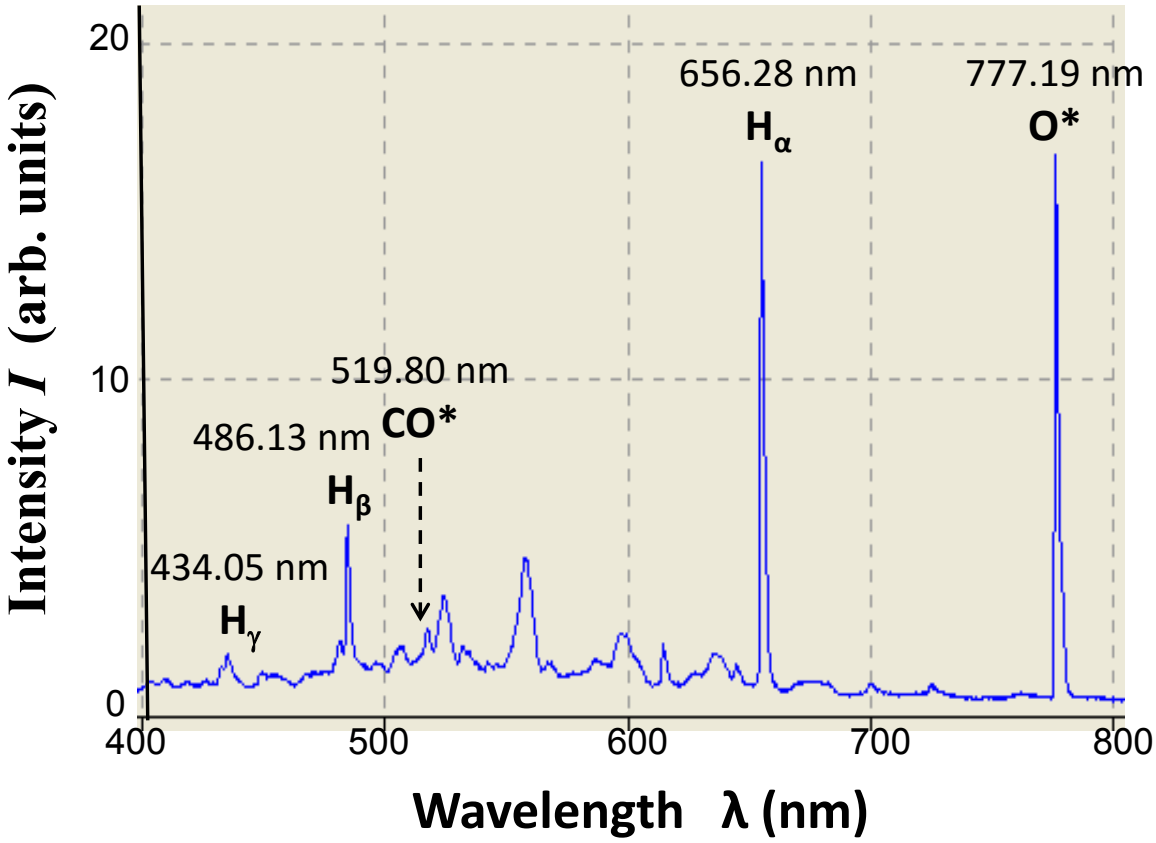


Fig. 3.4 Optical emission spectra of OCP at the early stage of $O_2$ plasma cleaning of a C:H- deposited wall at 700 W, 10 Pa.

amount of $H_2O$ and CO molecules desorbed from the wall. These etch products diminish with the progress of discharge cleaning, and the electron density increases to the saturation level at $t$~45 min.

This saturation level is almost same as the electron density obtained in pure $O_2$ discharge in a clean chamber without carbon layer deposition: $n_e = 4.0 \times 10^9$ cm$^{-3}$ for 800 W and $O_2$ 10 Pa in Fig. 3.5 (b). By using Figs. 3.5 (a) and 3.5 (b) the endpoint of cleaning discharge can be determined as ~ 45 min in the present experiment.

As mentioned in Eq. (3.3), the optical emission intensity $I_x$ is proportional to both the density $n_x$ and the electron density $n_e$. Therefore, dividing the intensity $I_x$ by $n_e$ at the identical position, enables one to obtain the density $n_x$ from Eq. (3.4). The Opto-CP data in Fig. 3.5 show the values of $I_x$ and $n_e$ at the same position at the same instant, so that temporal variations of H-atom and CO-molecule densities during the discharge cleaning of carbonized wall can be deduced as shown in Fig. 3.6. In the Fig. 3.6, the optical emission intensities of $H_\alpha$ and CO* lines are also plotted in open dots, to compare with the emissive species density of H-atom and CO-molecule indicated by solid dots. As shown in Fig. 3.6 (a), the ground state density of H-atom normalized by its initial density decreases more sharply than the normalized $H_\alpha$ line intensity. For example, the H-atom density at the cleaning time of 10 min is ~1/3 of the normalized $H_\alpha$ intensity. A similar phenomenon was observed for CO-molecule as well.

In the experiments, Opto-CP was moved to obtain spatial distribution of radical density. This technique is valid because the electron density can be considered almost uniform in case of low pressure discharge. However, it will not be easy to obtain the absolute value of radical density from Eqs. (3.3) and (3.5) because the electron impact cross-section $\sigma_x$ is unknown in most cases, and partly because measurement of the electron energy distribution function $F(\varepsilon)$ is difficult in reactive plasma. Assuming Maxwellian type of electron energy distribution

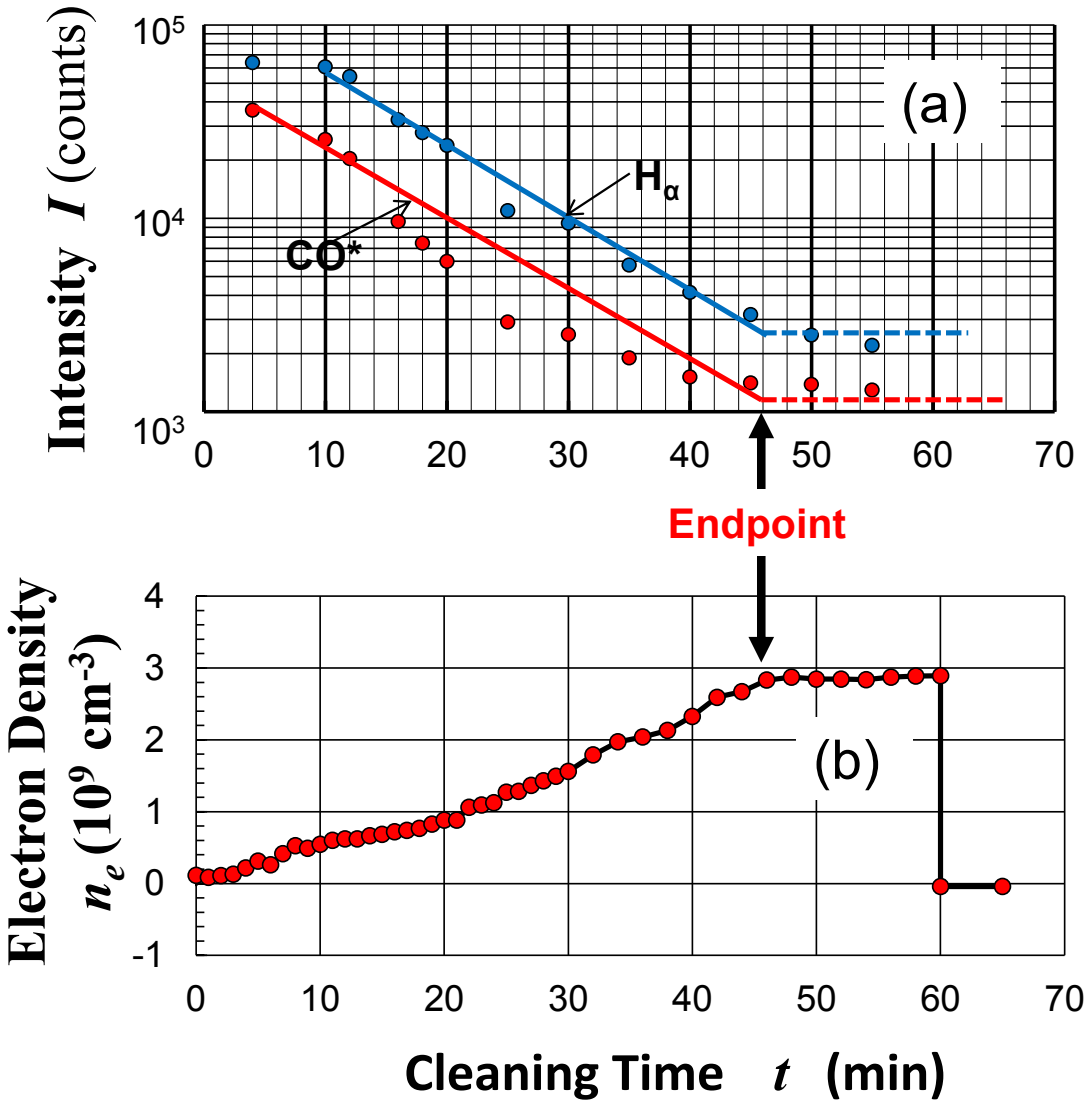


Fig. 3.5 Time variation of (a) optical emission intensities of $H_\alpha$ and CO* and (b) electron density during the $O_2$ cleaning at 700 W and 10 Pa.

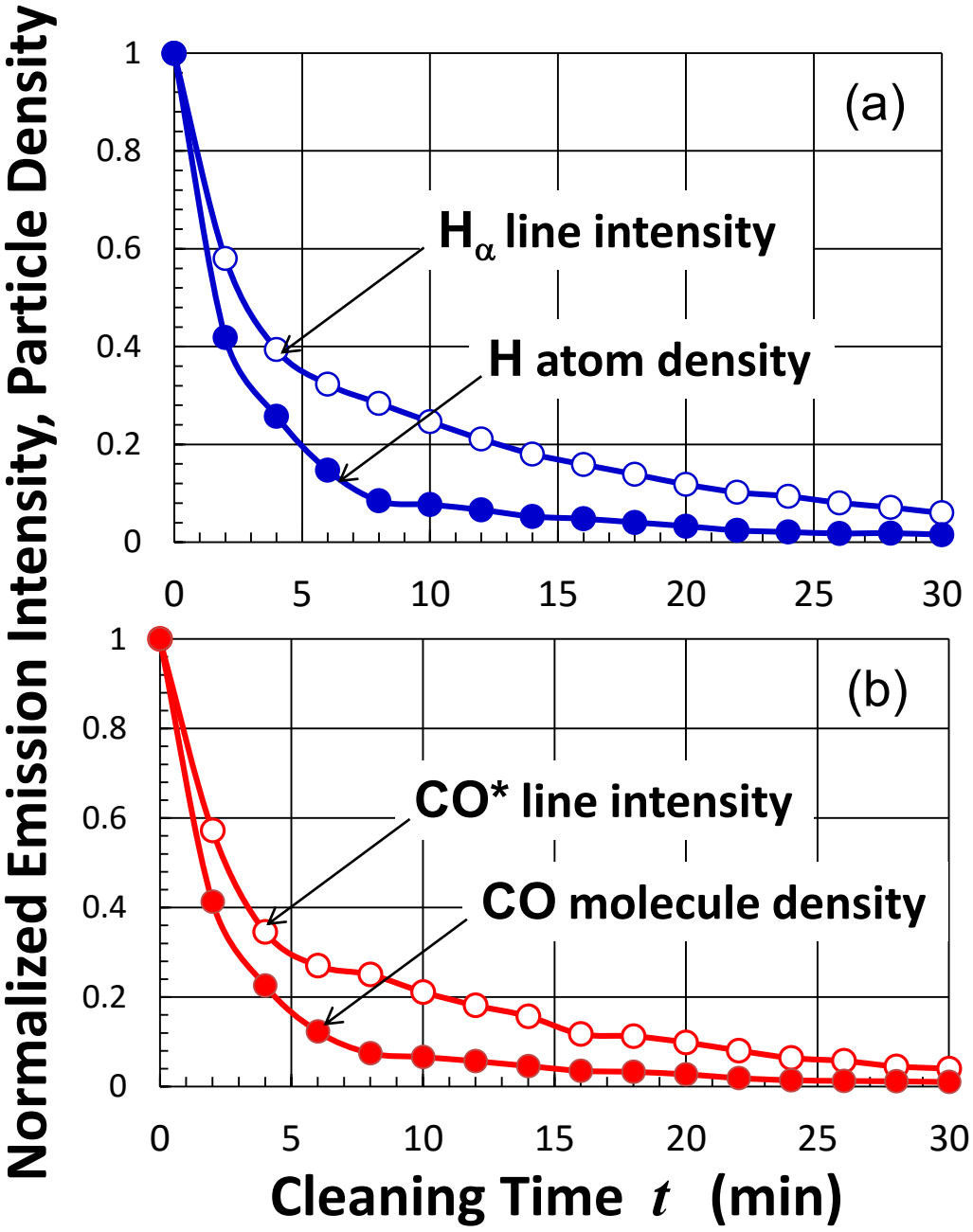


Fig. 3.6 Time variations of optical emission intensity and emissive species density normalized with the initial value for (a) H atom and (b) CO molecule in the experiment in Fig. 3.5.

function, the electron temperature can be evaluated in low-pressure reactive plasma using advanced actinometry[5] (multiple rare gas OES).

## 3.5 Summary

In this chapter, an advanced robust probe called *opto-curling probe* (Opto-CP) is presented, which enables simultaneous space-resolved monitoring of both OES and electron density in reactive plasma. The electron density is obtained from the microwave resonance frequency of a small antenna while the OES data is obtained through an optical fiber installed inside the probe. Without relying on actinometry, the relative density of radical species can be monitored, by taking the ratio of the optical emission intensity of relevant radical to the electron density. The usefulness of Opto-CP was experimentally demonstrated in oxygen plasma cleaning of the discharge chamber whose inner wall was in advance deposited with carbon thin layer during methane plasma CVD. The endpoint of chamber cleaning was clearly observed, and the temporal variations of the H-atom density and CO-molecule density were also successfully observed.

References

1) I. P. Herman: *Optical Diagnostics for Thin Film Processing* (Academic Press, San Diego, 1996).

2) M.A. Lieberman and A.J. Lichtenberg, *Principles of Plasma Discharges and Materials Processing* (Wiley, New York, 2005) 2nd ed., p.274

3) I. Liang, K. Nakamura, and H. Sugai: *Appl. Phys. Express* **4** (2011) 066101.

4) J. W. Coburn and M. Chen: *J. Appl. Phys.* **51** (1980) 3134.

5) M. V. Malyshev and V. M. Donnelly: *J. Vac. Sci. & Tech.* **A15** (1997) 550.

6) I. Liang, S. Ohta, K. Kato, K. Nakamura, I.P Ganachev, and H. Sugai : Ind. Appl. Plasma Process **3** (2011) 61.

7) J. C. Angus, P. Koidl, and S. Domitz: in *Plasma Deposited Thin Films*, ed. J. Mort and F. Jansen (CRC Press, Florida, 1986) p. 106.

# Chapter 4

# On-sweep Mode of CP Measurement in Pulsed Glow Discharge

## 4.1 Introduction

Most of the early pioneering works on gas discharges were carried out at low pressure in a glass tube consisting of a cathode and anode. A typical voltage-current characteristics of DC low pressure discharge tube is as shown in Fig. 4.1[1)]

In a DC glow discharge, the potential drop across the cathode sheath is typically of several hundred volts which can be utilized to bombard ions and deposit materials on the cathode.[2)] DC glow discharges have also been used for metal nitridation which enhances the physical property of a material and makes it corrosion and wear resistant.

Pulsed glow discharge plasma operated in the abnormal glow region is used for metal nitridation of surfaces. Pulsed plasma is used because it can be operated at higher peak voltage and current compared to a dc glow discharge. Also, arcing is a serious problem in metal nitridation process which can be suppressed by carefully adjusting the duty cycle ratio of the pulse power. The abnormal glow region of glow discharge is chosen because the glow seam completely covers the work-piece material placed on the cathode surface.[3)]

Unlike a steady state plasma where electron density remains unchanged with time, the measurement of time varying electron density in pulsed plasma is a challenging task.

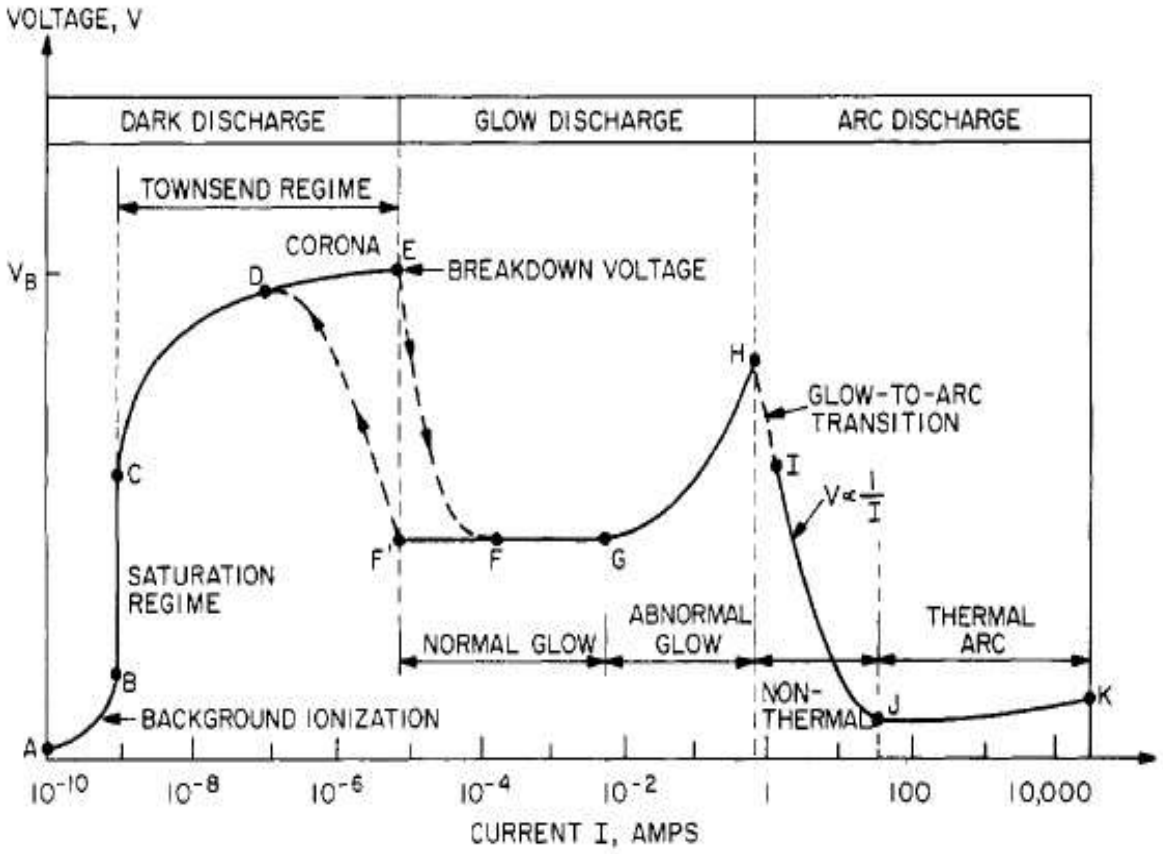


Fig. 4.1 Voltage-current characteristics of the DC low pressure electrical discharge tube[1)].

## 4.2 Discharge chamber and discharge conditions

A DC glow discharge device of 60 cm in diameter and 50 cm in length was used to produce the plasma as shown in Fig. 4.2. This device was specifically designed for carrying out metal nitridation processes, so that a pulsed plasma is mainly produced in nitrogen gas although other gases such as argon, hydrogen and methane were also available.

A negative high voltage (-1 to -2 kV) is applied, typically in 10 Pa nitrogen, at a pulse repetition frequency $f_d$ (= 0.4 - 25 kHz) to a cathode C (13 cm diameter) with five sets of grounded anode A (30 cm × 30 cm). The grounded anode centers are located at the positions $x$ = -15 cm, $x$ = 15 cm, $y$ = 15 cm, $y$ = -17 cm, and $z$ = -15 cm. The CP of 1.6 cm in diameter was set at the center ($x = y = z = 0$) of the chamber, 5 cm above the cathode ($y$ = -5 cm). The duty cycle ratio [DR = (discharge ON time) / (discharge pulse period)] can be varied in a wide range of 10-50 %. The CP used in the experiment was coated with alumina ($Al_2O_3$) so that the probe is electrically insulated, resistant to corrosion and arc ignition that can occur during discharge. Agilent NWA 8714ET (300 kHz -3 MHz) was used for CP measurements. CP measures electron density based on resonance frequency shift between discharge ON and OFF. The resonance frequency at discharge OFF was measured and found to be 838MHz.

## 4.3 Electron density measurement in pulsed discharge

A discharge was produced at a pulse repetition frequency of 1 kHz with a DR 20%. Immediately after discharge on a bright negative glow was observed at the cathode. The frequency of NWA was digitally swept from 800 MHz to 900 MHz, the number of data point being $n$ = 801 at a sweep time $T_{swp}$ = 400 ms. A very different reflectance spectra compared to a stationary plasma was observed as shown in Fig. 4.3 (a).

In a pulsed plasma, the electron density changes with time. Since, the NWA sweep time is many times larger than the discharge pulse the complex spectra comprises of spectrum

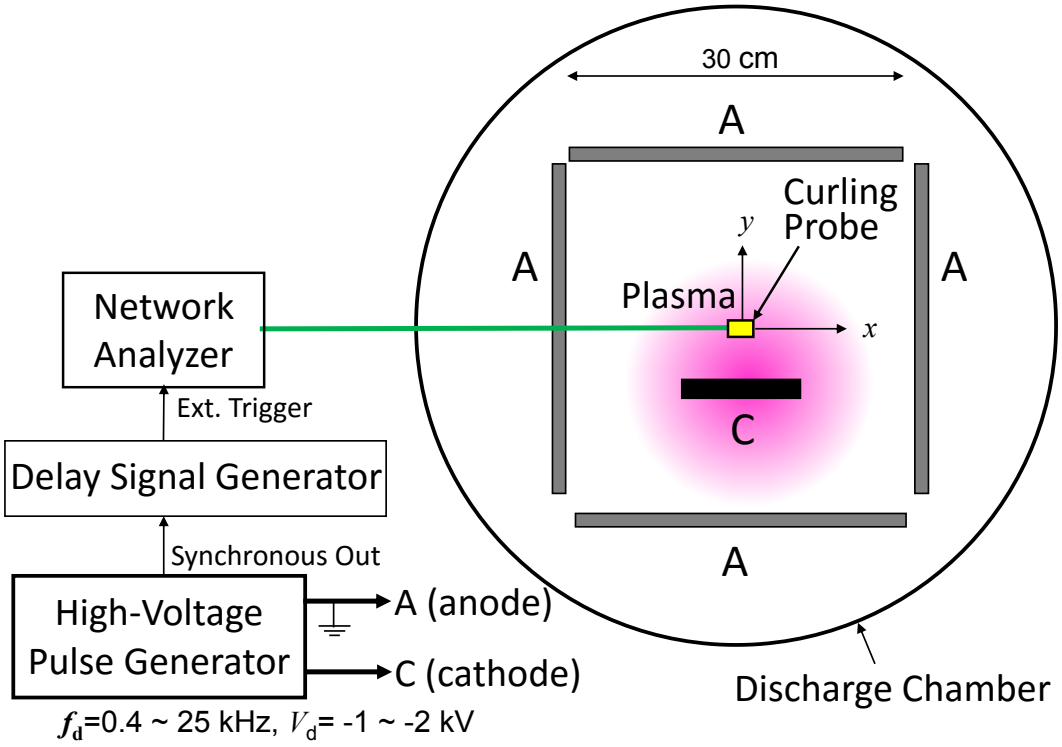


Fig. 4.2 Pulsed glow discharge apparatus

(a)

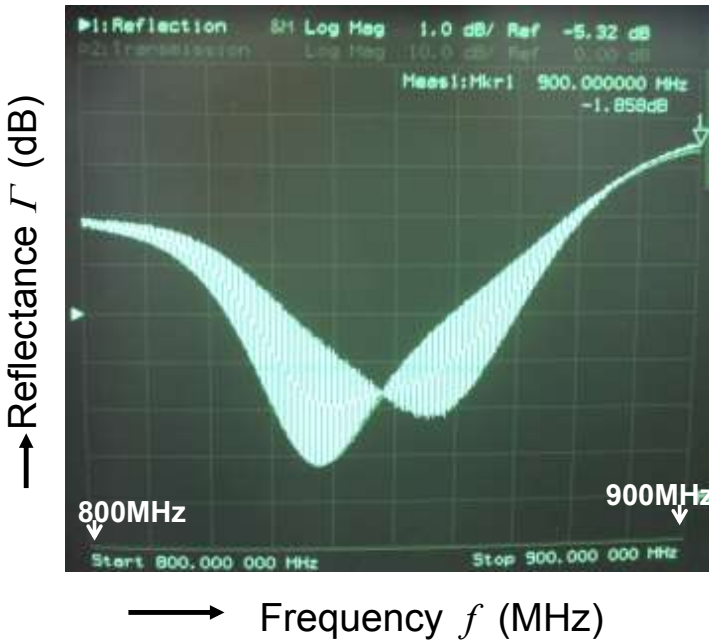


(b)

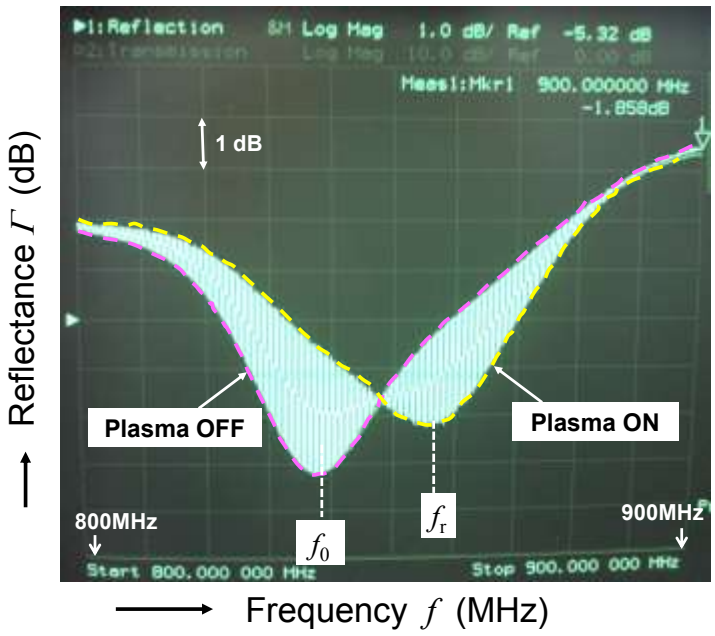


Fig. 4.3 (a) Stable frequency spectra obtained for 1kHz DR 20%, Tswp = 400 ms, (b) the complex spectra can be seen as composed of resonance frequency of plasma OFF and plasma ON condition.

corresponding to several ON and OFF states. The complex spectra is actually envelopes of frequency spectra during "Discharge ON" and "Discharge OFF" states. For ease of understanding Fig. 4.3 (a) is re-illustrated in Fig. 4.3 (b), where the pink dashed line coincides with the resonance frequency in vacuum and the yellow dashed line represents the envelope of resonance frequency in discharge ON states.

In order to understand the frequency spectra observed in Fig. 4.3, let us consider a simplified case where the normalized electron density is constant to be $N_e$=1 during the discharge ON ($T_{ON}$) and $N_e$=0 during the discharge OFF ($T_{OFF}$), as shown in Fig. 4.4. Let us also assume that NWA is set such that the number of data point $n$ = 201 with the sweep time $T_{swp}$. Hence, a single data point is obtained in a time $\Delta t = T_{swp}/200$. In Fig. 4.4 (a) the horizontal axis $\tau$ denotes the time normalized by $\Delta t$. Considering a duty ratio of 60 %, let us assign 4 points and 6 points to $T_{OFF}$ and $T_{ON}$, respectively, which means the data point per pulse period $m$ = 10 with 20 pulse periods per single frequency sweep.

In case of stationary plasma, the reflectance Γ(f) of CP measured by NWA can be expressed as

$$\Gamma(f) = 1 - A\exp[-(f - f_r)^2 / B] \qquad (4.1)$$

where $f_r$ is the resonance frequency, and $A$ and $B$ are constants. When the frequency is swept from the start frequency $f_{STRT}$ to the stop frequency $f_{STP}$ with the specified data point $n$, the frequency is digitally changed by the step $\Delta f = (f_{STP} - f_{STRT})/(n-1)$. Thus, Eq. (4.1) can be rewritten using the normalized frequency $\xi = (f - f_{STRT})/\Delta f$ as

$$\Gamma(\xi) = 1 - A\exp[-(\xi - \xi_r)^2 / B] \qquad (4.2)$$

For example, if we set the parameters $A$ = 0.5, $B$ = 1, and $\xi_r$ = 66 for plasma OFF, and $A$ = 0.3, $B$ = 1, and $\xi_r$ = 120 for plasma ON, the red and blue dashed curves in Fig. 4.5 (b) are obtained. Here the normalized frequency is swept from $\xi$ = 0 to 200. The values of $\xi$ = 0 and 200 in Fig. 4.4 (b) coincide with $\tau$ = 0 and 200 in Fig. 4.4(a) respectively.

In case of a pulsed plasma illustrated in Fig. 4.4 (a) Eq. (4.2) gives the reflectance $\Gamma(\xi)$ as indicated by the black solid line in Fig. 4.4 (b) (indicating Plasma ON). Namely, as the time goes on, the first four data points ($i$ = 1-4) show the $\Gamma$ value for plasma-OFF, and the subsequent data points ($i$ = 5-10) display the $\Gamma$ values for plasma-ON, thereafter repeating this sequence. The horizontal axes in Fig. 4.4 (a) and 4.4 (b) are on the same time scale. As a result, the NWA alternately observes the plasma-ON phase ($N_e$ = 1) and the plasma-OFF phase ($N_e$ = 0). Therefore, the envelope of the data points for the plasma-OFF phase coincides with the red dashed curve, while the envelope for the plasma-OFF phase coincides with the blue dashed curve for the stationary plasma of $N_e$ = 1. Thus, the simplified case illustrated in Fig. 4.4 clearly supports the experimental observations indicated in Fig. 4.3. It should be noted that the pulse duty ratio, the data number, and the number of data point are different in the simplified model compared to the experimental conditions.

When measurement is performed in the pulse modulated plasma, it is necessary to synchronize the pulse period $T = (T_{ON}+T_{OFF})$ with the sweep time $T_{SWP}$ for the selected $n$ number of data points. The synchronization takes place when the ratio of $T$ to $\Delta t$ is an integer. As the sweep time $\Delta t$ per data point is $T_{swp}/(n\text{-}1)$, this synchronizing condition can be rewritten as

$$(n-1)\frac{T}{T_{SWP}} = m \qquad (4.3)$$

where the data point per pulse $m$ is integer (1, 2, $\cdots$).

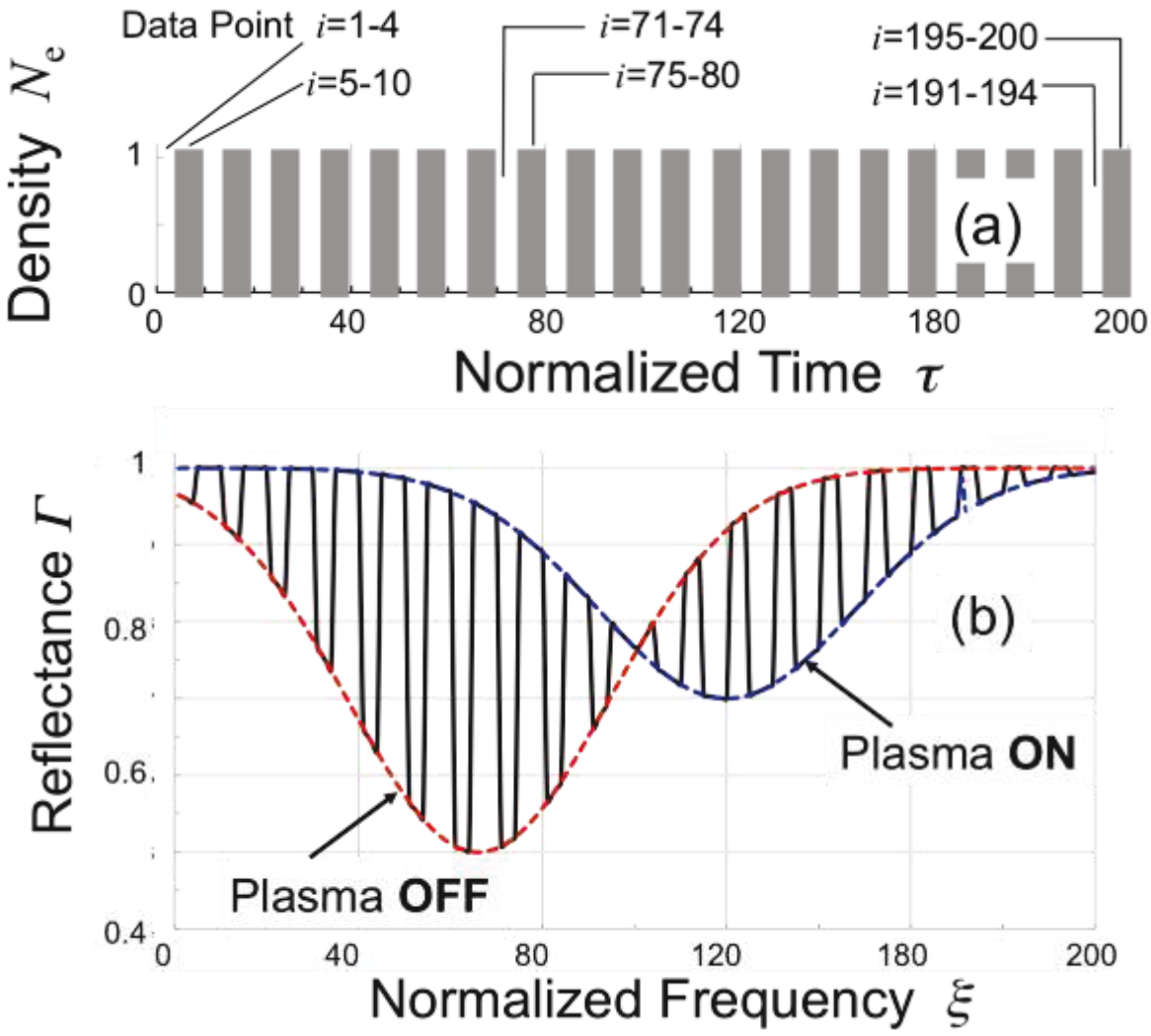


Fig. 4.4 (a) Time varying electron density Ne and (b) Complex spectra obtained for plasma ON and OFF for n = 201 and m = 10.

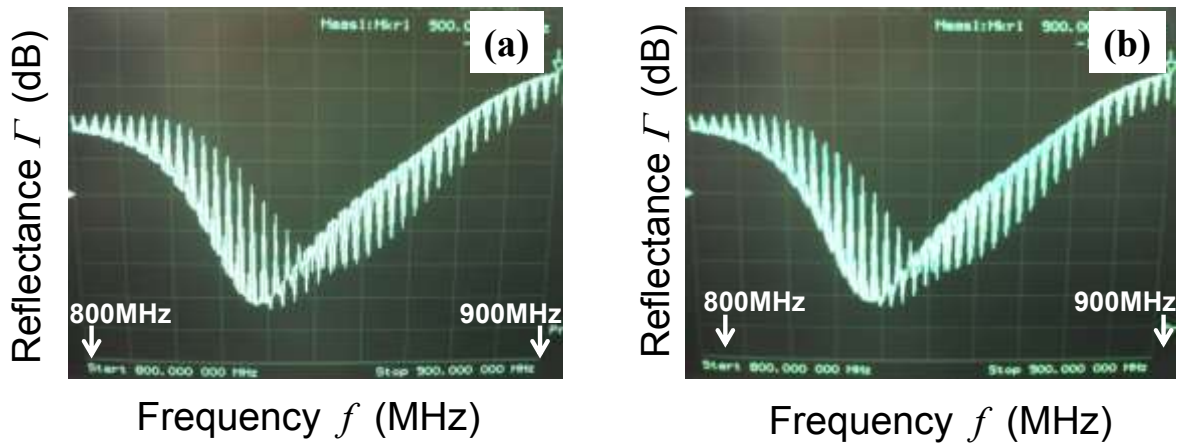


Fig. 4.5 (a) Unstable spectra observed for 1 kHz, Tswp = 380 ms with m = 1.9, and (b) Unstable spectra observed for Tswp = 420 ms with m = 2.1

In the experiment of pulsed discharge at 1 kHz ($T$ = 1 ms), the selected data number $n$ = 801 leads to various values of $m$ from Eq. (4.3), depending on the sweep time. When $T_{SWP}$ = 400 ms, one obtains the integer $m$ = 2 and observes a stable condensed spectrum owing to a good synchronization, as seen in Fig. 4.3. However, the frequency spectra are scattered and unstable sweep by sweep, for $T_{swp}$ = 380 ms ($m$ = 2.1) and 420 ms ($m$ = 1.9) because the synchronizing condition is not fulfilled as shown in Fig. 4.5.

Even in the synchronized condition ($m = 2$ and $T = 1$ *ms*), various frequency spectra were observed as shown in Fig. 4.6. It is because the NWA frequency sweep was performed independently of the discharge pulse. However, unlike Fig. 4.5, $f_0$ and $f_r$ can be easily obtained from Fig. 4.6 from the envelope lines for plasma-off and plasma-on respectively. In Fig. 4.6, using Eq. (2.15) the electron densities at different instances are calculated as are (a) $n_e$ = $0.48\times10^9$ cm$^{-3}$, (b) $1.17\times10^9$ cm$^{-3}$, (c) $1.50\times10^9$ cm$^{-3}$, and (d) $1.98\times10^9$ cm$^{-3}$ as labeled in each Fig 4.6 (a) to (d).

However, in a real case pulsed discharge the electron density $n_e$ is a function of time. In other words, unlike a stepped electron density change in the simplified model, the electron density in a real pulsed discharge smoothly changes with time as indicated in Fig. 4.7. As shown in Fig. 4.7 (a) the electron density $n_e(t)$ smoothly changes in time with the discharge ON at $t$ = 0 and OFF at $t = T$. On the other hand, the NWA digitally sweeps the frequency $f$ and samples the reflectance signal with an interval of $T/m$ as shown in Fig. 4.7 (b). The data acquisition time is approximately given by a reciprocal of the system IF bandwidth (BW) of NWA. The present model gives the BW of 30 kHz so that the time resolution is ~33 μs. For instance, the first sampling pulse ($j$ = 1) detects the reflectance of the start frequency $f_{STRT}$ at

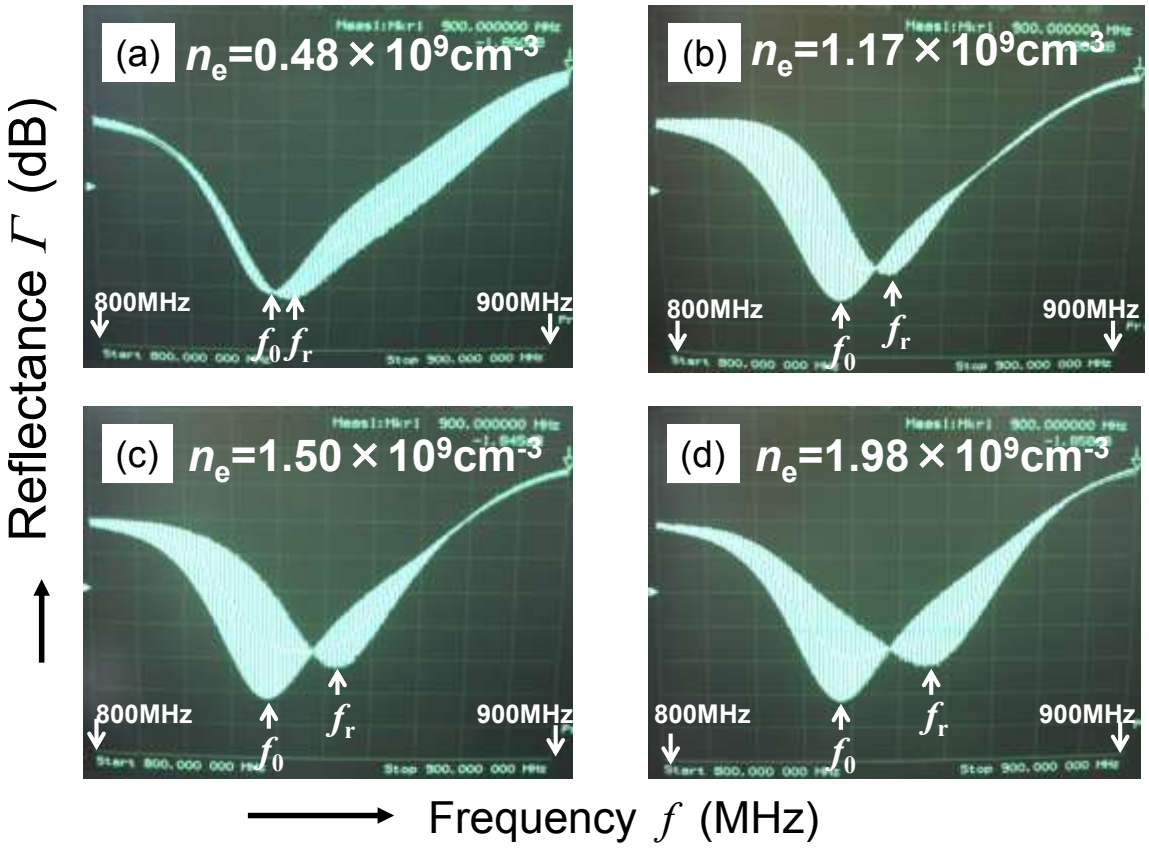


Fig. 4.6 a) Various frequency spectra observed in 1 kHz DR 20%, Tswp = 420 ms with m = 2.

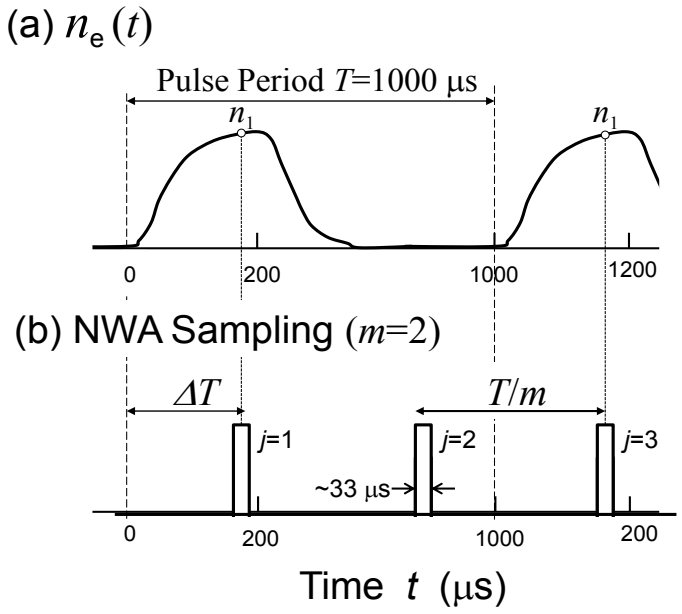


Fig. 4.7 (a) Pulse modulated electron density, (b) sampling pulse of the NWA at m = 2.

$t = \Delta T$ after the discharge ON, where the electron density is $n_1$. In case of $m = 2$, the third sampling pulse ($j = 3$) detects the reflectance of ($f_{STRT}+2\Delta f$) at the same density $n_1$. Thus, the first sampling time $\Delta T$ specifies the timing of $n_e(t)$ measured by the NWA.

Essentially, $\Delta T$ corresponds to the phase difference between the discharge pulse chain and the sampling pulse chain of NWA under the synchronized condition. In the present measurement, however, the NWA sweeps the frequency irrespective of discharge pulse so that $\Delta T$ is different per sweep. This is the reason why various frequency spectra were observed as in Fig. 4.6. To measure $n_1$, $\Delta T$ can be externally delayed against the discharge pulse. For the NWA used in the experiments, this feature of external trigger delaying was not available making time-resolved measurement impossible.

## 4.4 Summary

In this chapter, CP system using a conventional NWA was applied to the measurement of time-modulated electron density in plasma. In the pulse-modulated plasma measurement, it is necessary to synchronize the sweep time $T_{swp}$ of NWA with the pulse modulation period $T$, $(n\text{-}1)T/T_{SWP}$= integer (1, 2, ···) for the data point number $n$. Under the synchronized condition, a fully time-resolved measurement of the electron density can be made only when the first sampling time of the NWA is delayed relative to the timing of the discharge pulse by triggering the frequency sweep externally. Even though such control of the first sampling time was not available, the highest electron density within the pulse can be calculated by making several frequency sweeps and finding the maximum shift of resonance frequency.

References

1) J. R. Roth, *Industrial Plasma Engineering* Vol. I (IOP Publishing, London, 1994), 1st ed., p.149

2) M.A. Lieberman and A.J. Lichtenberg, *Principles of Plasma Discharges and Materials Processing* (Wiley, New York, 2005) 2nd ed., p.539

3) D. Pye, *Practical Nitriding and Ferritic Nitrocarburizing* (ASM International, Ohio, 2003) 1st ed., p.75

# Chapter 5

# On-point Mode of CP Measurement in Pulsed Discharge

## 5.1 Introduction

Due to the various applications of pulsed plasma, measuring time evolution of electron density is very important. In Chapter 4, measurement of electron density using a conventional NWA by fulfilling the synchronization condition was discussed. However, time-resolved measurement was not possible because the NWA couldn't be externally triggered. So, a newer NWA, Agilent E5071C was used to perform electron density measurement in pulsed plasma.

## 5.2 Experimental procedure

The experiments were performed on the same chamber as in Fig. 4.2. NWA Agilent E5071C operated in external trigger mode was used to perform all the experiments. A synchronous output from the high voltage power source was connected to the external trigger port of NWA using a Baby N Connector (BNC) cable. To nullify the effects caused by cable and connector loss, *one-point* calibration was performed before the start of each experiment. CP derives electron density based on resonance frequency shift obtained through frequency sweep of NWA. In the case of pulse modulated plasma, the electron density changes in time which causes temporal variations of reflectance spectrum and resonance frequency during the frequency sweep. In order to measure a frequency spectrum of reflectance $\Gamma$ ($S_{11}$ parameter) at a constant *phase* (*electron density*) of modulated electron density, two data sampling modes

of NWA were available; *on sweep* mode and *on point* mode. Experiments were performed by using *on sweep* mode in the beginning.

## 5.3 Reflectance measured with *on sweep* mode

A simplified data acquisition technique for *on sweep* mode is shown in Fig. 5.1. The frequency of NWA is digitally swept triggered by a synchronous out of the high-voltage pulse generator with the discharge pulse period $T$. When a discharge power $P_d$ is turned on and off, the electron density $n_e$ repeatedly varies in time as illustrated in the top section of Fig. 5.1.

Let the total number of data point be $n$ with the frequency sweep period $T_{SWP}$ of NWA. In the *on sweep* mode, a single discharge trigger drives $n$ numbers of frequency $f$ and the resultant reflectance $\Gamma$ during $T_{SWP}$, is as shown in lower section Fig. 5.1. Thus, the data point $m$ per single cycle of the discharge pulse is given by Eq. (4.3).

As mentioned in Chapter 4, in order to get stable reflection spectrum, the parameters $n$, $T$, and $T_{SWP}$ should be adjusted for $m$ to be integer. This is the *synchronization* condition[1)] in *on sweep* mode of measurement. A complex reflectance spectrum is obtained under synchronization using *on sweep* mode owing to a mixing of $\Gamma$ at different times. A well-defined algorism of data analysis is needed for deduction of time- resolved reflectance spectrum from the mixed frequency spectra.

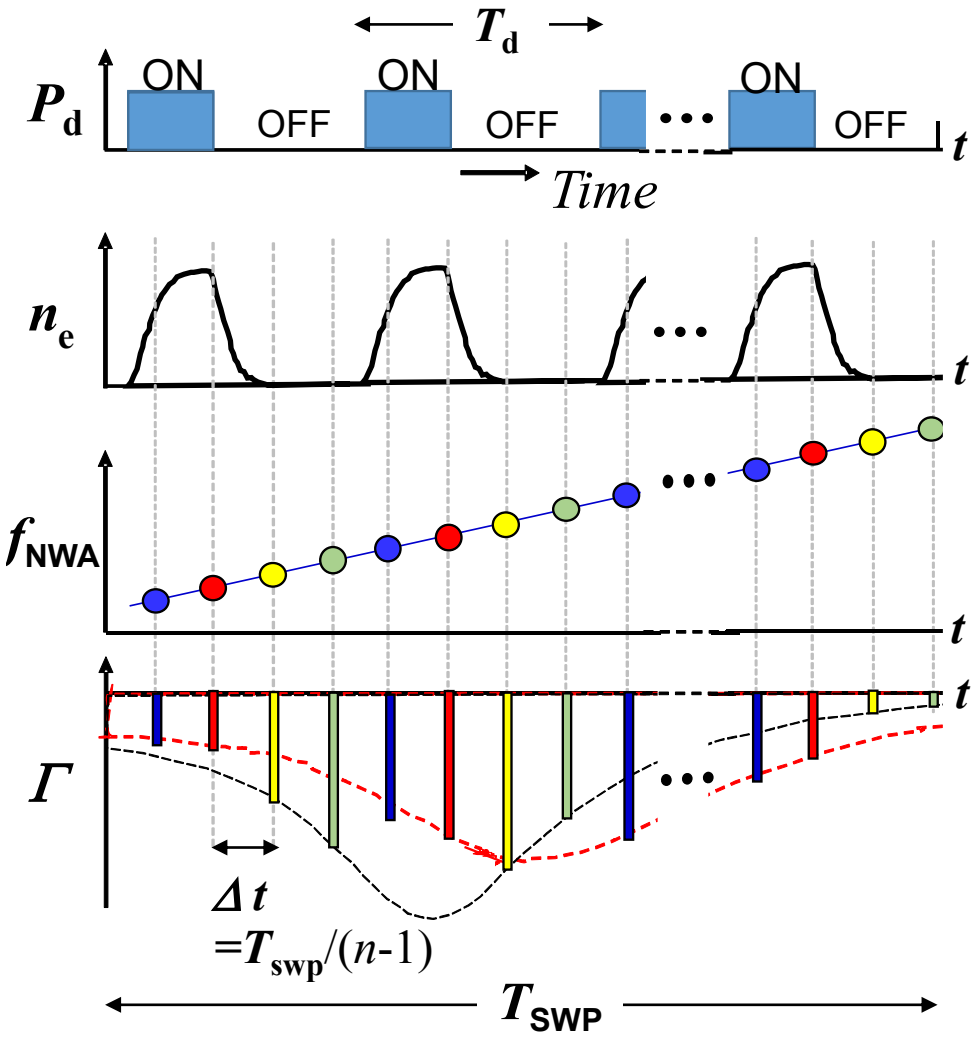


Fig. 5.1 Data acquisition in *on sweep* mode.

## 5.4 Time resolved measurement by *on sweep* mode

Fig. 5.2 (a) shows the reflectance spectra obtained for 0.4 kHz discharge at 13% DR by fulfilling the synchronization condition indicated in Eq. (4.3).

The sweep time ($T_{SWP}$) was 25 ms and the number of data points was $n$ = 1601 and $m$ = 10. Therefore, the complex spectra corresponds to 10 data points representing different phase in the pulse at intervals of $T/m$ (0.25 ms). The 1601 data points was divided into 10 groups ($m$=1 – 10), such that the first $m$=1group contains the data number 1, 11, 21… 1601, the second $m$=2 group contains the data number 2, 12, 22….1592 and so on.

The group of $m$ = 1-10 forms the reflectance $\Gamma$ spectrum corresponding to its phase, i.e., the time $\tau$ after turn-on of the discharge. Three examples of time-resolved $\Gamma$ spectrum corresponding to the discharge time $\tau$ = 0.25 ms, 0.5 ms and 0.75 ms are shown in Fig. 5.2 (b). The resonance frequencies found in these spectra, can be used to calculate the temporal electron density in Eq. (2.15). By sufficiently delaying the trigger time, a time resolved reflectance ($S_{11}$) at various time $\tau$ after the ignition of discharge is obtained. The resonance frequencies thus obtained can be used to measure the time evolution of electron density as shown in Fig. 5.2 (c).

The trigger polarity was initially chosen as negative edge, i.e, the trigger is activated when the trigger signal makes transition from high to low. It was found that sweep triggering in negative edge required sufficient delay of NWA to obtain a complete spectrum of electron density (drop to rise in the next cycle). So, all the subsequent experiments were performed in positive trigger edge.

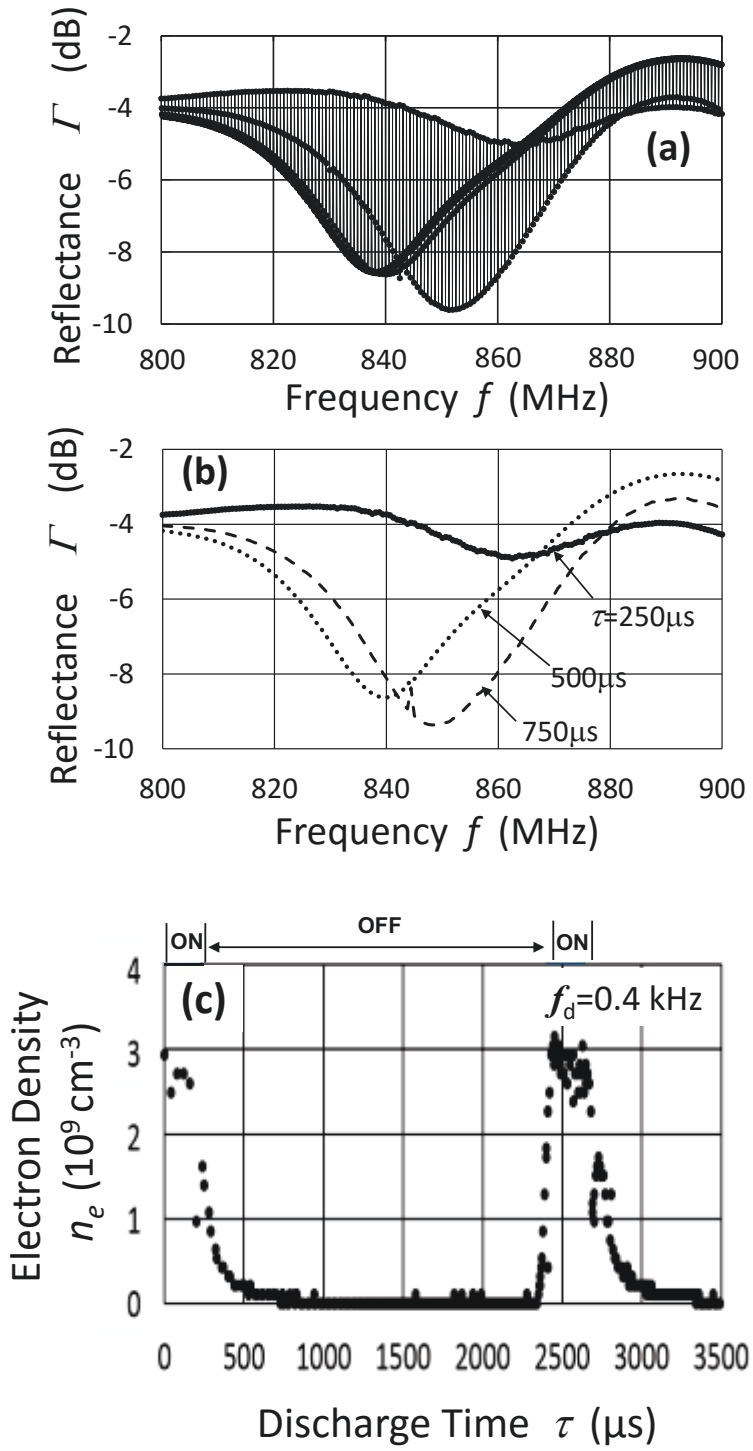


Fig. 5.2 (a) Reflectance spectrum obtained for 0.4 KHz at 13% DR, (b) Time-resolved $\Gamma$ spectrum corresponding to $\tau$ = 250μs, 500 μs and 750 μs, and (c) Time-resolved electron density measured for 0.4 KHz at 13% DR.

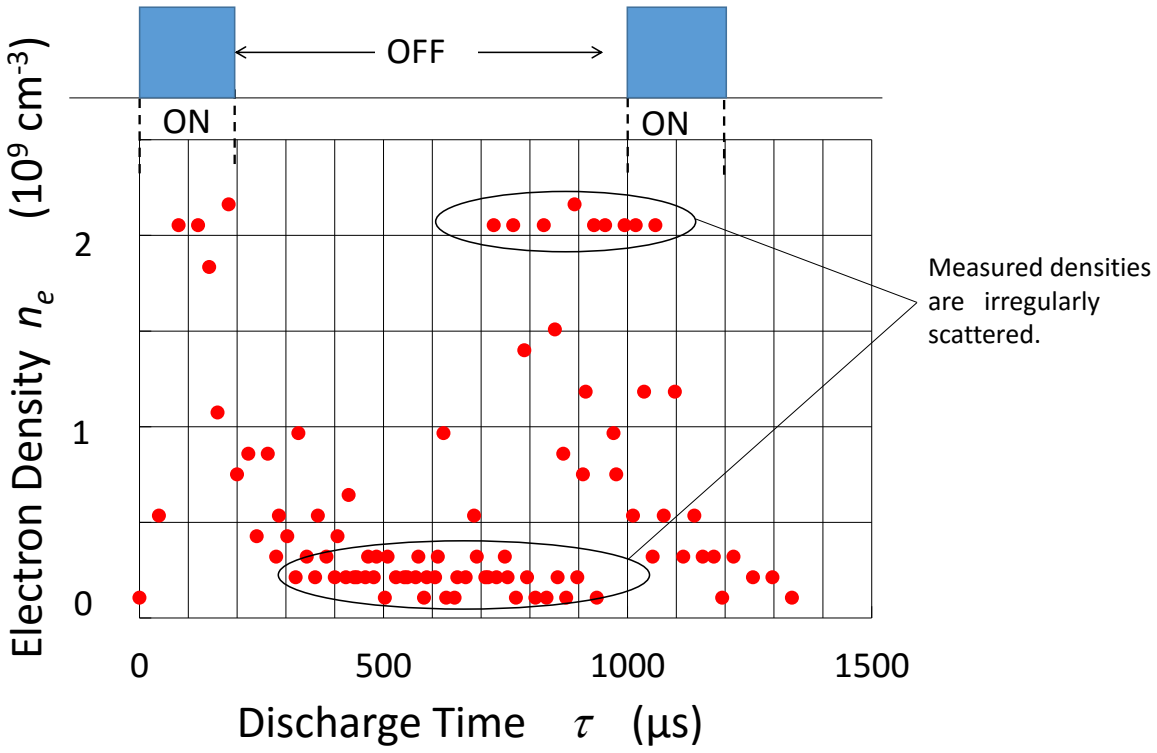


Fig. 5.3 Data scattering observed at 1 kHz DR 20% using *on sweep* mode.

Temporal variation of electron density at the discharge pulse frequency lower than 0.5 kHz were successfully measured in 10 Pa $N_2$ gas using *on sweep* mode. However, the reflectance spectrum obtained for high frequency pulsed discharge was found to be irregular and the time-resolved electron density was scattered. This scattering was found to increase with pulse frequency and increasing duty cycle ratio. Fig. 5.3 shows the time-resolved electron density measured for 1 kHz DR 20% using *on sweep* mode. It is evident from the figure that there is some error with the measurement.

At low frequency pulse, the NWA sweeps the frequency in full span per trigger received. However, as the pulse frequency increases, the NWA cannot make a full span sweep but needs intermittences among divided ranges of frequency sweep, causing the timing error in data acquisition by *on sweep* mode. Also, data analysis in *on sweep* mode is time-consuming and tedious. So, a different synchronization method called *on point* mode was used.

## 5.5 Reflectance measured with *on point* mode

In *on point* mode, each discharge trigger drives a single frequency $f_{NWA}$ (only one data point) per discharge pulse, and the reflectance is measured at the constant *phase* (constant *electron density*) of the discharge pulse, as shown in Fig. 5.4. In other words, the discharge pulse period $T_d$ is equal to the data sampling period $\Delta t = T_{SWP}/(n\text{-}1)$, and substituting this relation into Eq. (2.15) leads to $m = 1$. Thus, the *on point* mode automatically satisfies the synchronization condition. A single frequency sweep of NWA yields $n$ numbers of different frequency $f$ at the same electron density (indicated in the middle of Fig. 5.5). As a result, the reflectance spectrum at the observing *phase* (*electron density*) is immediately obtained as shown in the bottom of Fig. 5.4, without post-analysis of data required in the *on sweep* mode. This is one of the merits of *on point* mode, another being it's applicability to higher pulse repetition frequency with better time resolution.

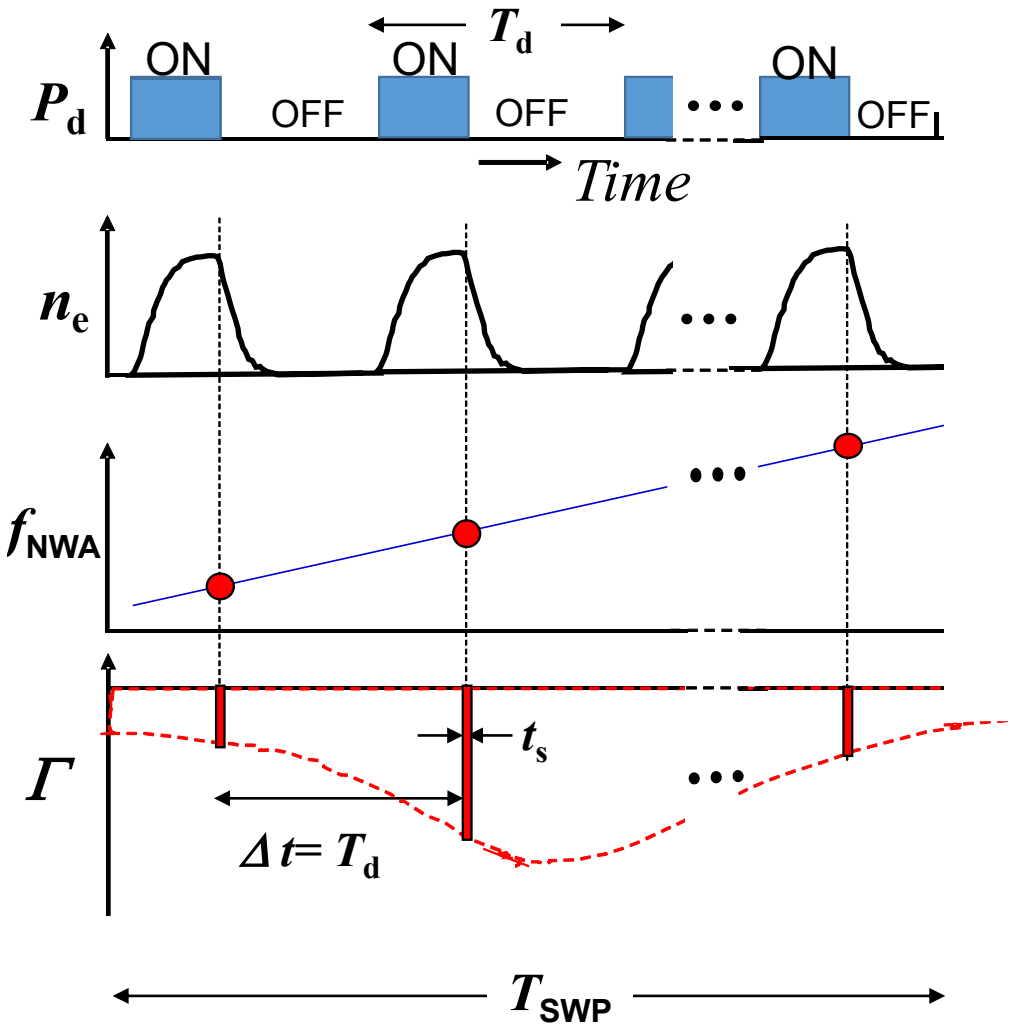


Fig. 5.4 Data acquisition in *on point* mode.

Since *on point* mode gives only one data of the electron density at the triggered time, one needs to delay the NWA trigger time in the discharge pulse period, in order to obtain a full shape of temporal electron density change. A pitch $\Delta t_D$ of time delay is desired to be as small as possible to increase the number of measured points during one cycle of the pulse.

## 5.6 Time-resolution of measurement

NWA uses super heterodyning detection system, i.e., the incoming signal is mixed with a local oscillator signal to obtain an intermediate frequency (IF) which is then passed through a band pass filter (IFBF). The IFBF acts as a window to detect the signals, and hence the time resolution of measurement is approximately given by a reciprocal relation with resonance bandwidth (RBW) of IF filter. For instance, for RBW of 100 kHz, the sampling time $t_s$ per data point is ~10 μs. If the pulse discharge period $T_d$ is shorter than the sampling time $t_s$, then there will be instances where IF measurement will have no pulse at all, leading to poor trace noise. Therefore, measurements should be made such that $t_s < T_d$.[2)] In the present study, we chose an RBW of 70 kHz in Agilent E5071C which corresponds to $t_s$ ~14 μs.

## 5.7 Time-resolved electron density measured with *on point* mode

Temporally changing electron density was measured in *on point* mode of NWA E5071C at the pulsed discharge frequencies higher than 1 kHz. Fig. 5.5 (a) shows three reflectance curves obtained at $\tau = 0$, 10 μs, and 20 μs for a 1 kHz discharge with DR 30%. It should be noted that the reflectance curves obtained are exactly similar to that of steady-state plasma greatly simplifying the data analysis. Fig. 5.5 (b) and 5.6 (c) display the discharge voltage, electron density and current respectively.

It is seen in this figure that the electron density increases and saturates following the trend of discharge current till $\tau = T_{ON}$. After the discharge off ($\tau > T_{ON}$), the current sharply decreases

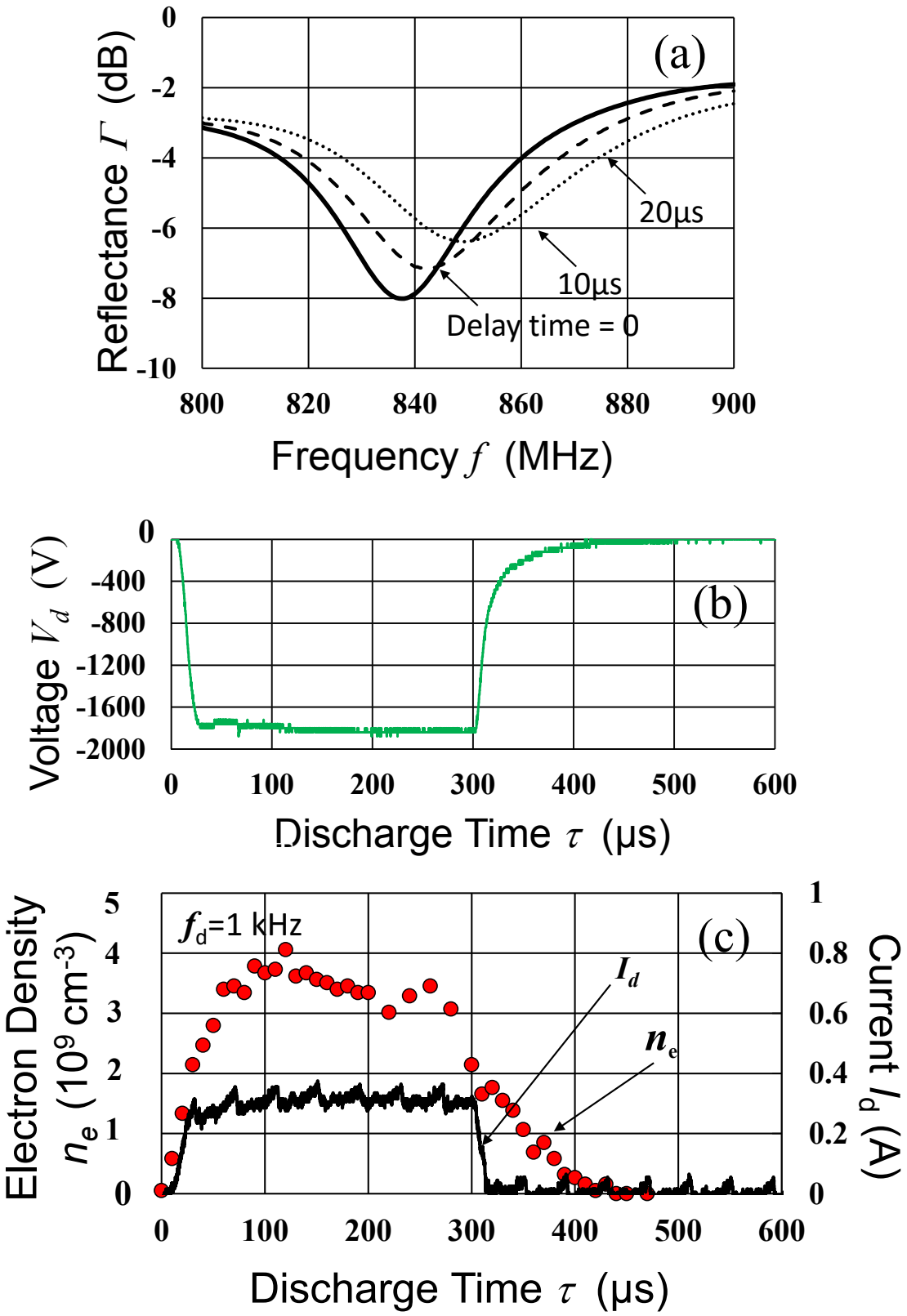


Fig. 5.5 (a) Reflectance obtained using *on point* mode for 1 kHz D.R 30% at $\tau$ = 0, 10 μs, and 20 μs, (b) discharge voltage for 1 kHz DR 30%, and (c) discharge current and time variation of electron density.

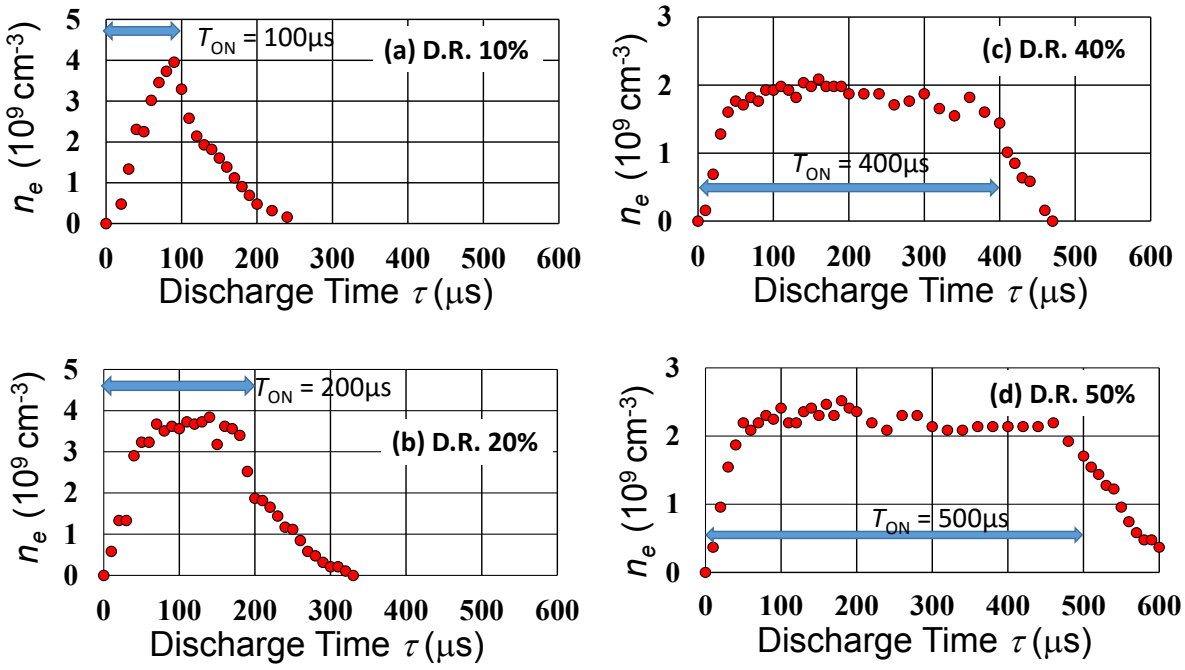


Fig. 5.6 Time evolution of electron density 1 kHz DR (a) 10%, (b) 20%, (c) 40% and (d)50%

to zero but the electron density decreases much slowly with a time scale of 100 μs in afterglow regime. Experiments were also performed by changing the duty cycle ratios (DR) to observe the dependence on time-variation of electron density for 1 kHz discharge. Fig. 5.6 shows the results of electron density measured in *on point* mode at pulse frequency of 1 kHz at the DR of 10%, 20%, 40% and 50%. The electron density in the active glow regime was found to decrease with increasing DR. This is because with the increase in DR, the peak discharge current decreases with increasing $T_{ON}$.

To observe the frequency dependence of electron density, experiments were performed at high repetition frequencies (>1 kHz). Fig. 5.7 shows the electron density profile obtained for 5 kHz with DR 50%. It can be seen in Fig. 5.7 that at *discharge on* the electron density increases up to a certain value and then drops to zero value in the discharge off region. This trend repeats again and again throughout the pulse.

For NWA E5071C, the minimum trigger delay time is 10 μs. For instance, at pulse frequency of 10 kHz with 20% DR, the discharge on time $T_{ON}$ is only 20 μs which allows data acquisition of only 2 points for $\tau < T_{ON}$. To overcome this data deficit, an external signal delay device (Hewlett Packard 8116A pulse/function generator) was used to delay the trigger signal, which enables delaying the trigger signal to a minimum of 2 μs. However, the minimum time resolution of measurement is not 2 μs but 14 μs. The time-resolution of measurement depends on the IFBW of the NWA, which was explained in the previous Sec. 5.6.

NWA operated in *on point* mode in conjunction with pulse delay generator was used to make measurement to pulse discharge of 10 kHz with 50% DR. Fig. 5.8 (a) shows the discharge voltage and Fig 5.8 (b) shows the temporal electron density change.

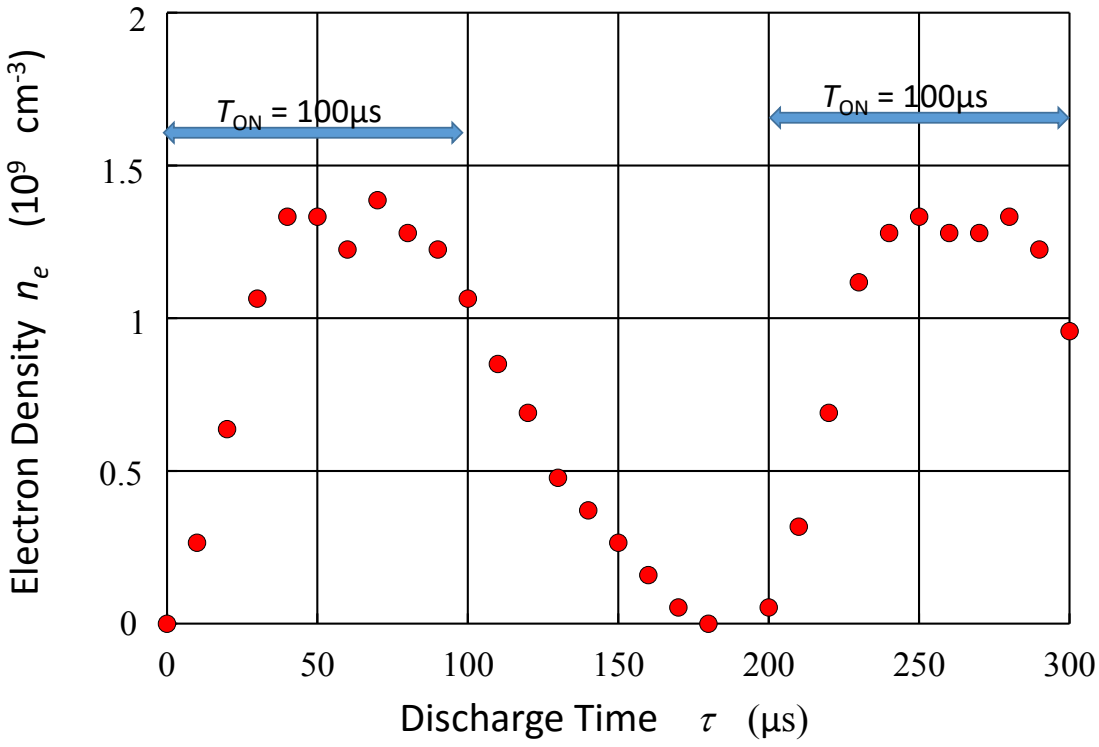


Fig. 5.7 Time evolution of electron density 5 kHz DR 50%.

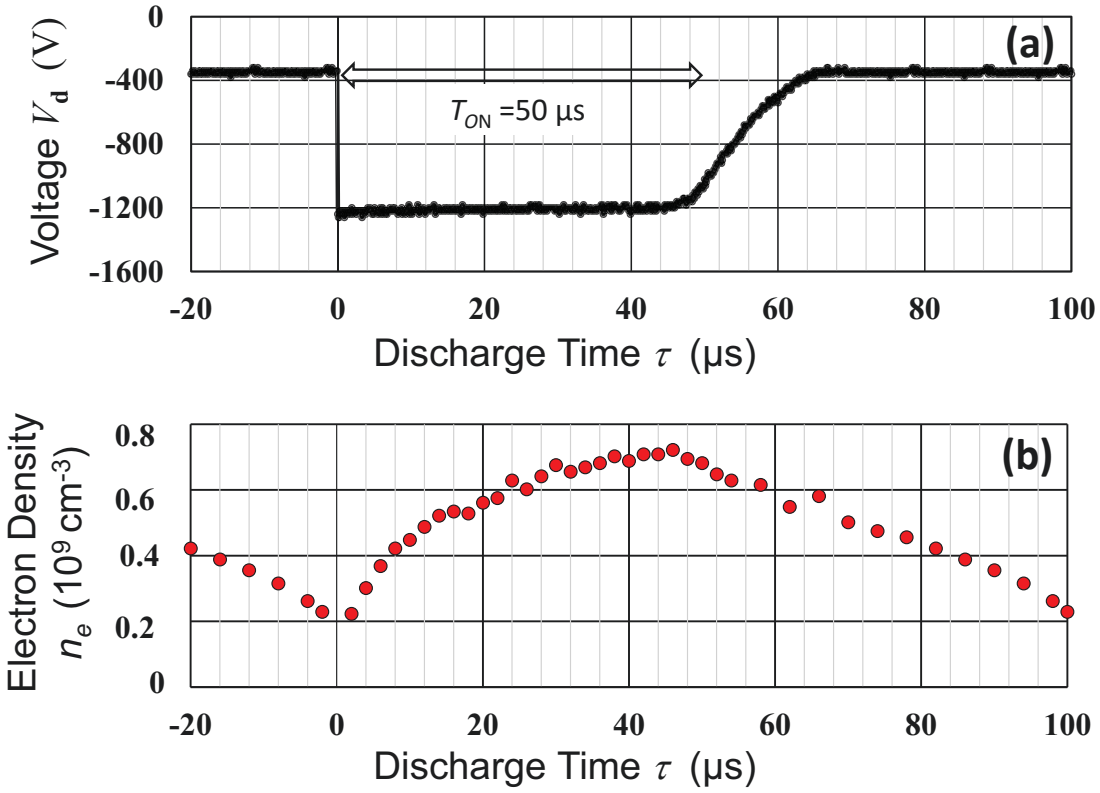


Fig. 5.8 (a) Discharge voltage for 10 kHz DR 50%, (b) Time variation of electron density.

It can be seen in Fig. 5.8 (b) that the electron density at $\tau = 0$ is not zero and the plasma continues over the discharge on and off. Namely, the plasma slowly decays and survives during the afterglow. This is clearly the effect of high pulse repetition frequency which is more visible as the repetition frequency is increased.

Fig. 5.9 (a) and (b) show the discharge voltage and electron density variation at 25 kHz DR 50%. The continuation of electron in the discharge is more evident through this figure.

Due to the limitation of the power-source used in the experiments, time-resolved electron density could be measured only up to 25 kHz. However, *on point* mode is applicable to even higher frequencies if used with newer pulsed network analyzers (PNA).

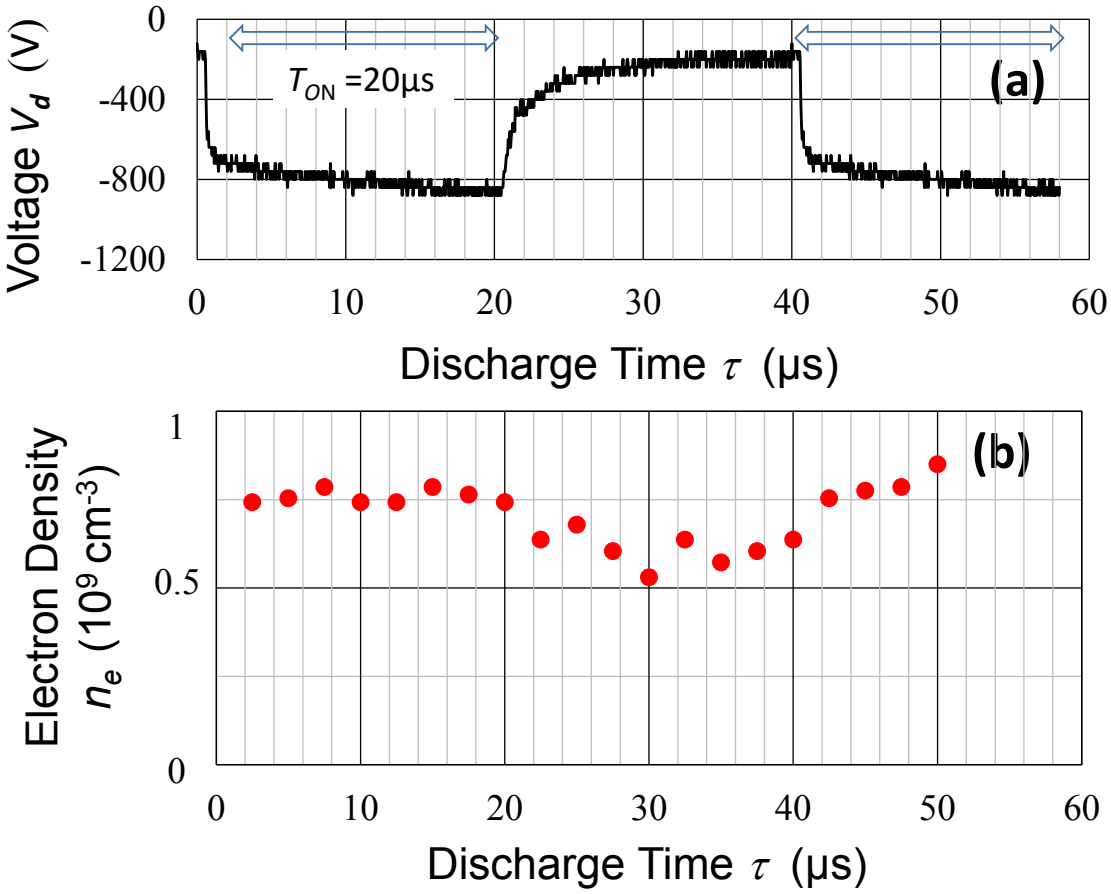


Fig. 5.9 (a) Discharge voltage (b) Electron density evolution for 25 kHz DR 50%

## 5.8 Electron density decay in afterglow region

The nature of electron density decay in the afterglow was investigated in nitrogen and argon discharge for the same pulse frequency of 1 kHz with 30% DR at a pressure of 40 Pa. Fig. 5.10 (a) and 5.10 (b) show the electron density decay in nitrogen and argon afterglow, respectively. In the case of nitrogen, an exponential density decrease was observed as shown in Fig. 5.10 (a), which can be simply expressed as exp ($-t/\tau_D$) with the time constant $\tau_D$~60 μs. On the other hand, the argon afterglow data in Fig. 5.10 (b) shows three step decrease: $\tau_D$~50 μs in step (i), $\tau_D$~400 μs in step (ii), and $\tau_D$~100 μs in step (iii).

To understand the difference of afterglow density decay between nitrogen and argon, we performed Langmuir probe measurement in a simplified condition of DC discharge at a pressure of 40 Pa where the discharge voltage and current was $V_d$ = -700 V and $I_d$ = 150 mA in nitrogen, and $V_d$ = -600 V and $I_d$ = 150 mA in argon. The Langmuir probe was a home-made probe of diameter 0.5 mm and the length of 0.8 cm. The semi-log plot of electron current $I$ and probe voltage $V$ curve for $N_2$ and Ar are shown in Fig. 5.10. The slope of straight line fitted for the measured points gives the electron temperature $T_e$~0.3 eV for the nitrogen discharge, while the argon plasma has a bi-Maxwellian type of electron energy distribution function with bulk temperature $T_{eb}$~0.9 eV and hot tail temperature $T_{eh}$~2 eV. Thus the argon plasma has abundant high-energy electrons, which are attributed to secondary electrons emitted from the cathode. The roughly three-step decay mechanism in argon afterglow can be explained based on the EEDF. In the afterglow, the high energy electrons are immediately lost in the step (i), since they can escape through a potential barrier around the cathode and anode. As the time passes by, the bulk electron temperature gradually decreases in the step (ii). When the temperature drops to ~0.2 eV, electron-neutral collision resonantly decreases owing to

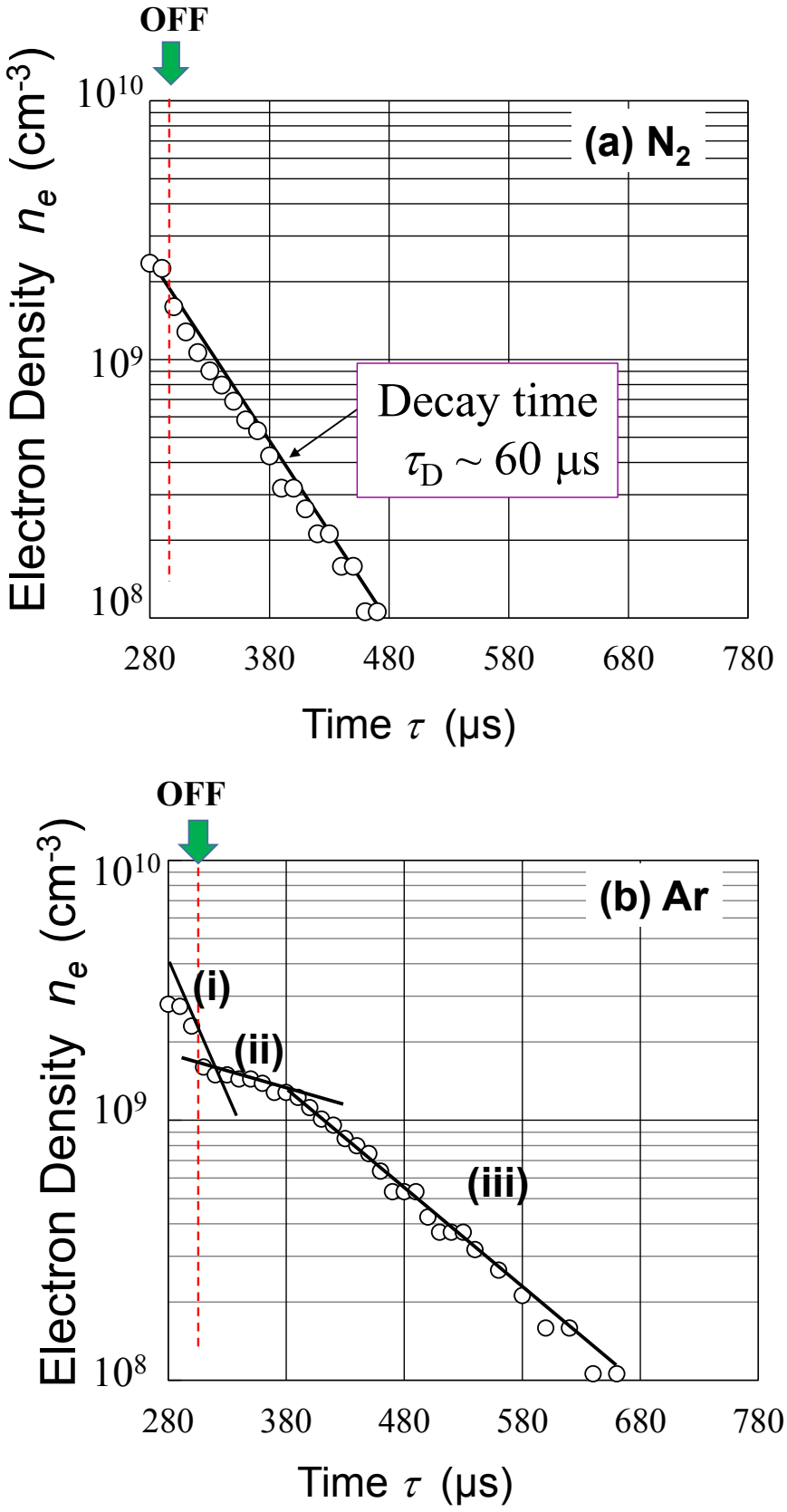


Fig. 5.10 (a) Electron density decay in $N_2$ afterglow, (b) Electron density decay in Ar afterglow

Ramsauer effect.[3] Thus, the electron diffusion loss is enhanced, leading to smaller value of $\tau_D$ in the step (iii).

On the other hand, nitrogen being a molecular gas, the high energy electrons are easily lost through many loss channels of inelastic collisions exciting to vibrational and rotational energy levels, along with dissociation processes.[4] This is the reason why high energy tail was hardly observed in nitrogen DC discharge as in Fig. 5.11. In the afterglow of pulsed discharge, a monotonic exponential decay of electron density was observed, probably due to a small Ramsauer effect in the case of nitrogen.

The electron density measured by curling probe (CP) was also compared with Langmuir probe. For the Langmuir probe used in the experiments the current acquisition area (A) was calculated to be $1.276\times10^{-5}$ m$^2$. Since the probe current collection area is large, for simplicity a planar probe model was considered.

The Langmuir probe electron saturation current is given by the equation :

$$I_{esat} = \frac{1}{4} en_o \bar{v}_e A \qquad (5.1)$$

where $e$ is charge of electron, $n_o$ is electron density at sheath edge, $m$ is the mass of electron, $K$ is the Boltzmann constant and $\bar{v}_e = \sqrt{\frac{8kT_e}{\pi m_e}}$ ,

The electron saturation current ($I_{esat}$) for $N_2$ was calculated from I, V curve to be $2.7045\times10^{-4}$ Amp. The electron density was calculated using Eq. (5.1) to be $1.446\times10^{9}$cm$^{-3}$. The electron density measured in the same plasma by CP displayed a value of $1.87\times10^{9}$cm$^{-3}$. These values lie in close proximity with each other, thus indicating a good agreement between CP and Langmuir probe measurement.

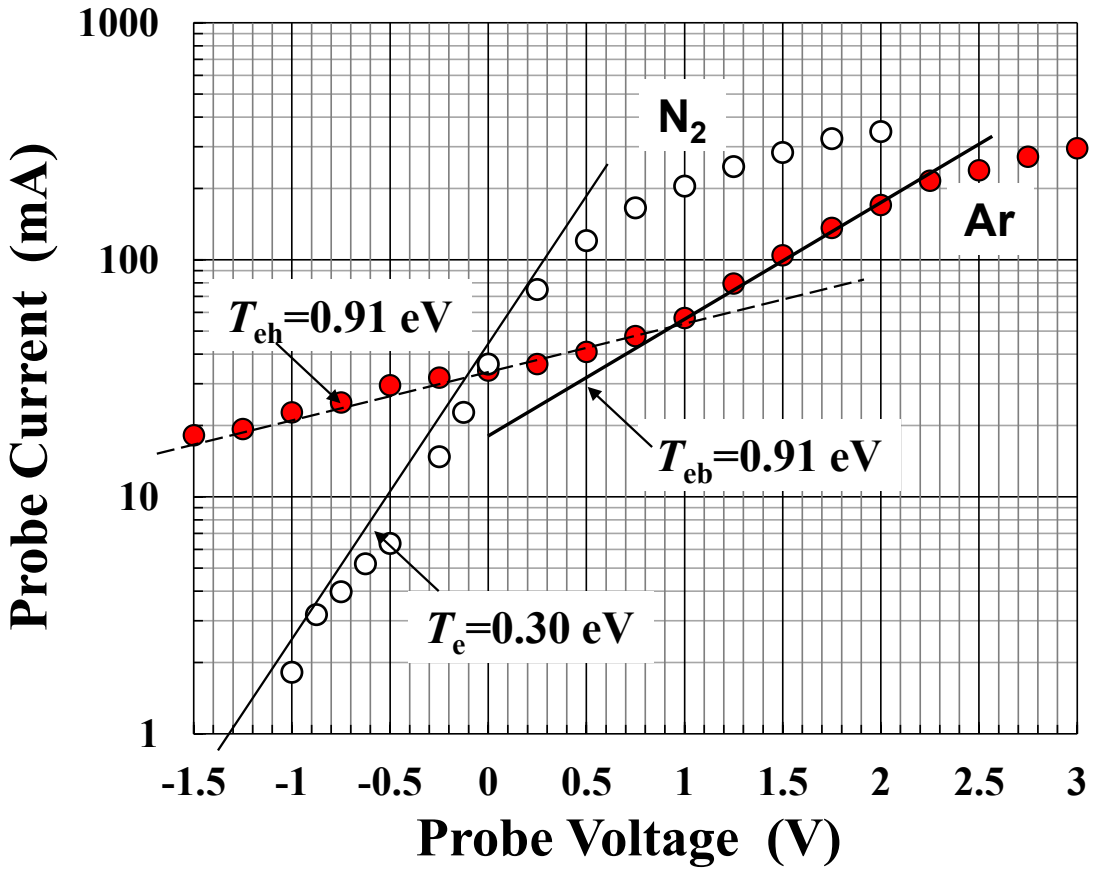


Fig. 5.11 Semi-log plot of probe electron current and probe voltage for DC discharge at 40 Pa in nitrogen and argon.

## 5.9 Summary

CP technique was applied to time-resolved measurement of electron density in pulsed DC glow plasma. Owing to the time variation of electron density (and hence resonance frequency), the NWA gives complex reflectance spectra when operated in *on sweep* mode. The complex spectra obtained by *on sweep* mode is applicable for time-resolved electron density measurement at low pulse frequency < 0.5 kHz. For higher frequencies of pulse discharge (up to 25 kHz), *on point* mode of NWA was introduced where each discharge trigger gives one data point of reflectance at a single frequency. The *on point* mode of NWA was utilized to perform time resolved electron density measurement in pulse frequencies up to 25 kHz. Using an external trigger delay, data was obtained at a minimum time interval of 2 μs in time-resolved measurement. The decay time constant of electron density in afterglow was investigated in nitrogen and compared with that of argon pulsed discharge. Three-step decay was observed in the case of argon. Langmuir Probe measurements showed a bi-maxwellian electron energy distribution for argon. The three-step decay mechanism was tentatively explained based on the bi-maxwellian distribution and on-set of Ramsauer effect.

References

1) A. Pandey, W. Sakakibara, H. Matsuoka, K. Nakamura, and H. Sugai: *Appl. Phys. Lett*. **104** (2014) 024111.

2) J.P. Dunsmore, in *Handbook of Microwave Component Measurement with Advanced VNA Technique* (Wiley, New York, 2012)1st ed., p. 365.

3) S. C. Brown, *Introduction to Electrical Discharges* (Wiley, New York, 1966) 1st ed., p. 6.

4) M.A. Lieberman and A.J. Lichtenberg, *Principles of Plasma Discharges and Materials Processing* (Wiley, New York, 2005) 2nd ed., p. 82.

# Chapter 6

# CP Measurement of Pulsed Plasma in Surface Magnetic Field

## 6.1 Introduction

Magnetic confinement has often been used to produce high density plasmas. Magnetic confinement can increase the power efficiency or number density in DC or RF glow discharges[1]. One of the plasma confinement technique is magnetic multipole confinement. In this technique, a set of alternating rows of north and south pole permanent magnets are placed around the surface of the discharge chamber[2]. The alternate rows of magnet produce *line cusp* as shown in the Fig 6.1[3]

The cusp fields formed at the chamber wall reduce the plasma diffusion loss to the wall of the chamber. Since magnetic field strength becomes weaker towards the center of the chamber, the plasma bulk is unmagnetized. Leung et al.[4,5] performed experiments using multipole fields and reported on good confinement and radial uniformity of bulk plasma.

## 6.2 Experimental apparatus

The experiments were performed in a surface magnetic confinement (SMC) device 105 cm in diameter and 120 cm in length. A pulsed plasma is produced in various gases (Ar, $CH_4$, $C_2H_2$, and $N_2$) typically at low pressure (1-3 Pa). The chamber consists of 3 cylindrical cathodes (13cm diameter, 100cm length), an 80-cm-diameter bottom disc cathode and a top ring cathode (55cm outer diameter, 30 cm inner diameter) and a grounded cylindrical anode (103cm in diameter). The number of cylindrical cathodes in the device could be increased or decreased according to the need. However, almost all the experiments were done by placing three

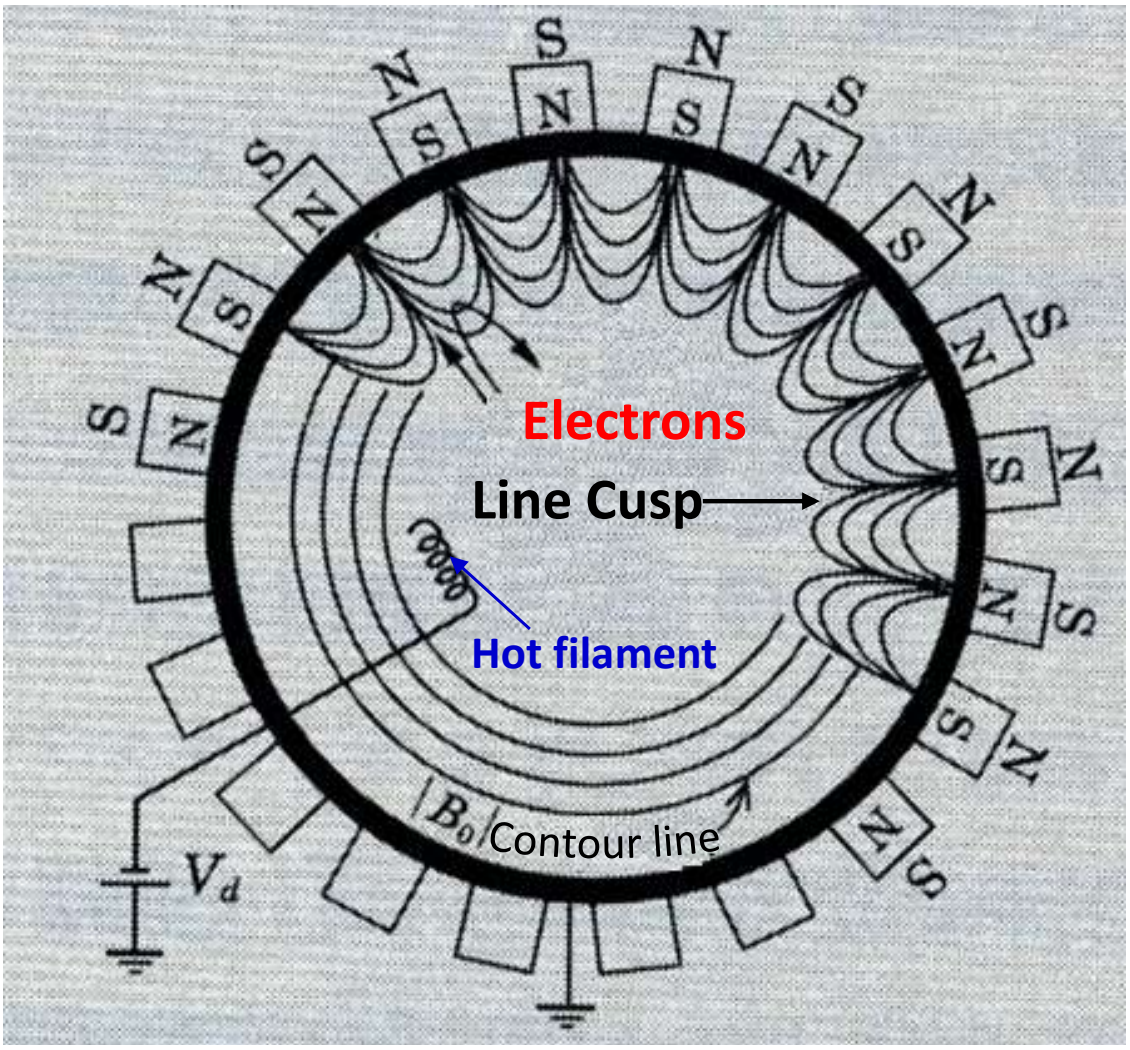


Fig. 6.1 Line cusps formed by permanent magnets.

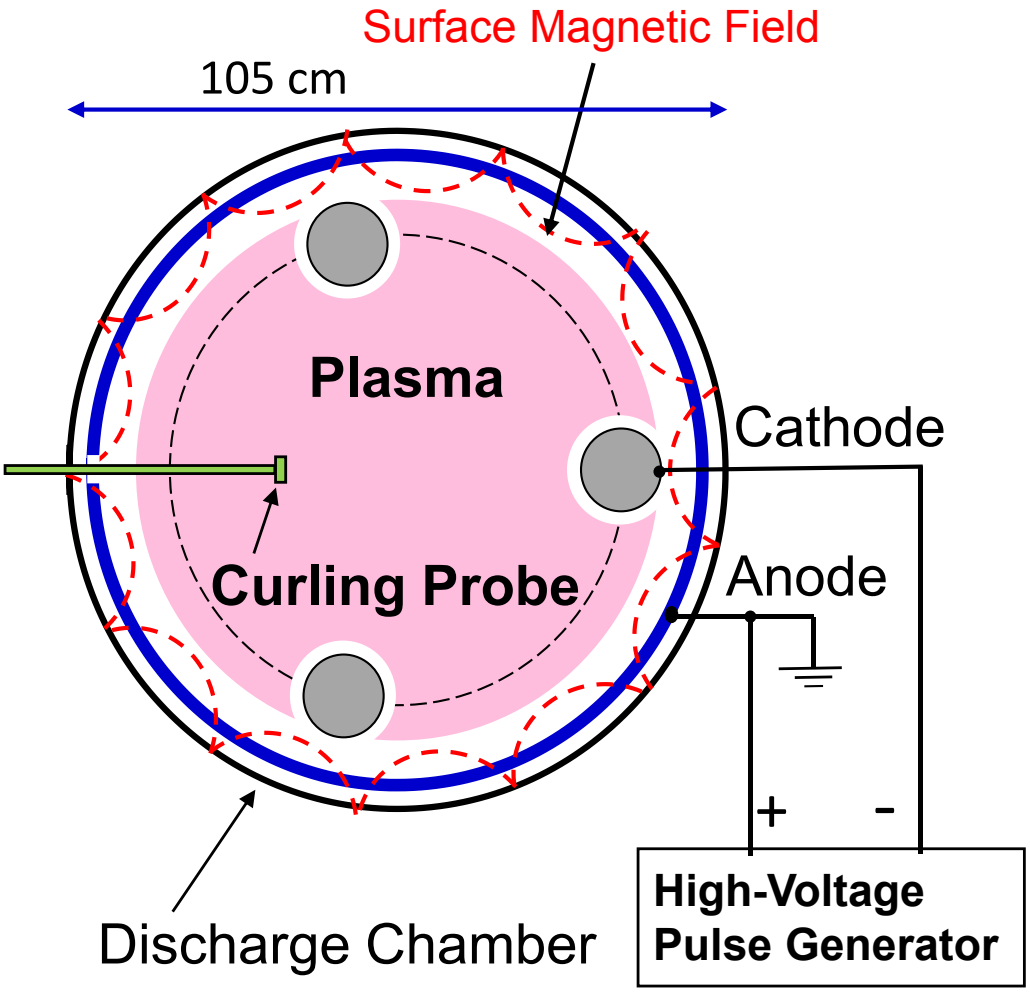


Fig. 6.2 DC pulsed plasma device with SMC.

cathodes. Fig. 6.2 shows the schematic of the experimental apparatus.

Pulsed plasma is produced in the chamber by applying a high voltage pulse (-1 kV) between the grounded anode (103 cm in diameter) and the cathodes. Permanent magnets were placed around the cylindrical side wall (anode) producing a surface magnetic field ~0.03 T.

The discharge apparatus is primarily used for pulsed CVD of DLC (diamond like carbon). As shown in Fig. 6.2, CP is inserted into the chamber at mid-height. A synchronous output from the high voltage source is used to trigger the NWA in *on point* mode. The details of data acquisition has already been discussed in Chapter 5 of this thesis.

## 6.3 Effect of surface magnetic confinement (SMC)

Surface magnetic confinement (SMC) reduces the diffusion loss of a plasma so that a high density plasma can be produced. The concept of SMC was experimentally applied to an inductively coupled plasma (ICP) by T.Shirakawa et al[6]. They observed dramatic effects of SMC, such as very low pressure discharge (~$3\times10^{-3}$ Pa) and drop of plasma potential from 80 V to 20 V. Figure 6.3 shows the electron density dependence on pressure obtained by Shirakawa et al[6].

Two notable effects of SMC can be observed in Fig.6.3, namely, high plasma density and a low discharge pressure. To observe the effects of SMC in our experiment, a comparison of discharge voltage and current for the SMC device (Fig. 6.2) and device without SMC (Fig. 4.2) in nitrogen at 1 kHz DR 30% was made.

Figure 6.4 (a) shows the discharge chamber without SMC, (b) and (c) show the discharge voltage and current respectively. It should be noted that Fig. 6.4 (a) represents the same figure as Fig. 4.2. The minimum pressure at which discharge could be produced in device without SMC was 10 Pa.

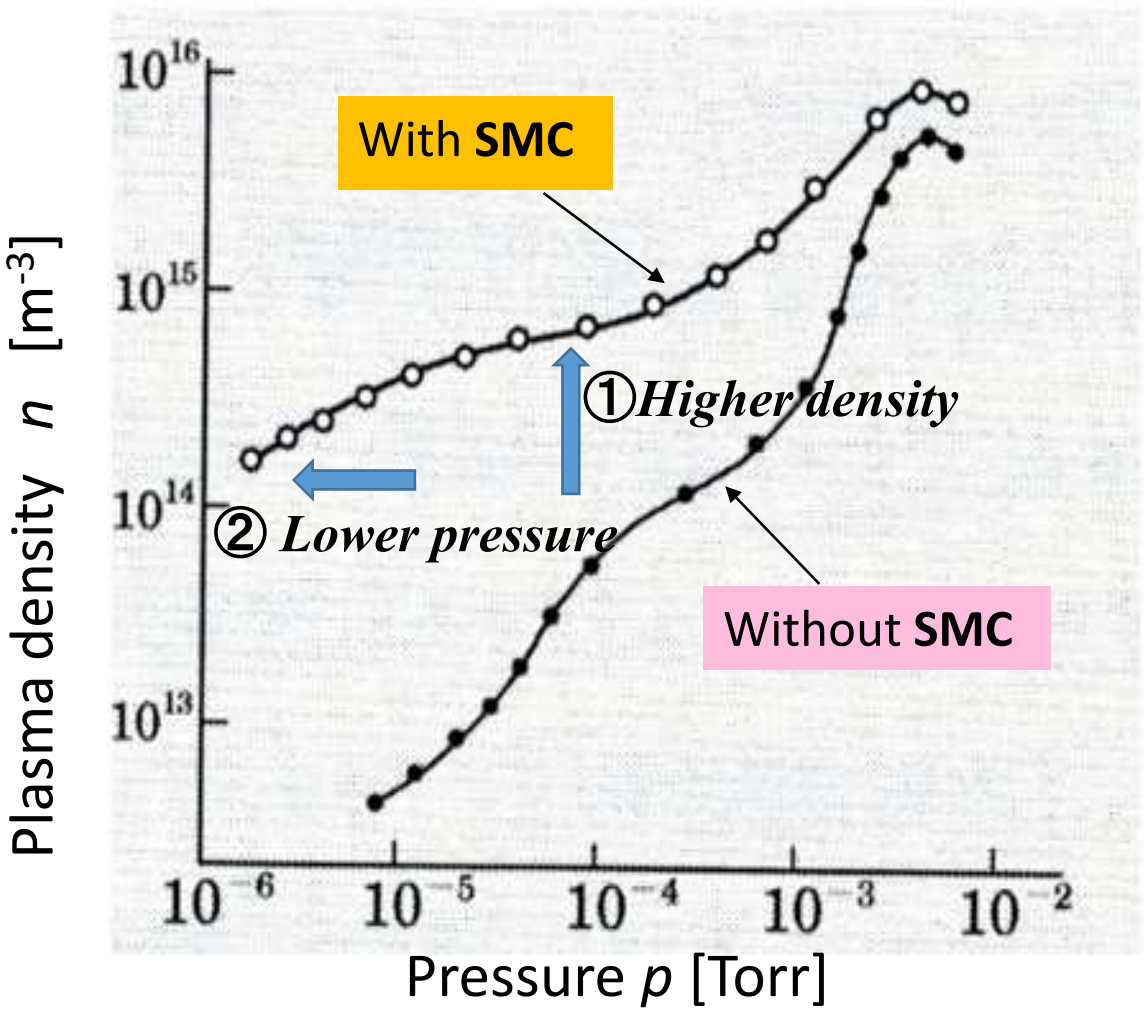


Fig. 6.3 Effect of SMC observed by T. Shirakawa in ICP device.

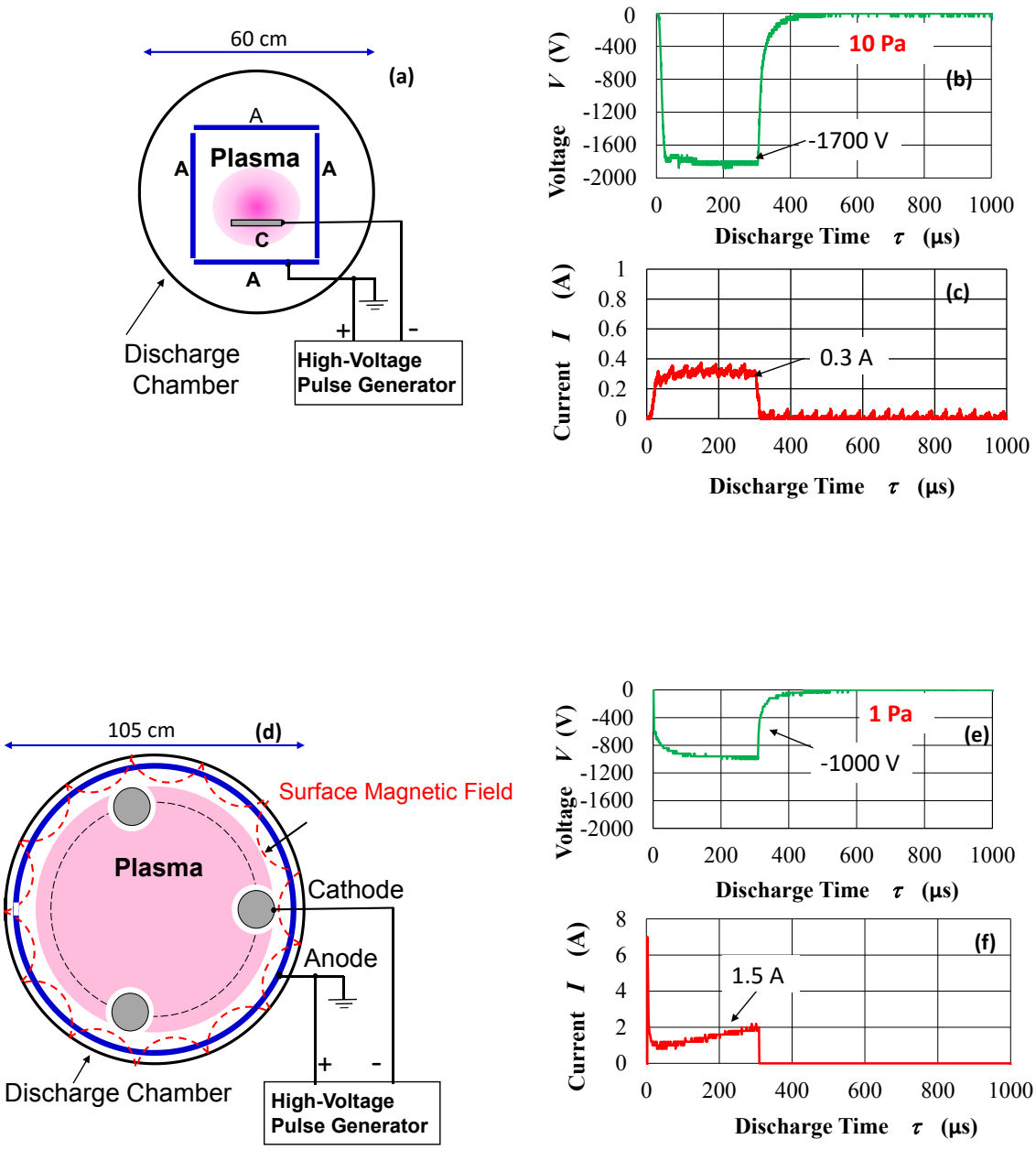


Fig. 6.4 (a) Discharge chamber without SMC, (b) discharge voltage curve, (c) discharge current, (d) Discharge chamber with SMC, (e) discharge voltage, and (f) discharge current

Nitrogen discharge at 1 kHz DR 30% was produced in SMC device. Despite the larger volume of SMC apparatus, discharge could be produced at 1 Pa, viz, $1/10^{th}$ the pressure compared to device without SMC. Also, discharge was produced at a lower discharge voltage (~1 kV) at five times the discharge current (1.5 Amp). The discharge chamber, discharge voltage and current are shown in Fig. 6.4 (c), (d) and (e) respectively. These results can be attributed to the effects caused by SMC.

## 6.4 Electron density measurement in SMC device

Pulsed plasma was produced in different gases (Ar, $CH_4$ and $C_2H_2$) in the SMC device typically at 1 Pa at different pulse repetition frequencies. The time dependence of electron density, density dependence on gas species was investigated as described below.

### 6.4.1 Density dependence on pulse repetition frequency

An experiment was carried out to observe the effect of pulse repetition frequency on peak electron density. The probe was positioned at a distance of 160 mm from the cathode and discharge was produced in Ar at 1 Pa at a constant discharge voltage. The pulse- repetition frequency was changed but the *discharge on* time $T$ and time of observation $\tau$ point was kept constant at all frequencies. Fig. 6.5 shows the data of peak electron density change with discharge frequency. It was found that the peak electron density increases with increasing pulse repetition frequency.

At *discharge on,* the electron density started to increase and reached some peak value just before *discharge off.* In the afterglow regime, the electron density decreased slowly until the start of *discharge on* in the next pulse, at which the electron density abruptly dropped to zero. In other words, some discontinuity in electron density evolution was observed for argon discharge which will be described in the next section.

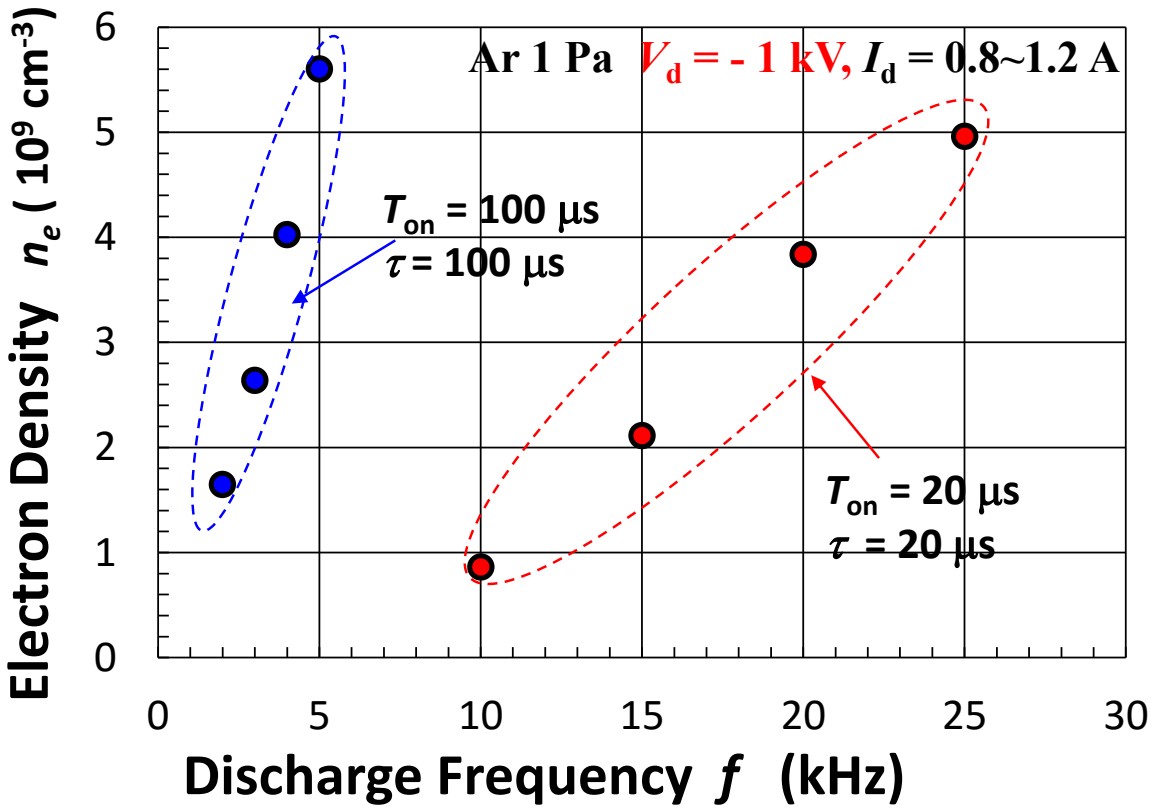


Fig. 6.5 Peak electron density dependence on discharge frequency.

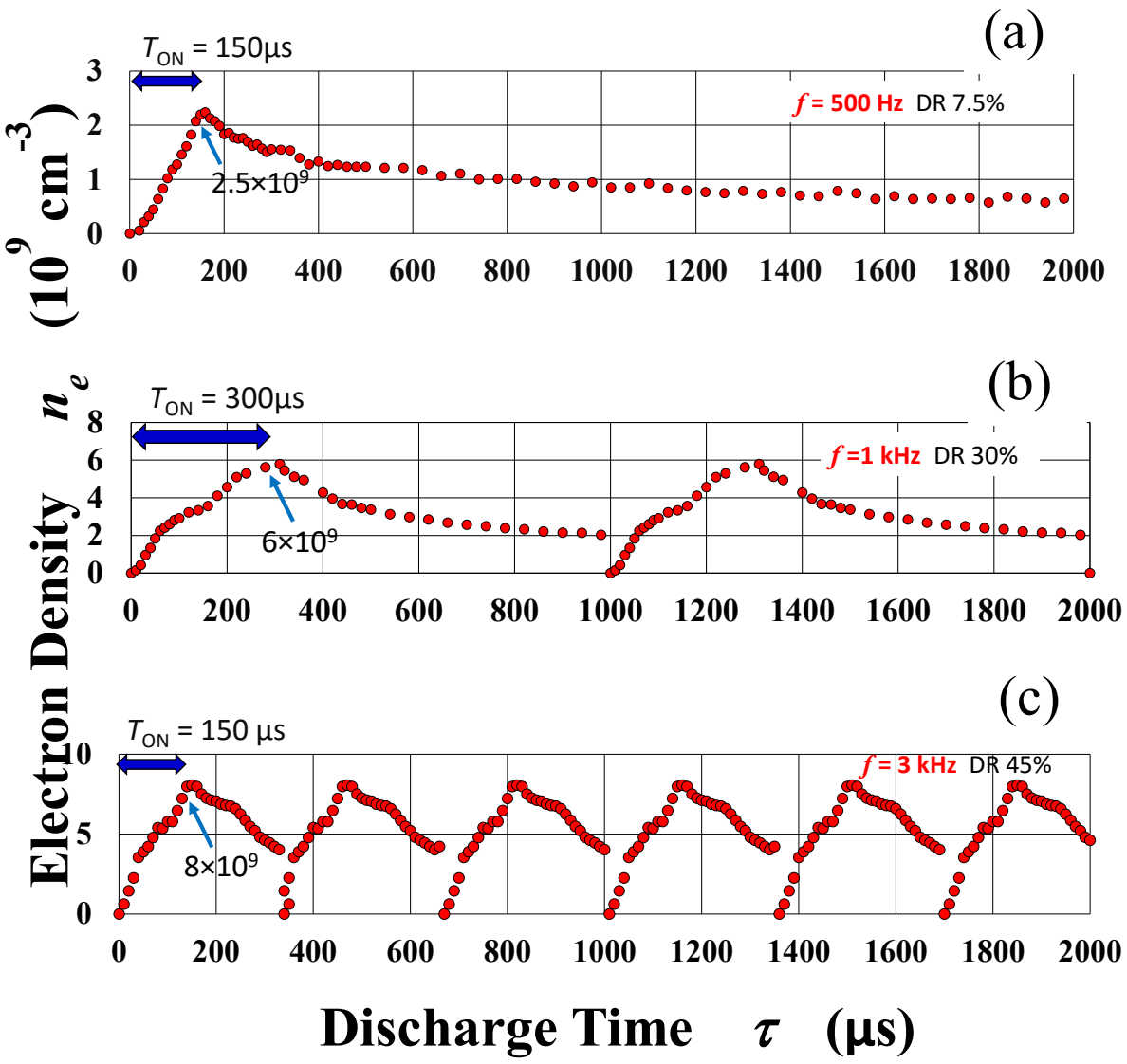


Fig. 6.6 Time resolved electron density measured at (a) 500 Hz DR 7.5%, (b) 1 kHz DR 30% and (c) 3 kHz DR 45%.

### 6.4.2 Sheath dynamics during discharge ON/OFF

The probe position was very close to the cathode (~5 mm) for the experimental results obtained in Sec. 6.4.1. To understand the sudden drop of electron density in Ar discharge, a simplified figure showing sheath thickness before and after the discharge is shown in Fig. 6.7 (a) and (b).

In the afterglow region the electron density decreases slowly and a thin sheath surrounds the cathode as shown in Fig. 6.7 (a). At *discharge on* (next pulse), a large voltage (approx. -1 kV) is suddenly applied to the cathode. This results in strong repulsion of electrons near the cathode and formation of a thick sheath as shown in Fig. 6.7 (b). Due to the sheath expansion, the area just in front of the CP becomes void of electrons and hence the CP registers electron density to be zero. It should be noted that the plasma density itself doesn't completely become zero : there are residual electrons in the chamber (away from cathode and CP). In the cartoon shown in Fig. 6.7 (c) the black solid line shows the density variation of electrons due to sheath expansion. If the probe is moved farther away, the electron density should follow the trend of the dashed line as shown in Fig. 6.7 (c).

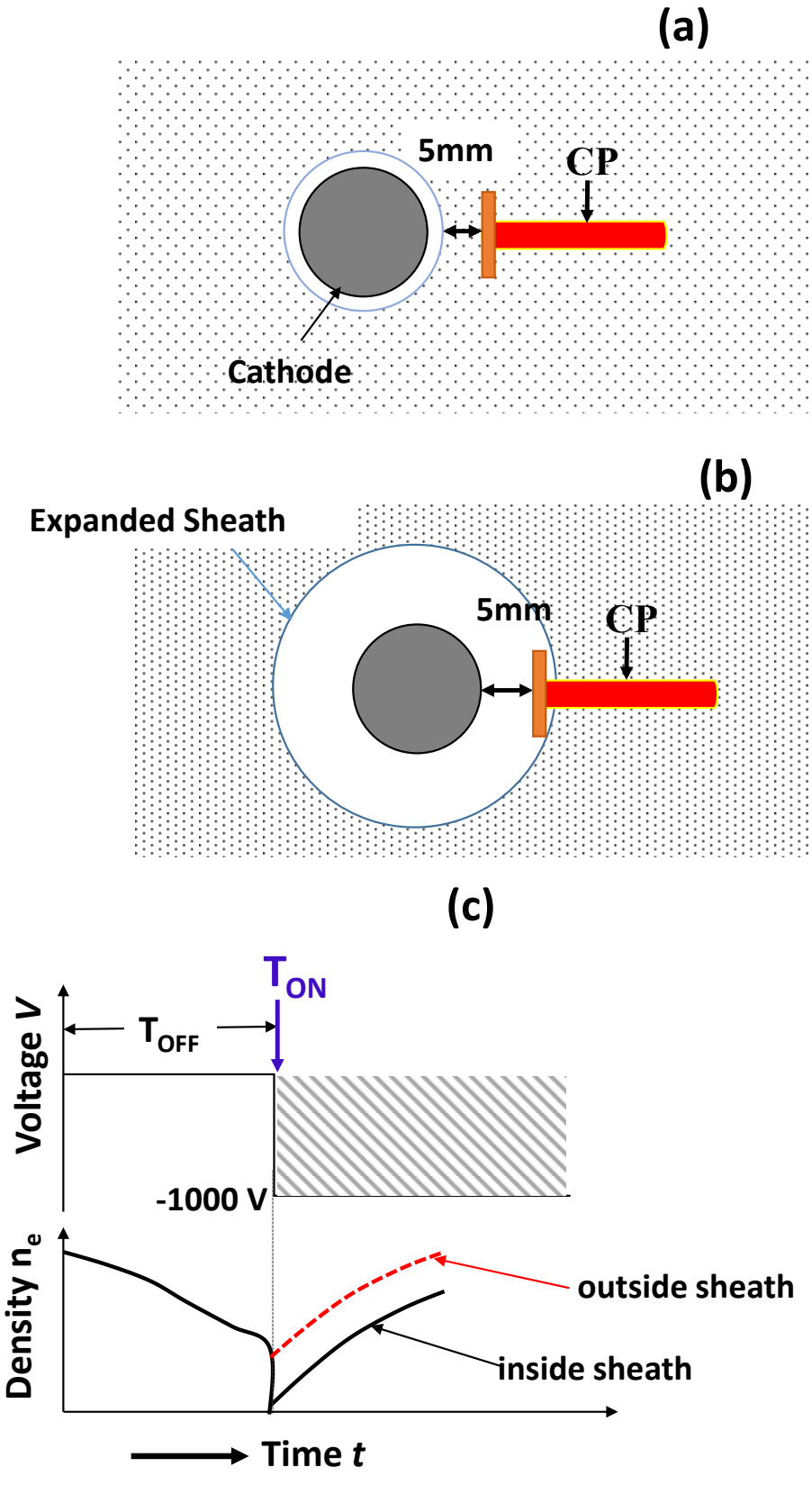


Fig. 6.7 (a) Sheath in afterglow region, (b) sheath expansion at discharge on, and (c) cartoon of electron density observed inside & outside sheath.

### 6.4.3 Electron density evolution dependence on gas species

Time resolved electron density measurement was performed in Ar, $CH_4$ and $C_2H_2$ discharge at 1 kHz DR 30% at 1 Pa. Fig. 6.8 shows the time evolution of electron density in Ar, $CH_4$ and $C_2H_2$. It can be seen that the peak electron density in Ar is higher compared to $CH_4$ and $C_2H_2$ and decays more slowly in the afterglow region.

It is well known that electrons with longer mean free path are well-confined in magnetic field[7,8]. In most cases, electrons with high energy have long mean free path. In Ar plasma, abundant high energy electrons with long mean free path are available, therefore, the electrons are well-confined by magnetic field. This results in high electron density and slower decay in the afterglow.

However, $CH_4$ and $C_2H_2$ are molecular gases and high energy electrons are readily lost through vibrational and rotational excitation[9]. So, most of electrons in $CH_4$ and $C_2H_2$ discharge have low energy with short mean free path and hence they aren't well-confined by surface magnetic field. As a result the electrons quickly decay in afterglow.

## 6.5 Summary

Time resolved electron density measurement was performed in SMC device for different gas species. A marked effect of SMC was observed, i.e, discharge at low pressure ($1/10^{th}$ ) at lower voltage and higher current (5 times). The time-resolved electron density measured in argon, showed discontinuity in density change at the start of discharge, which was explained in terms of sheath dynamics. Comparison of discharge produced in Ar, $CH_4$ and $C_2H_2$ at 1 Pa in 1 kHz DR 30% showed very high electron density for Ar. Ar plasma has high energy electrons with longer mean free path which are well-confined by surface magnetic field. On the other hand, the high energy electrons in $CH_4$ and $C_2H_2$ are used up in dissociation process, so that they are weakly confined by surface magnetic field.

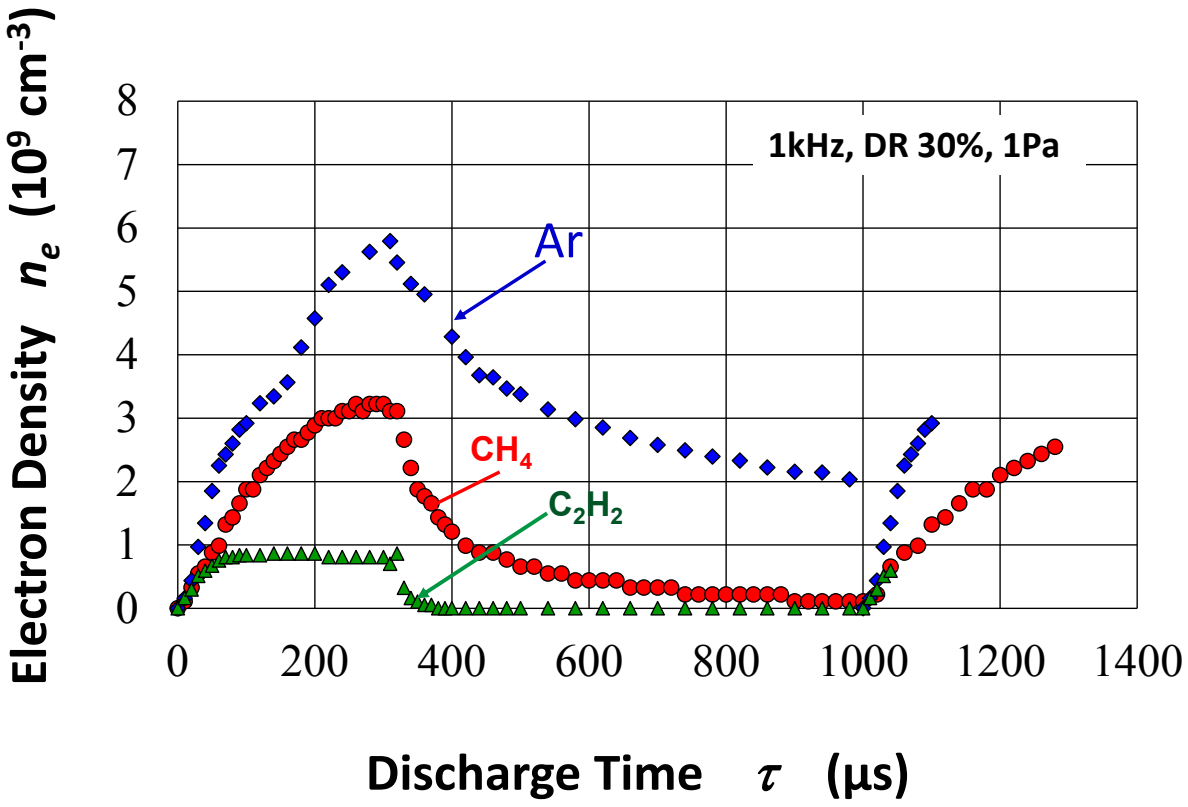


Fig. 6.8 Time resolved electron density measured in Ar, $CH_4$ and $C_2H_2$ at 1 kHz DR 30%.

References

1) J. R. Roth, *Industrial Plasma Engineering* Vol. I (IOP Publishing, London, 1994), 1st ed., p.79

2) M.A. Lieberman and A.J. Lichtenberg, *Principles of Plasma Discharges and Materials Processing* (Wiley, New York, 2005) 2nd ed., p. 155, p.82

3) H. Sugai, *Purazuma Electronics*(Plasma Electronics), (Ohmsha, Tokyo, 2000) 1st ed., p84[In Japanese]

4) K.N. Leung, T.K. Samec, and A. Lamm (1975), *Phys. Lett.* **51A,** 490.

5) K.N. Leung, G.R. Taylor, J.M. Barrick, S.L Paul, and R.E Kribel (1976), *Phys. Lett.* **57A,** 145.

6) T. Shirakawa, H. Toyoda and H. Sugai (1990) Jpn. J. Appl. Phys. **29** L1015

7) A. Y. Wong, Y. Nakamura, B. H. Quon, and J. M. Dawson (1975), *Phys. Rev. Lett.* **35**, 1156

8) H. Takekida, and K. Nanbu (2004), *J. Phys. D* **37**, 1800

# Chapter 7

# Summary and Future Scope

## 7.1 Summary

A brief summary of this thesis will be made in this chapter. Plasmas contain reactive species (free radicals, ions, electrons) which make them useful for industrial materials processing. New kind of plasma generation techniques and monitoring tools are therefore essential for effective process control and understanding the mechanism of processes.

In Chapter 1 a general introduction of fundamentals of plasma was made. Parameters like degree of ionization, quasi-neutrality, Debye length, and plasma frequency were briefly introduced. Also, probe diagnostic techniques like Langmuir probe, plasma oscillation probe, plasma absorption probe, and microwave resonator probe were briefly discussed. Langmuir probe is easy to construct and operate, however it is difficult to obtain accurate data due to complexities involved in the interpretation of I-V characteristics. Plasma oscillation probe and plasma absorption probe also have their own limitations. For example the hot filament used as electron source in plasma oscillation probe has a short-life time and plasma absorption probe cannot be applied to low electron density plasmas ($< 10^{10}$ $cm^{-3}$). Microwave resonator probe also called *hairpin probe* is difficult to construct and operate (fragile). Also, it can cause metal impurity contamination of the plasma

In Chapter 2, a new type of probe called *curling probe* was introduced. Curling probe is actually a modified form of microwave resonator probe that uses compact, spiral slot mono-pole antenna. The probe is made free from metal impurity contamination by the use a of a thin quartz cover (0.1~0.2 mm) that blocks the plasma from entering inside the probe. FDTD (Finite

difference time domain) simulation using a commercial software was used for probe modeling. A method of accurately determining the electron density in an experiment by using the results of FDTD simulation as a reference was shown. But, this approach was time-consuming and inconvenient. So, an analytical approach was used to develop a tractable formula to calculate electron density. A comparison of correction factor $\gamma$ in both simulation and the analytical approach was made. Curling probe was finally used in an ICP (Inductively coupled plasma) device to observe discharge and RF-bias effect on electron density.

In Chapter3, development of *opto-curling probe* (Opto-CP) was discussed. Opto-CP is a developed form of a conventional curling probe that enables simultaneous measurement of electron density and optical emissions from the plasma. It was shown that Opto-CP can be used to obtain radical densities in the plasma without the use of actinometry technique (rare gas addition). Finally, Opto-CP was used to monitor plasma CVD and cleaning process in $CH_4$ and $O_2$ plasma.

In Chapter 4, a technique to measure electron density in a pulsed plasma using curling probe was discussed. In a plasma with time-varying electron density, synchronization of discharge pulse with network analyzer (NWA) sweep is required to measure the electron density. The synchronization condition for a sweep time $T_{swp}$ of NWA with the pulse modulation period $T$ for $n$ no. of points was found to be $(n\text{-}1)T/T_{SWP}$= integer (1, 2, ⋯) .

In Chapter 5, two modes of NWA synchronization, namely *on sweep* and *on point* was compared. *On sweep* mode was found to be applicable in low pulse repetition frequency (< 0.5 kHz) pulsed plasma. Electron density measurement using *on sweep* mode was tedious, it was replaced with *on point* mode. Time-resolved electron density was measured up to 25 kHz with a minimum time resolution of ~ 2 μs. Electron density decay in plasma afterglow was also investigated. The decay trend for Ar afterglow was found to be different compared to

$N_2$ plasma afterglow. Electron energy distribution function (EEDF) measurement using Langmuir probe was carried out to understand the difference in decay mechanism.

In Chapter 6, curling probe was used in a large-volume plasma source with surface magnetic confinement (SMC). A comparison of discharge pressure, voltage and current was made between plasma sources with/without SMC. SMC was found to produce discharge at lower pressure and voltage with higher current. Pulse repetition frequency dependence of electron density was measured. Time- resolved electron density measured in $CH_4$, $C_2H_2$, and Ar at the same pressure and voltage showed highest electron density in Ar plasma. Ar plasma has more energetic electrons due to which magnetic confinement is effective.

## 7.2 Future Scope

*Curling probe* is a robust plasma monitoring tool that can be used in reactive plasmas as well. A variant of curling probe called opto-curling probe is more useful because of its ability to perform optical measurement. There are still many works that need to be done for further development of probe. Since the current analytical model isn't perfect there are rooms for some improvements so that probe analytical results are in better agreement with simulation results. Curling probe like all other probe diagnostic techniques causes some perturbation in the plasma. This perturbation can be minimized if the probe cross-section area is smaller. Therefore, work needs to be done for probe miniaturization. Also, the current probe cannot measure electron density in strongly magnetized plasma. So, new probe model needs to be developed to account for the effect of strong magnetic field. In conclusion, there are several aspects in which further work is needed to make curling probe measurement more reliable and accurate.

# Acknowledgement

I would like to express my gratitude to my academic supervisor, Professor Keiji Nakamura for providing me opportunity to do research and work towards my doctorate degree. I also want to thank Professor Hideo Sugai for his guidance, encouragement and help. He has been and will be a source of continuous inspiration for me.

I want to thank Professor Hideo Goto and Professor Junzo Ishikawa for their advice, valuable comments for the improvement of this thesis. I would also like to thank Mr. Kimitaka Kato, who helped me to perform experiments in the laboratory in the early years of my research. Much of the experimental work would have become impossible without the help of Mr. Kato. I also want to thank visiting Professor Ivan Ganachev for his suggestions and guidance at conducting computer simulations.

I also want to express my thankfulness to Mr. Hiroyuki Matsuoka, Wataru Sakakibara and Hiroki Tashiro from the research team at DOWA Thermotech Ltd. Most of my research work was done in close collaboration with the research team. I want to thank them for their cooperation despite their hectic schedule.

Student life is always full of many challenges including financial ones. I want to thank Mr. Kawai, CEO of Aichi Denkyu Company for providing me Gumbro scholarship. I am really grateful to Mr. Kawai and his friend Mr. Mizuno for their generosity. I also cannot help myself without thanking Heiwa-Nakajima Foundation, for providing me a generous scholarship for one year. The financial support I received from Heiwa-Nakajima Foundation helped me to completely focus on my studies in pursuit of doctorate degree. Chubu University *research assistant* support and special scholarship for graduate student was also instrumental for reducing my financial burden. I also want to thank the Nagai Foundation for providing me

financial assistance to participate in an international conference held in Australia.

I also can`t help myself without thanking my uncle Dr. Shankar Parajulee and my aunt Bina Sharma, who have been on my side supporting, encouraging and suggesting me in all the endeavors I take. I will be forever indebted for their love and kindness.

I want to appreciate and thank my wife Saraswati Karki for her relentless support, help and enduring love. Finally, I would like to thank my family and all my friends here in Japan and back home for their support and encouragement.

# Appendix

# List of research achievements

## A.1 Journal articles

| S.N | Title | Journal | Authors | Chapter |
|---|---|---|---|---|
| 1 | Opto-curling probe for simultaneous monitoring of optical emission and electron density in reactive plasmas | Appl. Phys. Express **6** (2013) 056202 | **Anil Pandey**<br>Keiji Nakamura<br>Hideo Sugai | 3 |
| 2 | Curling probe measurement of electron density in pulse-modulated plasma | Appl. Phys. Lett. **104**, 024111 (2014) | **Anil Pandey**<br>Wataru Sakakibara<br>Hiroyuki Matsuoka<br>Keiji Nakamura<br>Hideo Sugai | 4 |
| 3 | Time resolved curling probe measurements of electron density in high frequency pulsed DC discharges | Jpn. J. Appl. Phys. **55**, 016101 (2016) | **Anil Pandey**<br>Wataru Sakakibara<br>Hiroyuki Matsuoka<br>Keiji Nakamura<br>Hideo Sugai | 5 |
| 4 | Spatio-temporal curling probe measurement of electron density under surface magnetic confinement | Plasma. Sci. Technol. PSST-101077 (submitted) | **Anil Pandey**<br>Hiroki Tashiro<br>Keiji Nakamura<br>Hideo Sugai | 6 |

# A.2 Presentations at International Conferences

| S.N. | Title | Conference | Authors | Ch. |
|---|---|---|---|---|
| 1 | Opto-curling probe monitoring of local density of electron and radicals. | *21st International Symposium on Plasma Chemistry*(ISPC-21), Cairns Convention Center, Cairns, Australia | **Anil Pandey**, Kimitaka Kato, Shunjiro Ikezawa, Keiji Nakamura, Hideo Sugai | 3 |
| 2 | Opto-Curling Probe method for space-resolved measurement of electron and radical densities in plasma | *Dry Process Symposium 2013*, Ramada Plaza Hotel, Jeju, South Korea | **Anil Pandey**, Keiji Nakamura, Hideo Sugai | 3 |
| 3 | Curling probe analysis and simulation for collisional plasma | *8th International Conference on Reactive Plasmas and 31st Symposium on Plasma Processing* (ICRP-8), Fukuoka, Japan, | **Anil Pandey**, Keiji Nakamura, Hideo Sugai | |
| 4 | Curling probe measurement of plasma modulated at high frequency | *ISPlasma 2015*, Nagoya | **Anil Pandey,** Wataru Sakakibara, Hiroyuki Matsuoka, Keiji Nakamura, Hideo Sugai | 4, 5 |
| 5 | Curling probe measurement of large-volume pulsed plasma confined by surface magnetic field | 68th Gaseous Electronics Conference, Honolulu, Hawaii, USA | **Anil Pandey**, Wataru Sakakibara, Hiroki Tashiro, Keiji Nakamura, Hideo Sugai | 6 |
| 6 | Curling probe measurement of electron density in pulse-modulated at high frequency | 62nd AVS International Symposium and Exhibition, San Jose, California, USA | **Anil Pandey**, Wataru Sakakibara, Hiroyuki Matsuoka, Keiji Nakamura, Hideo Sugai | 5 |
| 7 | Effect of SMC on Production of Large-Volume Pulsed Plasma | Dry Process Symposium 2015, Awaji island, Japan | **Anil Pandey**, Wataru Sakakibara, Hiroki Tashiro, Keiji Nakamura, Hideo Sugai | 6 |